DEFINING TOUCH RECEPTORS AND THEIR CENTRAL PATHWAYS CONTROLLING TOUCH AND PAIN

by
Ling Bai

A dissertation submitted to Johns Hopkins University in conformity with the requirements for the degree of Doctor of Philosophy

Baltimore, Maryland

November, 2016

Abstract

Touch perception begins with activation of peripheral low-threshold mechanoreceptors (LTMRs) subtypes, and LTMR activity ensembles are propagated to the central nervous system (CNS) where they are integrated. Understanding the unique response properties and functions of LTMR subtypes and how ensembles of LTMR activities are processed in the CNS are major goals of somatosensory research. In the first part of my thesis, I genetically identified a major mammalian LTMR subtype that is sensitive to gentle stroking of the skin and I defined the peripheral morphological structures that specify their unique mechanical receptivity. In a survey of mammalian skin, I found a preponderance of neurofilament-heavy chain^{+} circumferential endings associated with hair follicles, prompting the development of a genetic strategy to interrogate these neurons. Targeted *in vivo* recordings revealed them to be Aβ Field-LTMRs, identified 50 years ago but largely elusive thereafter. Remarkably, while Aβ Field-LTMRs are highly sensitive to gentle stroking of the skin, they are unresponsive to hair deflection, and they encode skin indentation in the noxious range across large, spotty receptive fields. Individual Aβ Field-LTMRs form up to 180 circumferential endings, making them the most anatomically expansive LTMR identified to date and suggesting their sensitivity to skin stroking arises through integration across many low-sensitivity circumferential endings. In the second part of my thesis, I have examined the anatomy and function of LTMRs and their spinal cord ascending pathways. I found that spinal cord projection neurons (PSDCs) that innervate the dorsal column nuclei via the dorsal column are critical for the development of mechanical allodynia in mouse models of neuropathic pain. This finding defines a novel ascending pathway for mechanical allodynia and challenges the traditional view in the field that the anterolateral tract carries all ascending pain information.

Advisor: David D. Ginty, Ph.D.

Acknowledgments

Firstly, I would like to express my sincere gratitude to my thesis advisor, Dr. David Ginty, for his great mentorship over the years. I am grateful to have the opportunities to explore scientific questions under his guidance. His passion and vision on science, and his generous support to lab members, have had a great impact on me and have shaped me for my future scientific career.

I thank my thesis committee members, Dr. Xinzhong Dong, Dr. Michael Caterina, and Dr. David Linden, for their advice and insightful suggestions on my thesis research, and their support during my postdoctoral applications.

I would also like to thank all past and current members of the Ginty lab for their help and support, especially Dr. Yin Liu, Dr. Lishi Li, Dr. Siyi Huang, and Dr. Ting Guo for their suggestions and guidance in the early stage of my Ph.D. training, Dr. Brendan Lehnert for the *in vivo* DRG electrophysiology recordings and insightful discussions on my thesis research, Dr. Travis Dickendesher for generating *Advillin-Flpo* mouse line, and Dr. Anda Chirila for her spinal cord slice physiology recordings.

I thank Dr. Alex Kolodkin and Dr. King-Wai Yau for his encouragement and advice on my thesis research and scientific career development.

I thank my rotation lab advisor, Dr. Elisabeth Glowatzki, Dr. Christopher Potter, Dr. Richard Huganir for introducing me to different directions on neuroscience research. I would also like to thank Dr. Eunyoung Yi and Dr. Gareth Thomas for their mentorship and guidance during my rotations.

Lastly, I thank my parents, Yong Bai and Jingna Bao, and my husband, Junwei Liu, for their love and support.

Table of contents

List of figures

Chapter 1. Introduction

Sensitivity to mechanical stimuli is crucial for communication and survival of all organisms. In the case of mammalian skin, innocuous mechanical stimuli are detected by a diverse group of cutaneous low-threshold mechanoreceptor (LTMR) subtypes with distinct morphologies, physiological properties and functions. LTMRs are pseudo-unipolar sensory neurons whose cell bodies reside within dorsal root ganglia (DRG) or trigeminal ganglia. Their touch sensitivity derives from mechanosensitive peripheral axonal terminals that reside in the skin, where they associate with end organs that determine the geometry of their axonal terminals and force sensitivity (Loewenstein, 1969; Zimmerman et al., 2014). Touch stimuli are encoded and further transferred via axons to the central nervous system (CNS), where LTMR inputs carrying distinct aspects of touch information converge and integrate (Abraira and Ginty, 2013; Lechner and Lewin, 2013; Lumpkin et al., 2010). Thus, understanding the unique response properties and functions of LTMR subtypes and how ensembles of LTMR activities that underlie touch perception are integrated and processed in the CNS are major goals of somatosensory research.

1.1. LTMRs of hairy and glabrous skin

LTMRs are a heterogeneous group of sensory neurons. Just as the gustatory system has distinct taste receptors optimally tuned to detect sweet, sour, salty, umami, or bitter flavors, LTMRs are divided into subtypes distinguished by their unique tuning properties as well as their sensitivity, conduction velocity, and adaptation to sustained mechanical stimulation. For example, slowly-adapting (SA) touch receptors are indentation detectors, firing continuously during a sustained stimulus, while rapidly-adapting (RA) touch receptors are velocity detectors that only respond to the onset and offset of indentation.

In mammalian glabrous and hairy skin, at least seven LTMR subtypes tuned to distinct but overlapping features of a tactile stimulus have been described (Abraira and Ginty, 2013; Horch et al., 1977). Each subtype forms specialized axonal terminals associated with end organs (Figure 1). Aβ SA1-LTMRs form disc-like axonal terminals that associate with Merkel cells, which are located in the basal epidermis and are themselves mechanically sensitive, endowing Aβ SA1-LTMRs with their characteristic slowly adapting response property (Ikeda et al., 2014; Maksimovic et al., 2014; Maricich et al., 2009a; Woo et al., 2014). Aβ RA1-LTMRs are rapidly adapting and respond on/off set of sustained stimuli. In glabrous skin, Aβ RA1-LTMRs innervate Meissner corpuscles in dermal papillae underneath the epidermis and are sensitive to movement across the skin. While in hairy skin Aβ RA-LTMRs, together with Aδ-LTMRs and C-LTMRs, form longitudinal lanceolate endings, which extend along the long axis of hair follicles and are rapidly or intermediately adapting to skin indentation (Li et al., 2011). In contrast, Aβ RA2-LTMRs terminate deep in the dermis where they are wrapped by layers of cushion-like lamellar cells within Pacinian corpuscles; these serve as high pass mechanical filters that underlie the unique Aβ RA2-LTMR high frequency vibration tuning property. Aβ SA2-LTMRs also terminate in the dermis and may form Ruffini endings (Chambers et al., 1972), although this is controversial. The least understood LTMR subtype, the Aβ Field-LTMR (field receptor), first described nearly 50 years ago in the cat by Burgess and colleagues, is rapidly or intermediately adapting to skin indentation (Burgess et al., 1968; Horch et al., 1977). These neurons are sensitive to gentle stroking of the skin but rarely respond to deflection of individual hairs (Horch et al., 1977). The terminal structure and skin arborization patterns of Aβ Field-LTMRs have not been determined, leaving open the question of how these distinct properties arise.

Recently, molecular genetic tools have been developed which facilitate our understanding of the molecular identity, peripheral terminal structure, circuit organization of LTMRs (Li et al., 2011; Luo et al., 2009; Rutlin et al., 2014). However, there are still LTMR subtypes that are not

well studied and even unexplored. In order to gain insight into how touch is encoded by different LTMR subtypes, I attempted to identify uncharacterized LTMR subtypes using anatomical tracing and mouse molecular genetic approaches (Chapter 2). I've taken an unbiased retrograde labeling approach to visualize the cutaneous endings of Aβ LTMRs, which guided molecular-genetic strategies to label the Aβ LTMRs for which genetic tools do not currently exist, specifically Aβ SA1-LTMRs as well as the elusive Aβ Field-LTMRs.

Figure 1.1 Schematic image depicts the peripheral axonal terminals of primary sensory neurons in the skin.

(A-B) Innocuous touch information is processed by both glabrous hairless (A) and hairy (B) skin. (Image adapted from Abraira and Ginty, 2013).

(A) In glabrous skin, innocuous touch is mediated by four types of mechanoreceptors, including Aβ SA1-LTMRs with Merkel ending**s**, Aβ SA2-LTMRs with Ruffini endings, Aβ RA1-LTMRs with Meissner corpuscles, and Aβ RA2-LTMRs with Pacinian's corpuscles.

(B) In hairy skin, tactile stimuli are transduced through three types of hair follicles, defined in the mouse as guard, awl/auchenne, and zigzag. The longest hair type, guard hairs, is associated with touch domes at the apex and Aβ-LTMR lanceolate endings at the base. Awl/auchene hairs are triply innervated by C-LTMR, Aδ-LTMR, and Aβ-LTMR lanceolate endings. Zigzag hair follicles are the shortest and are innervated by both C-LTMR and Aδ-LTMR lanceolate endings. In addition, all three hair follicle types are innervated by circumferential endings whose physiological properties will be discussed in Chapter 2. Abbreviations: SC, stratum corneum; SG, stratum granulosum; SS, stratum spinosum; SB, stratum basalis.

Figure 1.1

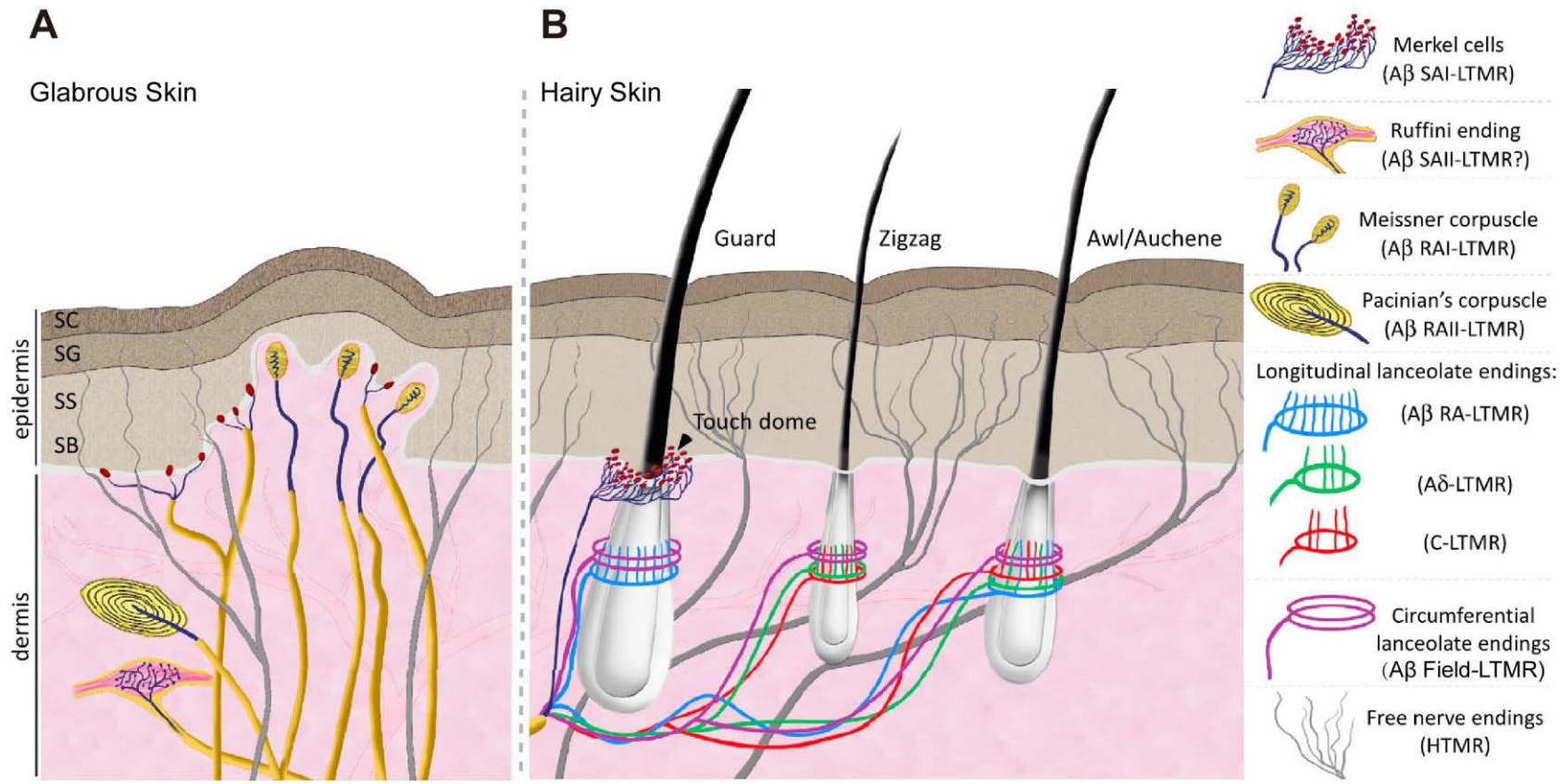
A
Glabrous Skin
epidermis
dermis
SC
SG
SS
SB
B
Hairy Skin
Guard
Zigzag
Awl/Auchene
Touch dome
Merkel cells
(Aβ SAI-LTMR)
Ruffini ending
(Aβ SAII-LTMR?)
Meissner corpuscle
(Aβ RAI-LTMR)
Pacinian's corpuscle
(Aβ RAII-LTMR)
Longitudinal lanceolate endings:
(Aβ RA-LTMR)
(Aδ-LTMR)
(C-LTMR)
Circumferential
lanceolate endings
(Aβ Field-LTMR)
Free nerve endings
(HTMR)

1.2. The form that underlies function of cutaneous touch receptors

The sensitivity of different LTMR subtypes derives from mechanosensitive peripheral axonal terminals that reside in the skin, where they associate with distinct end organs that determine the geometry of their axonal terminals in different locations of the skin (Abraira and Ginty, 2013; Zimmerman et al., 2014). It has been long argued that the particular mechanical response properties of LTMR subtypes are determined by the unique geometry of their axonal terminals and associated end organs (Loewenstein, 1969). In this section, I will summarize the recent findings describing the ultrastructural features of mechanosensory end organs underlying the unique function LTMR subtypes.

1.2.1. Merkel cell/Aβ SA1-LTMR mechanotransduction

Aβ SA1-LTMR responses to static indentation comprise a high frequency dynamic phase during initial skin indentation, and lower frequency, tonic firing during prolonged indentation. Functionally, studies mainly performed in human and other primates indicate that the glabrous skin Merkel cell/Aβ SA1-LTMR complex conveys information about texture, curvature and object shape with high spatial acuity (Blake et al., 1997; Maricich et al., 2009b). The Merkel cell/Aβ SA1-LTMR complex has been shared by many specialized skin types, including in a dome-shaped bulge close to guard hairs of hairy skin, in glabrous skin, the noses of moles, the wings of bats, whisker pads, the mucosa of the mouth and lips, and elsewhere (Halata et al., 2003).

The Merkel cells are a group of specialized oval cells in the basal layer of epidermis that are innervated by sensory fibers and were thus reasoned to mediate mechanosensation (Figure 1.2A). They are anchored within the epidermis by both thin cytoplasmic protrusions projecting to keratinocytes as well as desmosomes (Iggo and Muir, 1969). These physical connections link movement and compression of the skin to mechanical stress on Merkel cells. On the other hand,

Aβ SA1-LTMR endings exhibit stereotyped discoid enlargement and connect to the dermal side of each Merkel cell. Synapse-like structures at the junction between Aβ SA1-LTMR endings and Merkel cells have been described in multiple species and include a postsynaptic-like thickening of Aβ SA1-LTMR axon terminal membranes, and the presence of presynaptic protein and neurotransmitter in the Merkel cells (Fagan and Cahusac, 2001; Hartschuh and Weihe, 1980; Mihara et al., 1979). However, small clear synaptic vesicles typically associated with fast neurotransmission are absent in Merkel cells, and instead dense core vesicles are seen clustered near the presumptive postsynaptic region of axonal endings. These dense core vesicles are hypothesized to release neuropeptides rather than classical neurotransmitters, thus modulating Aβ SA1-LTMR responses.

Taste receptor cells in the gustatory system and hair cells of the auditory system are prominent examples of non-neuronal cells participating in stimulus transduction (Finger et al., 2005; LeMasurier and Gillespie, 2005), yet only recently was it shown that an analogous situation occurs in touch sensation. Merkel cells, both in culture and *ex-vivo*, exhibit mechanically activated currents, which are absent following loss of the mechanically activated cation channel Piezo2 (Ikeda et al., 2014; Woo et al., 2014). Moreover, optogenetic activation of Merkel cells is alone sufficient to evoke a slowly-adapting discharge in Aβ SA1-LTMRs, whereas ablation or functional inactivation of Merkel cells leads to a reduction in both the dynamic and static phases of Aβ SA1-LTMR firing in response to skin indentation (Maksimovic et al., 2014; Woo et al., 2014). Thus, both Merkel cells and Aβ SA1-LTMRs directly respond to mechanical force applied to the skin, and Merkel cells signal to Aβ SA1-LTMRs to achieve optimal activation of the LTMR, indicating an involvement of non-neuronal components of cutaneous touch complexes in the detection of stimuli as well as modulation of LTMR responses.

1.2.2. Glabrous corpuscle/Aβ RA-LTMR transduction mechanisms

Two types of rapidly adapting Aβ-LTMRs have been identified that are associated with corpuscle structures in glabrous skin. They are rapidly adapting to static indentation and are tuned to vibration and motion across the skin, in contrast to the static mechanical indentation encoded by Merkel cells/Aβ SA1-LTMRs. Psychophysical studies in humans have described two coding channels of vibration, with low-frequency sinusoids perceived as flutter, and high-frequency stimulation detected as vibration (Talbot et al., 1968). Indeed, Aβ RA1-LTMRs, which are tuned to low-frequency vibrations under 40Hz, can detect slip of an object in the hand (Johansson, 1978; Knibestöl, 1973; Talbot et al., 1968) and may be essential for reflex grip control. On the other hand, Aβ RA2-LTMRs are tuned to high frequency stimulation, with optimal activation around 200 Hz, and thus are involved in detecting vibration of held objects (Brisben et al., 1999; Iggo and Ogawa, 1977; Sato, 1961). Both Aβ RA1-LTMRs and Aβ RA2-LTMRs are associated with corpuscles structures which are discovered over 150 years ago. Nestled within dermal papillae of glabrous skin, Meissner corpuscles are composed of flattened lamellar cells which form an ellipsoid structure perpendicular to the skin surface, with one or more tortuous Aβ RA1-LTMR axons meandering throughout (Figure 1.2B) (Cauna, 1956; Idé, 1976). In contrast, the larger Pacinian corpuscles are found deep in the dermis of glabrous skin, and in some species hairy skin and non-cutaneous tissues including the mesentery and periosteum. Pacinian corpuscles are oval shaped, contain layered lamellae, and reach up to 3-4mm in length in adult human hands (Figure 1.2C) (Bentivoglio and Pacini, 1995; Cauna and Mannan, 1958).

The non-neuronal components of Meissner and Pacinian corpuscles are quite distinct, and their arrangement within the corpuscle offers clues about how vibration and dynamic movement across the skin are encoded. Each disc-like unit of the Meissner corpuscle consists of an unmyelinated axon terminal swelling surrounded by flattened Schwann cell-derived lamellar cells (Cauna, 1956; Cauna and Ross, 1960). These discoid units are serrated on their external surfaces while smooth on their inner surfaces, and are connected to collagen fibers that traverse the

fibroblast capsule surrounding them (Figure 1.2B) (Idé, 1976; Takahashi-Iwanaga and Shimoda, 2003). Significant convergence occurs, as a single Aβ RA1-LTMR innervates multiple Meissner corpuscles (Paré et al., 2002). During indentation, force is transduced via collagen fibers connected to the serrated edges of the lamellar cells, which leads to bending of Aβ RA1-LTMR axon terminals until the smooth lamellar cell middle compresses. This compression generates action potentials during stimulus onset and produces a rapidly-adapting response (Cauna and Ross, 1960; Takahashi-Iwanaga and Shimoda, 2003). How this mechanism results in Meissner corpuscle sensitivity at the low end of the frequency stimulation range is unknown.

In contrast to the layered lamellae organization of Meissner corpuscles, the non-neuronal components of Pacinian corpuscles are arranged in concentric lamellae, consisting of an inner core, an intermediate layer/growth zone, and an outer zone. The inner core is composed of tightly packed, bilaterally symmetric hemi-lamellar cells distributed along both sides of the Aβ RA2-LTMR axon terminal, with small diameter collagen fibers coursing longitudinally in the clefts between them (Paré et al., 2002; Pease and Quilliam, 1957). The outer zone, about three times thicker than the inner core, is composed of concentrically arranged, flattened and overlapping lamellar cells, interspersed with circularly oriented type II collagen fibers in the fluid-filled extracellular space (Pawson et al., 2000; Pease and Quilliam, 1957). A single, heavily myelinated axon penetrates each corpuscle. Its unmyelinated axonal branches project radially into the clefts between the inner core hemilamellar cells (Figure 1.2C) (Cauna and Mannan, 1958; Spencer and Schaumburg, 1973). The lamellar composition is believed to be responsible for the Aβ RA2-LTMR's encoding of high frequency vibration, postulated in a model proposed over 50 years ago: Pacinian corpuscle outer core lamellar cells and surrounding fluid act as a high pass filter that dampens low frequency mechanical stimuli, while allowing the slightest high frequency vibration to reach axonal filopodia via interconnected collagen fibers. The depolarizing generator potentials of the filopodia converge and summate on the primary axon (Loewenstein and Skalak, 1966).

Therefore, the cylindrically layered ultrastructure of Pacinian corpuscles facilitates the high-frequency sensitivity of Aβ RA2-LTMRs.

1.2.3. Hair follicle LTMR mechanotransduction mechanisms

Hair follicles are neurophysiologically complex mechanosensory organs. Apart from the SA1/Merkel cell complex, hair follicles are innervated by collars of LTMR terminals located just below the level of the sebaceous gland in both rodents and primates. The outer region of this sensory collar contains circumferential endings, whose physiological properties and functions remain unknown (Biemesderfer et al., 1978; Rice and Munger, 1986). The inner region is composed of three types of longitudinal lanceolate terminals, comb-like protrusions aligned parallel to the hair follicle. These longitudinal lanceolate endings, belonging to Aβ RA-LTMRs, Aδ-LTMRs, and C-LTMRs, are all sensitive to hair deflection and light touch of the skin, yet they have distinct tuning properties and conduction velocities (Brown and Iggo, 1967; Iggo, 1960). Similar to Aβ RA1-LTMRs associated with Meissners' corpuscles in glabrous skin, lanceolate Aβ RA-LTMRs and Aδ-LTMRs are rapidly adapting and sensitive to movement and low frequency vibration, despite slight differences in tuning properties (Brown and Iggo, 1967; Koltzenburg et al., 1997; Lechner and Lewin, 2013). In rodent trunk skin, lanceolate C-LTMRs are intermediately adapting. Their electrophysiological properties resemble those of C-LTMRs in humans, which are optimally tuned to stroking of the skin at rates that are deemed pleasurable, thus implicating lanceolate C-LTMRs in "emotional touch" (Löken et al., 2009; Vallbo et al., 1993).

Despite their differences in sensitivity and encoding, the three types of lanceolate ending LTMRs have virtually identical terminal structures (Li and Ginty, 2014; Li et al., 2011). All lanceolate terminals are shaped like flattened cylinders and are sandwiched between two or three terminal Schwann cell processes. The inner face of the axon directly abuts the basal lamina of

hair follicle outer root sheath cells, with no intervening Schwann cell process, enabling a close apposition of LTMR axon terminal membranes and hair follicle keratinocytes (Figure 1.2D). Longitudinally-oriented collagen fibers fill the extracellular space between and around each lanceolate ending-terminal Schwann cell unit, which may provide structural support for the lanceolate complex (Li and Ginty, 2014; Yamamoto, 1966).

How does hair deflection result in excitation of LTMR lanceolate endings, and subsequently, LTMR firing? Electron microscopy has demonstrated that large numbers of hemidesmosomes are distributed along hair follicle epithelial cell membranes, and fine filaments appear to project from these hemidesmosomes to directly contact both LTMR lanceolate endings and terminal Schwann cell processes (Figure 1.2E) (Li and Ginty, 2014). These filaments may serve to either simply anchor axon terminals to hair follicles, or perhaps function as a kind of protein tether necessary for mechanotransduction of lanceolate ending LTMRs. The 'protein tether' hypothesis posits a mechanism analogous to that seen in the auditory system, where tip links that connect stereocilia of cochlear hair cells transduce stereocilia movements to the opening of force-gated ion channels (LeMasurier and Gillespie, 2005). In support of such a model for hair follicle lanceolate endings, protein tethers extend between cultured somatosensory neuron axons and fibroblasts, and chemical ablation of these tethers leads to a loss of mechanically activated currents (Hu et al., 2010). Thus a physical connection between hair follicle epithelial cells and LTMR lanceolate endings may underlie LTMR excitation during hair deflection. Future challenges include understanding the contributions of hair follicle epithelial cells, terminal Schwann cells, and putative mechanical tethers in the transduction of hair deflection to LTMR excitation.

Taken together, anatomical, physiological, and pharmacology evidences have support that particular mechanical response properties of LTMR subtypes are determined by the unique geometry of their axonal terminals and associated end organs, including the Merkel ending/Aβ

SA1-LTMR, Meissner corpuscle/Aβ RA1-LTMRs, Pacinian corpuscle/Aβ RA2-LTMRs, and Lanceolate ending/LTMR complex. The least understood LTMR subtype, Aβ Field-LTMRs, are sensitive to gentle stroking of the skin but rarely respond to deflection of individual hairs (Horch et al., 1977). However, the terminal structure and skin arborization patterns of Aβ Field-LTMRs have not been determined, leaving open the question of how these distinct properties arise. In my thesis research, I attempted to determine the structural basis of the unique response properties of Aβ Field-LTMRs using a combination of anatomical, physiological, and mathematical modeling approaches, asking how does the ultrastructure and morphology of individual Aβ Field-LTMR terminals underlie their unique mechanical sensitivity.

Figure 1.2 Schematic images reveal the ultrastructure feature of LTMR end organs of glabrous skin and hairy skin. (Image adapted from Zimmerman et al., 2014)

(A) Cytoplasmic protrusions of the Merkel cell and hemidesmosomes physically link Merkel cells to surrounding epithelial cells. Dense-core vesicles are located inside the Merkel cell in close proximity to the enlarged axon terminal and are thought to be involved in signaling between the Merkel cell and the neurite (white arrows).

(B) Meissner corpuscles are located within dermal papillae and are innervated by one or more Aβ RA1-LTMRs. The external capsule is linked to both the lamellar cells and the epidermis via collagen fibers.

(C) Pacinian corpuscles are located in the deep dermis, contain layered lamellar cells, and are innervated by a single Aβ RA2-LTMR. Axonal protrusions project from the neurite into the cleft between inner-core lamellar cells and are thought to be the sites of generator potentials. Longitudinal and circumferential collagen fibers anchor the inner core and outer zone, respectively.

(D) Innervation pattern of Awl/auchene hair follicles. Terminal Schwann cells surround all three types of interdigitated lanceolate endings, as well as the circumferential endings.

(E) Cross-sectional view of (B), based on EM analysis. Terminal Schwann cells surround lanceolate endings on either side, with a gap in coverage facing the hair follicle hair cells. Putative protein tethers may connect hair follicle epithelial cells with LTMRs and terminal Schwann cells, while both longitudinal and circumferential collagen fibers provide a supporting role.

Figure 1.2

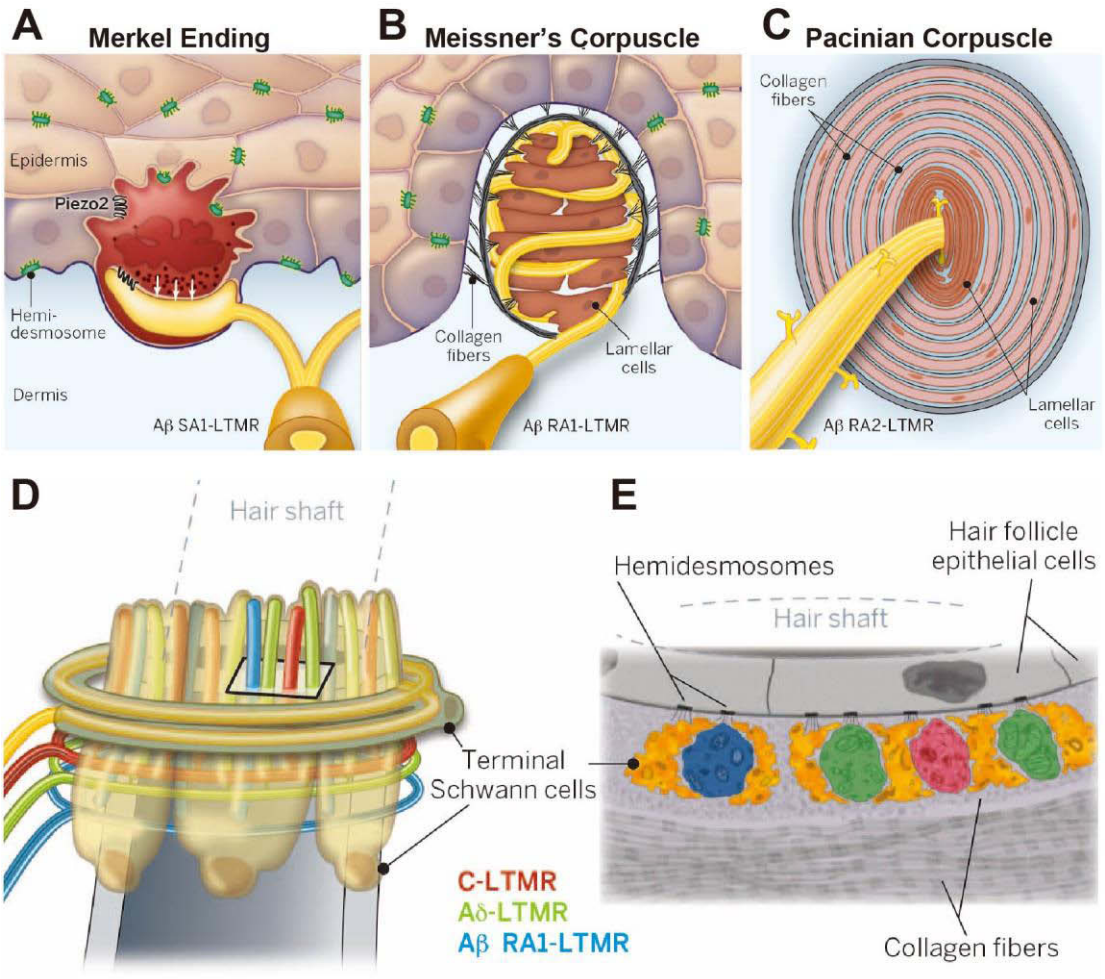
A
Merkel Ending
Epidermis
Piezo2
Hemi-
desmosome
Dermis
Aβ SA1-LTMR
B
Meissner's Corpuscle
Collagen
fibers
Lamellar
cells
Aβ RA1-LTMR
C
Pacinian Corpuscle
Collagen
fibers
Lamellar
cells
Aβ RA2-LTMR
D
Hair shaft
Terminal
Schwann cells
C-LTMR
Aδ-LTMR
Aβ RA1-LTMR
E
Hemidesmosomes
Hair follicle
epithelial cells
Hair shaft
Collagen fibers

1.3. Ascending circuits for touch sensation

Information of touch stimuli is firstly encoded by LTMR subtypes that are tuned to different mechanical stimuli. Upon activation of cutaneous terminals of somatosensory neurons, sensory stimuli are transformed into action potentials that propagate via the central axonal branches of sensory neuron to the spinal cord dorsal horn and in some cases, the DCN, which are the first stages for sensory information integration and processing. The dorsal column (DC) of the spinal cord is a major ascending pathway that conveys touch information from the spinal cord to higher levels of the central nervous system (Figure 1.3). Axons ascend through the DC to innervate the DCN in the brainstem. From there, DCN projection neurons convey information to the several targets including thalamus, superior colliculus, and cerebellum.

There are mainly two touch ascending pathways traveling through the DC to the DCN (Abraira and Ginty, 2013). On one hand, Aβ-LTMRs send out collaterals not just to the spinal cord; one axonal branch also ascends through the DC directly to the DCN (Figure 1.3). The axonal projections of Aβ-LTMRs are organized somatotopically in the DCN, whereby caudal neurons innervate the medial region of DCN and rostral neurons innervate the lateral region.

On the other hand, there is a population of spinal cord projection neurons that send axons through the DC to the DCN. These neurons are located in the deep lamina of spinal cord dorsal horn and receive input from primary somatosensory neurons (Figure 1.3) (Britain, 1988; Cliffer and Cliffer, 1985; Madsen, 1984). These neurons are named “PSDC” neurons, the post-synaptic dorsal column neurons, and the ascending axons from PSDC neurons are collectively called the “indirect pathway”. Decades ago, blind recordings were made from PSDC neurons in anaesthetized cat and showed that they response to cutaneous mechanical stimuli, either low threshold or high threshold (Britain, 1988). However, PSDC neurons have been ignored in textbooks and recent studies, and how their ascending projections, together with Aβ-LTMRs, are

organized in the DCN is largely unknown and their functions have not yet been revealed. In my thesis research, I attempted to gain insight how information is processed in the DCN, the first relay nuclei of touch information in the brainstem (Chapter 5).

Figure 1.3 Schematic image reveals the dorsal column ascending pathways.

Afferents from different types of sensory neurons innervate different target in the central nervous system. C-LTMRs, Aδ-LTMRs, and nociceptors innervate the superficial laminae of the dorsal horn from laminae I-III. Aβ-LTMRs innervate deep laminae of dorsal horn (from III-V) and further bifurcate and send axons through the dorsal column (DC) to innervate the dorsal column nuclei (DCN) in the brainstem. In the spinal cord, post-synaptic dorsal column neurons (PSDCs) also ascend through the DC to innervate the DCN. The ascending projections from the Aβ-LTMRs and PSDC neurons are named as “direct pathway” and “indirect pathway”, respective.

Figure 1.3

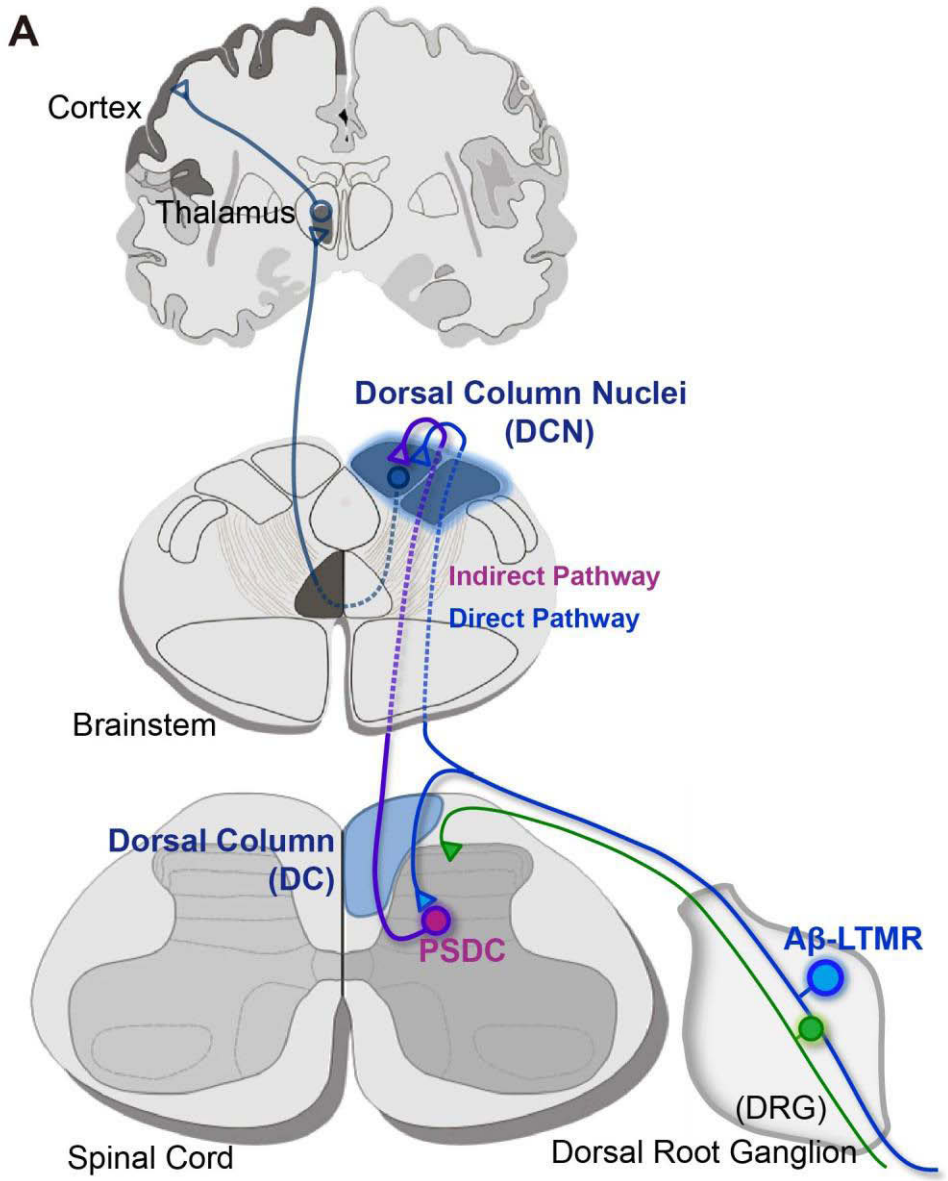
A
Cortex
Thalamus
Dorsal Column Nuclei
(DCN)
Indirect Pathway
Direct Pathway
Brainstem
Dorsal Column
(DC)
PSDC
Aβ-LTMR
(DRG)
Dorsal Root Ganglion
Spinal Cord

1.4. Spinal cord circuits underlying traumatic peripheral neuropathic pain

Traumatic peripheral neuropathic pain is a chronic debilitating pain state that is caused by an injury of the peripheral axons of primary sensory neurons and that persists long after the initial insult (Campbell and Meyer, 2006). Peripheral neuropathic pain can result from complications after surgeries or injury from a traumatic accident, and depending on the condition of injuries, it may present a great variety of features that decreases the quality of life of the patients, including 1) widespread or attacks of pain without seeming provocation (spontaneous pain), 2) pain to light stroking of the skin (mechanical allodynia or hyperalgesia), 4) hypersensitivity to thermal stimuli, especially cooling stimuli (thermal hyperalgesia).

Great efforts have been made to understand the mechanisms underlying traumatic peripheral neuropathy, and multiple alterations along the somatosensory system have been implicated to explain abnormal pain during peripheral neuropathy (Figure 1.4). Abnormalities may occur in injured and uninjured sensory afferent supplying the affected region, which can be modulated by an alteration of growth factors acting on the sensory or sympathetic nervous system, or through expression of channels/receptors controlling signal transduction. On the other hand, central sensitization, which has mainly been addressed in spinal cord, may also occur following peripheral nerve injury, including alterations of presynaptic release properties, postsynaptic receptors, local spinal cord circuits, and descending modulation. Finally, an immune response has recently been implicated, acting both peripherally and centrally.

A big issue of traumatic peripheral neuropathy is the difficulty of treatment. Medicines that are widely used to control other types of pain are not effective on peripheral traumatic neuropathic pain, including local analgesic drugs like lidocaine, corticosteroids drugs, nonsteroidal anti-inflammatory drugs (NSAIDs), and opioid drugs like morphine (Lee et al., 1995; Bian et al., 1999). Therefore, it is crucial to understand the neural circuitry underlying abnormal

pain sensations produced by traumatic neuropathic pain in order to identify potential targets for therapy. Recently, molecular genetic studies have identified several components of spinal cord local circuits underlying development of peripheral traumatic neuropathic pain (Peirs et al., 2015; Petitjean et al., 2015). However, the ascending pathways carrying pathological pain information to the brain have not yet been identified or examined.

Classic lesion studies in cats, non-human primates, and human patients have revealed that the DC pathways are mainly involved in discriminative touch sensation. In contrast, another major ascending pathway of the somatosensory system, the anterolateral tract (ALT), is known for conveying temperature, itch and pain information to the brain. The ALT originates from spinal cord projection neurons in lamina I or lamina IV, and ALT axons travel through ventral or lateral regions of the spinal cord and to innervate several brain regions including the parabrachial nuclei, periaqueductal gray, superior colliculus, and thalamus (Basbaum et al., 2009). It has been widely accepted that the ALT conveys cutaneous pain under most pathological conditions due to its important role in pain sensation under non-pathological status, though this hypothesis lacks direct evidence. In addition, two studies have recently suggested an involvement of the dorsal column pathway in the peripheral neuropathic pain. In rat, mechanical hypersensitivity induced by peripheral nerve injury was abolished by a dorsal column lesion, as well as by anesthetic applied directly to the DCN (Ossipov et al., 2002; Sun et al., 2001). However, these studies have been largely ignored by peripheral neuropathic pain researchers, and the ALT is still considered the main ascending pathway for peripheral neuropathy. Based on these prior experiments, and the fact that peripheral neuropathic pain is difficult to be treated by traditional analgesic drugs, I hypothesized that peripheral neuropathic pain may develop through a non-traditional pain pathway, the DC pathway. In the last part of my thesis (Chapter 6), I will examine the function of the two major somatosensory ascending pathways in the development of peripheral neuropathy, and further dissect the spinal cord circuits that are involved in this process.

Figure 1.4 Mechanisms underlying peripheral neuropathic pain.

A schematic image summarizes the major mechanisms underlying peripheral neuropathic pain, their location, and the triggers responsible for their activation. (Image adapted from Costigan et al., 2009)

Figure 1.4

A

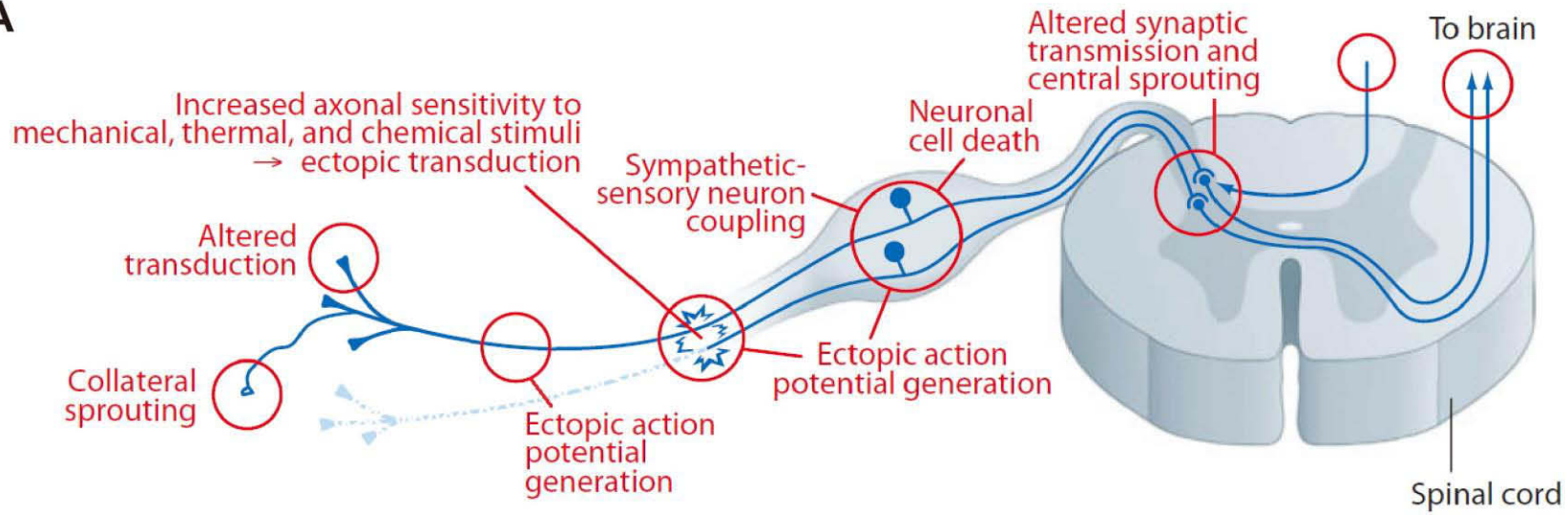
Increased axonal sensitivity to mechanical, thermal, and chemical stimuli → ectopic transduction
Altered transduction
Collateral sprouting
Ectopic action potential generation
Sympathetic-sensory neuron coupling
Ectopic action potential generation
Neuronal cell death
Altered synaptic transmission and central sprouting
To brain
Spinal cord

Chapter 2. Genetic identification of Aβ Field-LTMRs

All LTMRs have a central axonal projection that innervates the spinal cord dorsal horn. Undirected recordings indicate that five Aβ LTMR subtypes, including the Aβ Field-LTMR, also have an axonal branch that ascends via the DC to the DCN in the brainstem (Horch et al., 1976), and these projections are considered important for the perception of discriminative touch (Ballermann et al., 2001; Dobry and Casey, 1972). Here we have taken an unbiased retrograde labeling approach to visualize the cutaneous endings of Aβ LTMRs with axons that ascend the DC to the brainstem of mice. These experiments guided molecular-genetic strategies to label the Aβ LTMRs for which genetic tools do not currently exist, specifically Aβ SA1-LTMRs as well as large myelinated cutaneous sensory neurons with circumferential endings that are later identified as the elusive Aβ Field-LTMRs.

2.1. Identification of cutaneous LTMRs that innervate the DCN

To visualize the cutaneous terminal morphologies of uncharacterized Aβ-LTMR subtypes, we designed an unbiased retrograde labeling strategy to selectively label neurons exhibiting direct DCN projections. AAV2/1-Cre virus was injected bilaterally into the rostral DC at the first cervical level of $R26^{LSL\text{-}tdTomato}$ mice to retrogradely infect DRG neurons and visualize their cutaneous axonal projections (Figure 2.1A). TdTomato$^+$ thoracic and lumbar DRG neurons have large cell bodies (650 ± 23 μm^2) and are neurofilament-heavy chain$^+$ (NFH$^+$) (99.9 ± 0.1%; Figure 2.1C), but they do not bind to the lectin IB4 and very few express CGRP (0% and 9 ± 1%, respectively; Figures 2.1E-F). These findings indicate that our retrograde labeling strategy is specific for neurons that have a branch extending via the DC to the DCN because small or medium sized DRG sensory neurons, including C-LTMRs, Aδ-LTMRs and most nociceptors, do not have an axonal branch that projects directly to the brainstem (Abraira and Ginty, 2013; Horch et al., 1976).

We next visualized the cutaneous projection patterns and terminal morphologies of tdTomato$^+$ neurons. In hairy skin, tdTomato$^+$ neurons form four types of endings. Close to the epidermis and between hair follicles, tdTomato$^+$ axonal terminals were observed wrapped by S100$^+$ Schwann cells (Figure 2.1G) in structures that resemble Pacinian corpuscles (Luo et al., 2009); however, unlike Pacinian corpuscles, these tdTomato$^+$ endings do not reside within the deep dermis. This is a curious neuronal population with unknown physiological properties. The other three types of tdTomato$^+$ axons observed form terminals associated with hair follicles. At the neck of guard hair follicles, tdTomato$^+$ axonal endings associate with Troma1$^+$ Merkel cells (Figure 2.1H); these tdTomato$^+$ neurons are the well-described Aβ SA1-LTMRs. A third tdTomato$^+$ neuronal population forms NFH$^+$ longitudinal lanceolate endings (98 ± 1% of these endings are NFH$^+$) that wrap around hair follicles just below the level of the sebaceous gland (Figure 2.1I); these neurons are Aβ RA-LTMRs. A fourth class of tdTomato$^+$ DRG neurons displays circumferential endings that also encircle hair follicles below the sebaceous gland (Figure 2.1I). Similar to Aβ SA1-LTMR and Aβ RA-LTMR endings, the majority of tdTomato$^+$ circumferential endings are NFH$^+$ (99.5 ± 0.5%) (Figure 2.1I), suggesting these neurons have large caliber, myelinated axons with conduction velocities in the Aβ range. Whole-mount staining of back hairy skin revealed that NFH$^+$ circumferential endings innervate 94 ± 3% of hair follicles, whereas Aβ RA- and SA1-LTMRs innervate only 8 ± 2% and 0.8 ± 0.2% of hair follicles, respectively (Figure 2.1B). Thus, we have identified a DCN-projecting DRG neuronal population with a striking preponderance of NFH$^+$ circumferential endings in hairy skin of mice.

Neurons with circumferential endings in rodents were first described in the 1980s (Millard and Woolf, 1988; Rice and Munger, 1986), although their physiological and functional properties are unknown. To ask whether neurons with NFH$^+$ circumferential endings are restricted to rodents, we next examine the hairy skin of several mammalian species. A comparative study of mice, cats, dogs and marmosets indicates that neurons with NFH$^+$

circumferential endings are found in each of these species (Figure 2.2). Thus, NFH^+ circumferential ending neurons are a prevalent neuronal population amongst mammalian species.

Just as there are multiple sensory neuron subtypes with longitudinal lanceolate endings, experiments examining expression patterns of molecular markers showed there are multiple neuronal types with circumferential endings (Fünfschilling et al., 2004). Indeed, we found that in mouse hairy skin, there are two molecularly distinct types of circumferential endings, one expressing CGRP and the other expressing NFH (Figure 2.3). To visualize the terminal morphologies of $CGRP^+$ DRG neurons, we used a BAC transgenic mouse line, *CGRP-GFP,* in which the pattern of GFP expression recapitulates that of endogenous CGRP (Figure 2.3A-B). Whole-mount staining of hairy skin from *CGRP-GFP* mice showed that nearly all hair follicles are innervated by both CGRP-GFP^+ (99.3 ± 0.1%) and NFH^+ circumferential endings (94 ± 3%, Figure 2.1B, 2.3B-C). By counterstaining with Tuj1, a tubulin protein that labels all sensory axons, we observed that essentially all circumferential endings are either $CGRP^+$ or NFH^+ (Figure 2.3D). Furthermore, the majority of circumferential endings labeled by DCN retrograde labeling are NFH^+ (99.5 ± 0.5%, Figure 2.1I, 2.3E) and are $CGRP^-$ (0%, Figure 2.3E) Together, these findings indicate that two DRG sensory neuron subtypes form circumferential endings in hairy skin, and that only those with NFH^+ circumferential endings project directly to the DCN. The dorsal column conveys discriminative touch, proprioceptive signals as well as visceral nociceptive information to the brain. Thus, we hypothesized that these skin innervating DRG neurons with NFH^+ circumferential endings are a novel Aβ-LTMR subtype.

2.2. Intersectional genetic strategies to selectively label neurons with NFH^+ circumferential endings and Aβ SA1-LTMRs

The molecular, anatomical, electrophysiological, and functional properties of DRG neurons with circumferential endings surrounding hair follicles are unknown. We therefore sought to generate

molecular genetic tools that enable investigation of these neurons. We first asked whether NFH^+ circumferential ending neurons express TrkC and cRet, which are receptors for neurotrophin-3 (NT3) and glial cell line-derived neurotrophic factor family members, respectively (Durbec et al., 1996; Lamballe et al., 1991; Trupp et al., 1996). TrkC is expressed in subsets of large diameter NFH^+ DRG neurons (Bardoni et al., 2014), and 53 ± 3% of DCN-projecting DRG neurons are $TrkC^+$ (Figure 2.1D). In addition, NT3-TrkC signaling mediates development of several DRG neuron subtypes, including neurons with NFH^+ circumferential endings (Albers et al., 1996; Krimm et al., 1999). We found that $TrkC^+$ DRG neurons of adult mice can be subdivided into three mutually exclusive populations based on their expression patterns of molecular markers. Approximately 35.9 ± 1.7% of $TrkC^+$ neurons are proprioceptors labeled by PV^{iCre}, 18.6 ± 1.5% are peptidergic nociceptors expressing CGRP, and the remaining 53.3 ± 1.3% express Ret (Figure 2.5A-B); this $TrkC^+/Ret^+$ population may include neurons with NFH^+ circumferential endings. In fact, $TrkC^+$ neurons do not overlap with Npy2r-GFP^+ neurons, nor do they express TrkB or tyrosine hydroxylase (TH), which are markers of Aβ RA-LTMRs, Aδ-LTMRs, and C-LTMRs, respectively (data not shown), suggesting that the $TrkC^+/Ret^+$ DRG population may include previously uncharacterized LTMR subtypes.

To define the morphological properties of $TrkC^+$ DRG neurons, we generated a $TrkC^{tdTomato}$ knock-in mouse line in which the coding determinants of tdTomato with an N-terminal myristoylation signal tag is inserted into the exon containing the first coding ATG of the *TrkC* gene (Figure 2.4A-B). In the DRG, the pattern of tdTomato expression recapitulates that of TrkC (Figure 2.4C), allowing us to use $TrkC^{tdTomato}$ mice to visualize the peripheral axonal terminals of $TrkC^+$ DRG neurons. Interestingly, in hairy skin, tdTomato is found in all NFH^+ circumferential endings; 100% of NFH^+ circumferential endings are $tdTomato^+$ while 98.0 ± 0.1% of $tdTomato^+$ circumferential endings are NFH^+ (Figure 2.4C and 2.5C). $TrkC^{tdTomato}$ also labels all Aβ SA1-LTMR endings associated with Merkel cells (100%, Figure 2.4E and 2.5D) as well as

a subset of free nerve endings (Figure 2.4E, thinner tdTomato$^+$ fibers, arrow heads). By crossing *TrkC^{tdTomato}* mice with *Ret^{CFP}*, we found that nearly all Merkel cell-associated endings and NFH$^+$ circumferential endings are both TrkC$^{tdTomato+}$ and Ret^{CFP+} (100% and 94.7 ± 1.5%, respectively) (Figure 2.4F, 2.5C-D), whereas TrkC$^{tdTomato+}$ free nerve endings are Ret^{CFP-} (data not shown). Thus, TrkC$^+$/Ret$^+$ DRG neurons of adult mice are Aβ SA1-LTMRs and NFH$^+$ circumferential ending neurons.

To selectively label the TrkC$^+$/Ret$^+$ DRG neuronal populations, we designed an intersectional genetic labeling strategy. For this, we generated a *TrkC^{CreER}* knock-in mouse line (Figure 2.4A-B), which expresses a tamoxifen-sensitive form of Cre recombinase in TrkC$^+$ neurons. When *TrkC^{CreER}* mice were crossed with *Ret$^{f(CFP)}$* mice (Uesaka et al., 2008), which express CFP under the control of the endogenous *Ret* locus following Cre-mediated recombination (Figure 2.6A), tamoxifen treatment promoted CFP expression exclusively in TrkC$^+$ cells (95.6 ± 1.3% and 100%, Figure 2.6E, 2.6H). Interestingly, we found that treatment of *TrkC^{CreER}; Ret$^{f(CFP)}$* mice with 0.1 mg of tamoxifen at P5 led to expression of CFP in the majority of NFH$^+$ circumferential endings (79.6 ± 3.3%; Figure 2.6B-C), but not in other populations, including PV$^+$ proprioceptors (0%, Figure 2.6G), CGRP$^+$ peptidergic nociceptors (1.7 ± 0.1%, Figure 2.6F), Aβ SA1-LTMRs with Merkel endings (7 ± 4%, Figure 2.6B), Aβ RA-LTMRs (0%, Figure 2.6B), or free nerve endings (data not shown). Based on the efficiency of terminal labeling and the percentage of labeled NeuN$^+$ DRG neurons, we estimate that neurons with NFH$^+$ circumferential endings represent 4.3 ± 0.3% of all thoracic DRG neurons (3853 neurons counted in 4 animals), which is comparable to the density of Aβ RA-LTMRs and Aδ-LTMRs (Li et al., 2011).

In contrast, due to the dynamic and differential expression of TrkC in DRG neuron subtypes (data not shown), treatment of *TrkC^{CreER}; Ret$^{f(CFP)}$* mice with 3 mg of tamoxifen at E12.5

led to expression of CFP exclusively in 40 ± 4% of Merkel endings that are derived from Aβ SA1-LTMRs (Figure 2.6B, 2.6D), but not in other populations, including PV^+ proprioceptors (2.2 ± 0.2%, Figure 2.6J), $CGRP^+$ peptidergic nociceptors (0%, Figure 2.6I), Aβ RA-LTMRs with NFH^+ lanceolate endings (0%, Figure 2.6B), NFH^+ circumferential endings (0%, Figure 2.6B) or free nerve endings (data not shown). Thus, the tamoxifen-inducible $TrkC^{CreER}$; $Ret^{f(CFP)}$ intersectional genetic strategy enables selective labeling of either Aβ SA1-LTMRs or neurons with NFH^+ circumferential endings, depending on the time of tamoxifen delivery.

2.3. Neurons with NFH^+ circumferential endings are Aβ Field-LTMRs sensitive to gentle stroking of the skin but are relatively insensitive to skin indentation

In order to evaluate the physiological properties of NFH^+ circumferential ending neurons, we developed a targeted *in vivo* electrophysiological recording paradigm (Figure 2.7A, See Experimental Procedures). We crossed $TrkC^{CreER}$; $Ret^{f(CFP)}$ with a dual recombinase dependent reporter line $R26^{LSL\text{-}FSF\text{-}tdTomato}$ (*Ai65*) and intradermally injected an AAV2/1-Flpo virus to label $TrkC^+$ neurons innervating the dorsal surface of the thigh. This allowed us to confine our recordings to NFH^+ circumferential neurons innervating a small region of hairy skin amenable to mechanical stimulation. Recently, NFH^+ circumferential ending neurons were suggested to function as Aδ-mechanonociceptors on the basis of *ex vivo* recordings from a mixed population of DRG neurons labeled by DOR^{GFP+} (Bardoni et al., 2014). Our intersectional genetic strategy allowed us to unambiguously and quantitatively explore the link between the structure and function of NFH^+ circumferential ending neurons.

We first assessed responsiveness of NFH^+ circumferential ending neurons to skin stroke. Upon gentle stroking of the skin in the rostral to caudal direction with a fine brush (average holding force of 5 mN, 1-10 mm/sec sweep velocity), NFH^+ circumferential ending neurons showed robust responses with an action potential firing frequency that equaled or exceeded those

of Aβ RA-LTMRs and Aβ SA1-LTMRs labeled using *Npy2r-GFP* mice and *TrkC*^{CreER}*; Ret*$^{f(CFP)}$ mice treated with tamoxifen at E12.5, respectively (Figure 2.7B-C). Moreover, electrical stimulation of the skin with a bipolar electrode demonstrated that NFH$^+$ circumferential ending neurons have a conduction velocity of 17.0 ± 2.0 m/sec (Figure 2.7D), which is indistinguishable from the conduction velocities of Aβ RA-LTMRs and Aβ SA1-LTMRs, respectively (Figure 2.7D). Thus, NFH$^+$ circumferential ending neurons are Aβ-LTMRs highly sensitive to gentle skin stroke.

Interestingly, although NFH$^+$ circumferential ending neurons are highly sensitive to gentle stroking of the skin, they exhibit a much higher force threshold than Aβ RA-LTMRs and SA1-LTMRs (Figure 2.7E) when the skin is indented with von Frey filaments. These responses exhibited considerable trial-to-trial variability, therefore we next used a force-controlled stimulator which could be precisely and consistently positioned over the skin. We found that each NFH$^+$ circumferential ending neuron's receptive field displayed "hotspots", which we subsequently targeted to assess indentation responses. NFH$^+$ circumferential ending neurons exhibited distinct adaptation properties compared to Aβ SA1-LTMRs and Aβ RA-LTMRs. At forces near threshold their responses adapted rapidly over tens of milliseconds, while at higher forces adaptation responses to indentation steps became intermediate between Aβ SA1-LTMRs and Aβ RA-LTMRs (Figure 2.7F). NFH$^+$ circumferential ending neurons also show few or no off responses, which are a hallmark of Aβ RA-LTMRs (Figure 2.7F), suggesting they belong to an Aβ-LTMR population with intermediate adaptation properties.

We also made intracellular recordings from NFH$^+$ circumferential neurons using an *ex vivo* preparation. These recordings revealed inflected somal action potentials that were broader than the uninflected somal action potentials of Aβ RA-LTMRs (Figure 2.8A). Consistent with the *in vivo* recordings, individual receptive fields were composed of multiple hotspots. Application of

controlled forces using a blunt probe (1 mm diameter) centered over a hotspot revealed that NFH^+ circumferential neurons have an indentation threshold about 5 mN (Figure 2.8C), which is considerably higher than that of both Aβ RA-LTMRs and Aβ SA1-LTMRs (McIlwrath et al., 2007). Moreover, indentation responses became more slowly adapting and firing rates increased as forces increased into the noxious range (Figure 2.8C). These neurons responded far more vigorously when the same hotspots were indented with sharp probes (Figure 2.8D), and even more robustly when coaxial forces were applied to individual hairs (hair pull) in the hotspot (Figure 2.8E). Thus, while NFH^+ circumferential neurons are highly responsive to gentle skin stroking, and are therefore an LTMR, these neurons also exhibit hallmarks of myelinated nociceptors (Burgess and Perl, 1967; Djouhri and Lawson, 2004; Koerber et al., 1988).

Both Aβ RA-LTMRs and Aβ Field-LTMRs are hairy skin innervating, predominantly rapidly adapting LTMR subtypes that are sensitive to skin stroking. Unlike Aβ RA-LTMRs, Aβ Field-LTMRs do not respond to deflection of individual guard hairs (Horch et al., 1977). Therefore, we next performed *in vivo* recordings to ask whether NFH^+ circumferential ending neurons are sensitive to guard hair deflection by moving a brush across the tips of guard hairs, which extend beyond awl/auchene and zigzag hairs. In all cases tested, this stimulus elicited bursts of spikes in Aβ RA-LTMRs but failed to excite NFH^+ circumferential ending neurons (Figure 2.7G-H). Taken together, the NFH^+ circumferential ending neuron is an Aβ-LTMR that is exquisitely sensitive to gentle stroking of the skin, relatively insensitive to skin indentation, with a rapidly adapting discharge at low to moderate indentation forces, and insensitive to deflection of guard hairs. Thus, the properties of NFH^+ circumferential ending neurons match those of both classically defined Aβ Field-LTMRs (Burgess et al., 1968) as well as a subset of myelinated nociceptors (Burgess and Perl, 1967), and are hereafter referred to simply as Aβ Field-LTMRs.

Figure 2.1 Genetic identification of sensory neurons that innervate the DCN.

(A-I) The rostral cervical DC of $R26^{LSL\text{-}tdTomato}$ mice was injected with AAV2/1-Cre virus to retrogradely label neurons that project to the DCN. Schematic of the retrograde labeling strategy is revealed in (A).

(B) NFH^+ circumferential endings, NFH^+ lanceolate endings, and Merkel endings innervate 94 ± 3%, 8 ± 2%, and 0.8 ± 0.2% of hair follicles, respectively (3964 hair follicles from 3 mice).

(C-F) Double immunostaining of NFH and tdTomato (C), TrkC and tdTomato (D), IB4 and tdTomato (E), CGRP and tdTomato (F) on adult thoracic DRG sections. The majority of $tdTomato^+$ DRG neurons are NFH^+ (99.9 ± 0.1%, 958 neurons from 3 mice) with large cell bodies (650 ± 23 μm^2, 327 neurons from 3 mice). Subsets of $tdTomato^+$ DRG neurons are $TrkC^+$ (53.0 ± 2.7%, 984 neurons from 3 mice). The majority of $tdTomato^+$ DRG neurons do not bind to IB4 (0%) or express CGRP (9.5 ± 1.1%; 958 or 984 neurons from 3 mice).

(G-I) In hairy skin, at least 4 types of terminals are labeled by tdTomato: an unknown ending type innervating $S100^+$ terminal organs that resemble Pacinian corpuscles (G), Merkel endings from Aβ SA1-LTMRs that associate with $Troma1^+$ Merkel cells (H), lanceolate endings that are NFH^+ (97.8 ± 1.2%, 156 terminals from 3 mice) and derived from Aβ RA-LTMRs (I, asterisk), as well as circumferential endings that are also NFH^+ (99.5% ± 0.5%, 465 terminals from 3 mice) (I, arrowhead).

Scale bar: 50 μm (C-I).

Figure 2.1

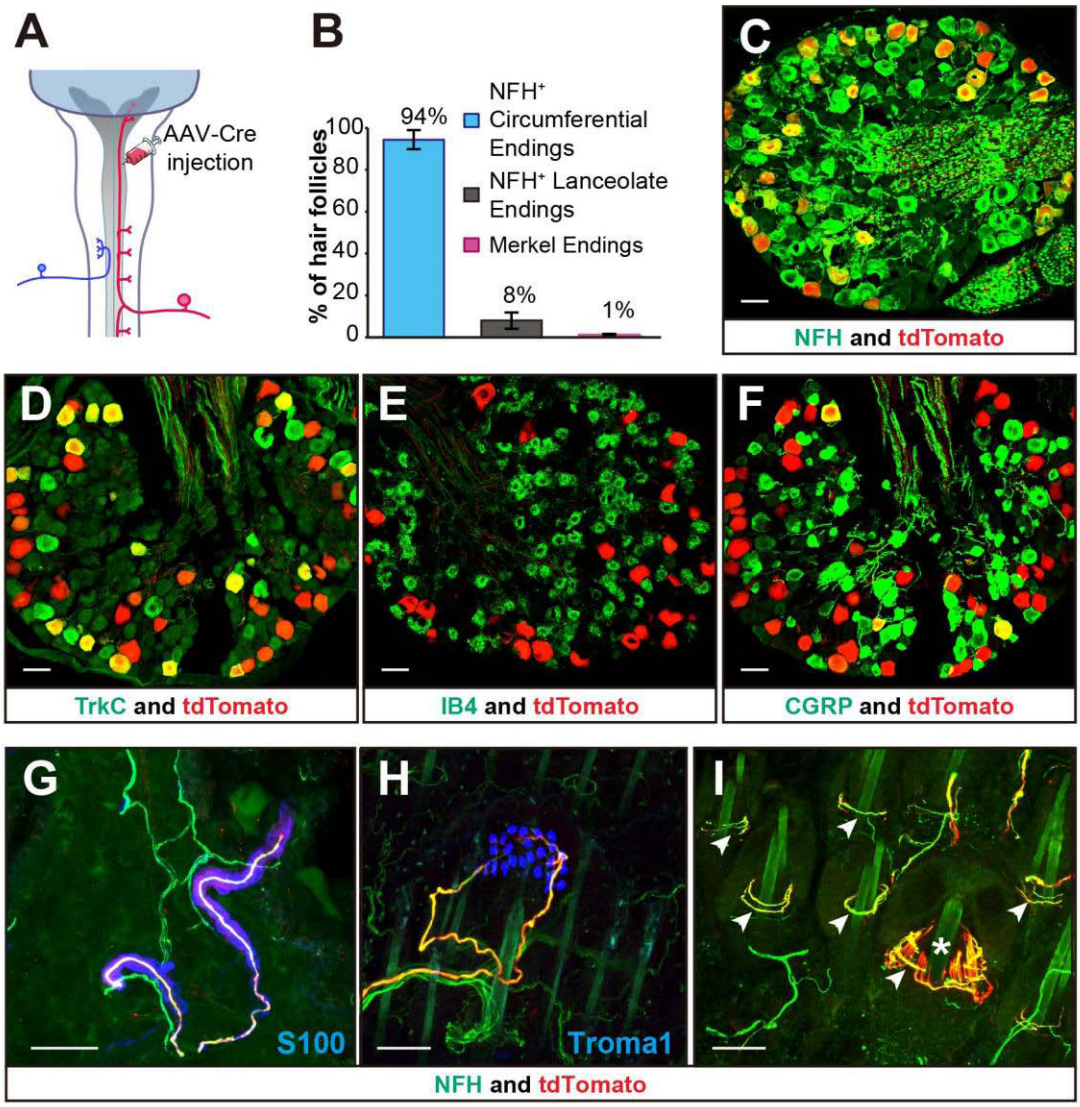
A
AAV-Cre injection
B
% of hair follicles
100
80
60
40
20
0
94%
8%
1%
NFH+ Circumferential Endings
NFH+ Lanceolate Endings
Merkel Endings
C
NFH and tdTomato
D
TrkC and tdTomato
E
IB4 and tdTomato
F
CGRP and tdTomato
G
S100
H
Troma1
I
NFH and tdTomato

Figure 2.2 NFH^+ circumferential ending neurons are a prevalent neuronal population amongst mammalian species

(A-D) Immunostaining of NFH and Tuj1 on hairy skin sections reveals that NFH^+ circumferential endings (arrowhead) can be found in mouse (A), cat (B), dog (C), and marmoset (D).

Scale bar: 50 μm (A-D).

Figure 2.2

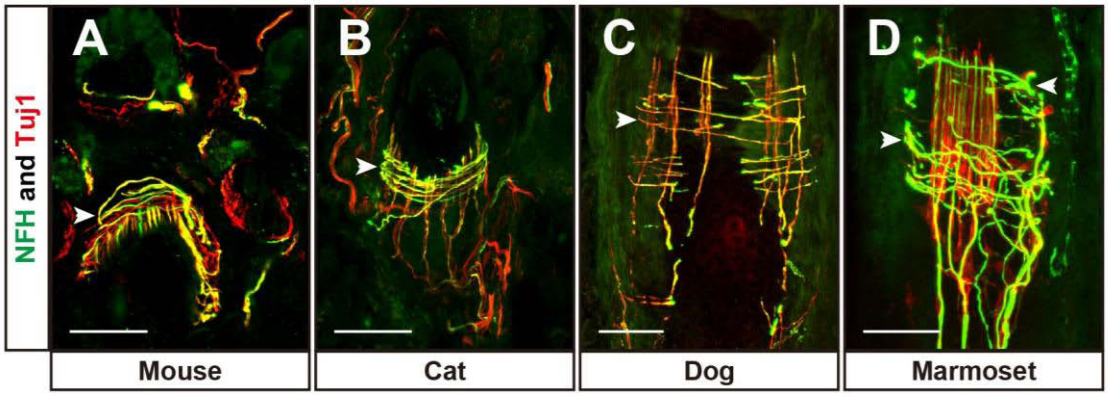

Figure 2.3 Characterization of two types of circumferential endings

(A) Double immunostaining of GFP and CGRP on adult thoracic DRG sections of *CGRP-GFP* mice reveals that the GFP specifically recapitulate the endogenous expression pattern of CGRP. 94% of GFP^+ neurons are $CGRP^+$, while 83% $CGRP^+$ neurons are GFP^+ (n = 4 mice).

(B) Whole-mount immunostaining of GFP and CGRP of hairy skin from *CGRP-GFP* mice reveals that all the GFP^+ circumferential endings are $CGRP^+$ and vice versa (n = 5 mice).

(C) Whole-mount immunostaining of GFP and NFH of hairy skin from *CGRP-GFP* mice reveals that all hair follicles are wrapped up by two types of circumferential endings express either CGRP or NFH (99.3 ± 0.1% and 94 ± 3%, respectively, 3964 hair follicles from 3 animals). Careful analysis of confocal z-stacks images shows that these two types of circumferential endings do not overlap with each other. Note the yellow color is due to the proximity of these fibers, which results in overlap in the z-axis projection.

(D) In hairy skin sections from *CGRP-GFP* mice, NFH^+ circumferential endings (red) and CGRP-GFP^+ circumferential endings (green) are virtually excluded from each other and cover all circumferential endings labeled by Tuj1 (Blue) (n = 3 animals).

(E) Immunostaining of CGRP, tdTomato, and NFH on adult back hairy skin sections of $R26^{LSL\text{-}tdTomato}$ mice 3 weeks after AAV2/1-Cre DC injection. Nearly all $tdTomato^+$ circumferential endings are NFH^+ (99.5% ± 0.5%) and $CGRP^-$ (0%).

Scale bar: 50 μm (A-E).

Figure 2.3

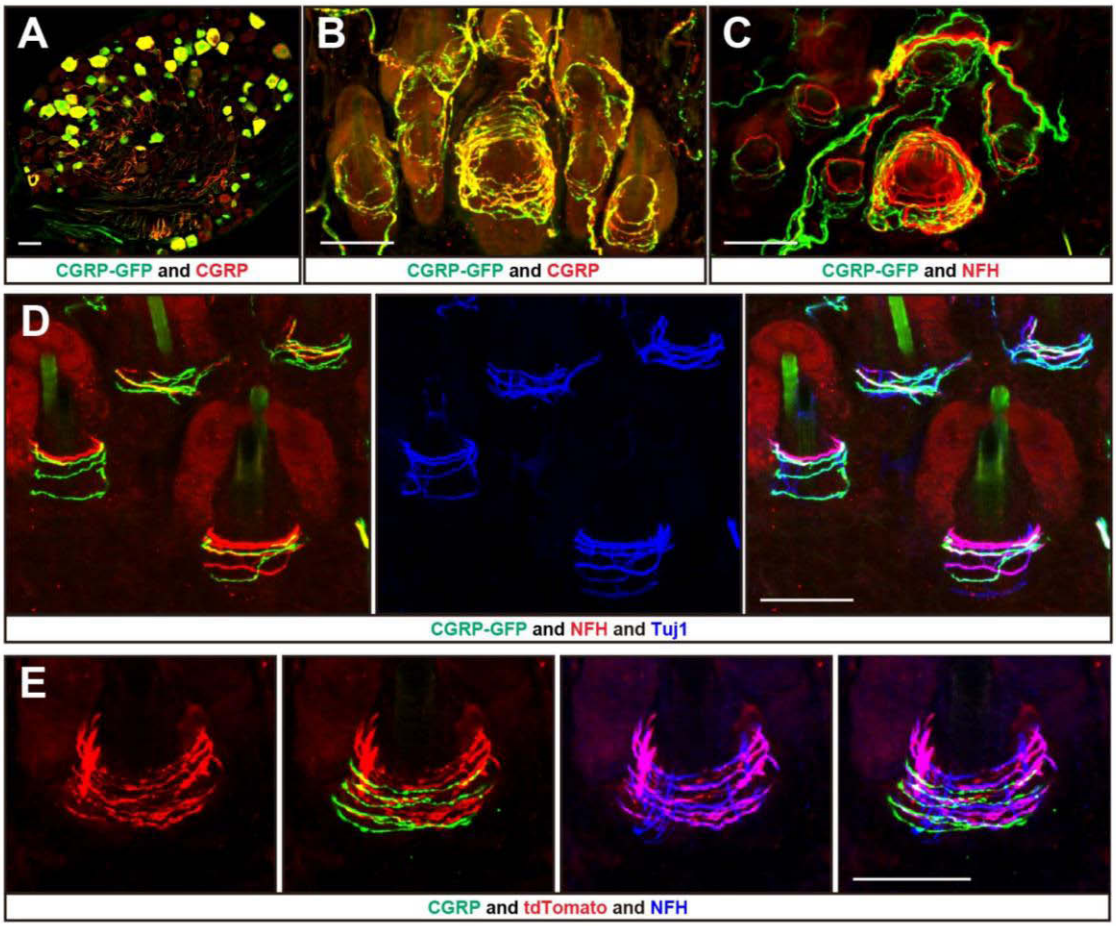
A
B
C
CGRP-GFP and CGRP
CGRP-GFP and CGRP
CGRP-GFP and NFH
D
CGRP-GFP and NFH and Tuj1
E
CGRP and tdTomato and NFH

Figure 2.4 Generation of *TrkC* knock in mice and characterization of the peripheral terminals labeled by TrkC or Ret.

(A) *TrkC* targeting strategy. Top: WT *TrkC* gene; bottom: targeted *TrkC* gene with a neomycin cassette flanked by *frt* sites. Yellow rectangles: 5' UTR or coding region of *TrkC*; red arrow: *tdTomato* with myristoylation signal tag or *CreER* cassettes; grey arrow: Neomycin cassette; grey arrowheads: *frt* sites. The bar labeled "5' probe" or "Neo probe" indicates the location of probes for Southern blot hybridization.

(B) Southern confirms the $TrkC^{tdTomato}$ or $TrkC^{CreER}$ cassettes are specifically knocked into the *TrkC* locus. Homozygous $TrkC^{tdTomato}$ or $TrkC^{CreER}$ mice die at early postnatal age.

(C) Double immunostaining of TrkC and tdTomato of adult DRG sections from $TrkC^{tdTomato}$ mice reveals the expression of tdTomato specifically recapitulate the endogenous expression pattern of TrkC.

(D-E) Immunostaining of NFH, tdTomato, and Troma1 of hairy skin sections from $TrkC^{tdTomato}$ mice reveals that tdTomato labels 100% of NFH^+ circumferential endings (D) (401 terminals from 4 animals), 100% Merkel endings (58 terminals from 4 animals), and some free nerve endings (arrow heads) (E). Note the $tdTomato^+$ free nerve endings are thinner and weaker than other labeled endings.

(F) Immunostaining of CFP, NFH, and Troma1 of hairy skin sections from Ret^{CFP} mice reveals that CFP labels 98.0 ± 1.4% NFH^+ circumferential endings and 100% of Merkel endings (401 terminals and 58 terminals, respectively, from 4 animals).

Scale bar: 50 μm (C-F).

Figure 2.4

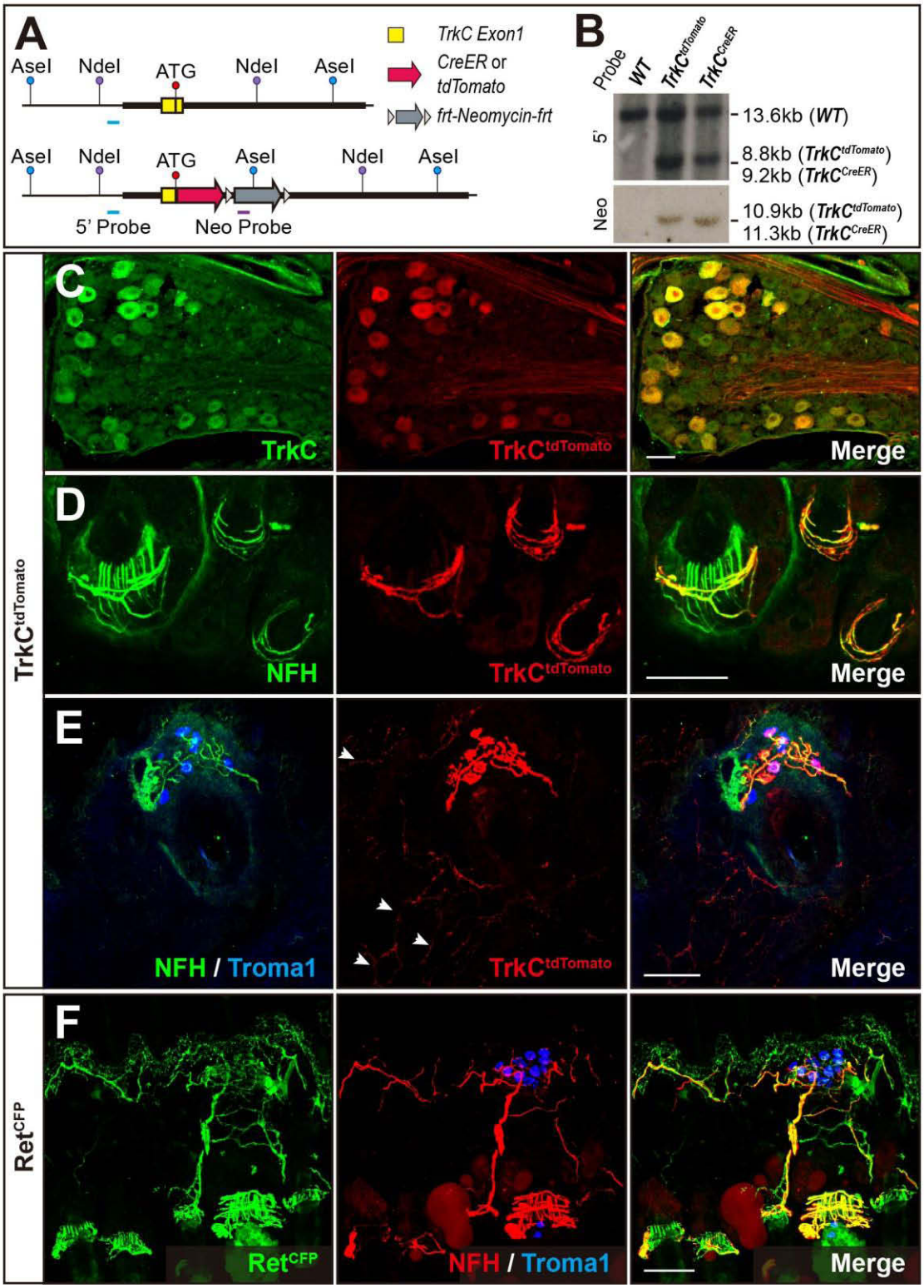
A
AseI
NdeI
ATG
NdeI
AseI
TrkC Exon1
CreER or
tdTomato
frt-Neomycin-frt
AseI
NdeI
ATG
AseI
NdeI
AseI
5' Probe
Neo Probe
B
Probe
WT
TrkCtdTomato
TrkCCreER
5'
13.6kb (WT)
8.8kb (TrkCtdTomato)
9.2kb (TrkCCreER)
Neo
10.9kb (TrkCtdTomato)
11.3kb (TrkCCreER)
TrkCtdTomato
C
TrkC
TrkCtdTomato
Merge
D
NFH
TrkCtdTomato
Merge
E
NFH / Troma1
TrkCtdTomato
Merge
RetCFP
F
RetCFP
NFH / Troma1
Merge

Figure 2.5 Characterization of the TrkC$^+$ and Ret$^+$ neurons and their peripheral terminals.

(A) Immunostaining of TrkC (blue), CFP (green), tdTomato (red), and CGRP (white) on thoracic DRG sections from *Ret^{CFP}; PV^{iCre}; R26$^{LSL\text{-}tdTomato}$* mice shows that TrkC$^+$ DRG neurons can be divided into three nearly mutually exclusive populations expressing Ret, PV, and CGRP. These images reveal the presence of TrkC$^+$ and Ret$^+$ (white arrows), TrkC$^+$ and PV$^+$ (asterisks), and TrkC$^+$ and CGRP$^+$ neurons (yellow arrow heads).

(B) Quantification of the percentages of Ret$^+$, PV$^+$, or CGRP$^+$ thoracic DRG neurons among total TrkC$^+$ neurons (1175 neurons from 4 animals) demonstrates that 53.3 ± 1.3% of TrkC$^+$ neurons are Ret$^+$, 35.9 ± 1.7% are PV$^+$, while 18.6 ± 1.5% are CGRP$^+$. Small subsets of TrkC$^+$ neurons express more than one of those molecular markers: 5.9 ± 0.8% are Ret$^+$ and PV$^+$; 3.5 ± 1.2% are Ret$^+$ and CGRP$^+$; 0.3 ± 0.2% are PV$^+$ and CGRP$^+$; while 0.3 ± 0.1% are Ret$^+$, PV$^+$, and CGRP$^+$.

(C-D) Immunostaining of hairy skin sections from *Ret^{CFP}; TrkC^{tdTomato}* mice reveals that Ret$^+$ (green) and TrkC$^+$ (red) neurons innervate 94.7 ± 1.5% of NFH$^+$ circumferential endings (blue) (C) and 100% of Merkel endings (blue) (D) (415 circumferential terminals and 58 Merkel endings from 4 animals).

Scale bar: 50 μm (A, C-D).

Figure 2.5

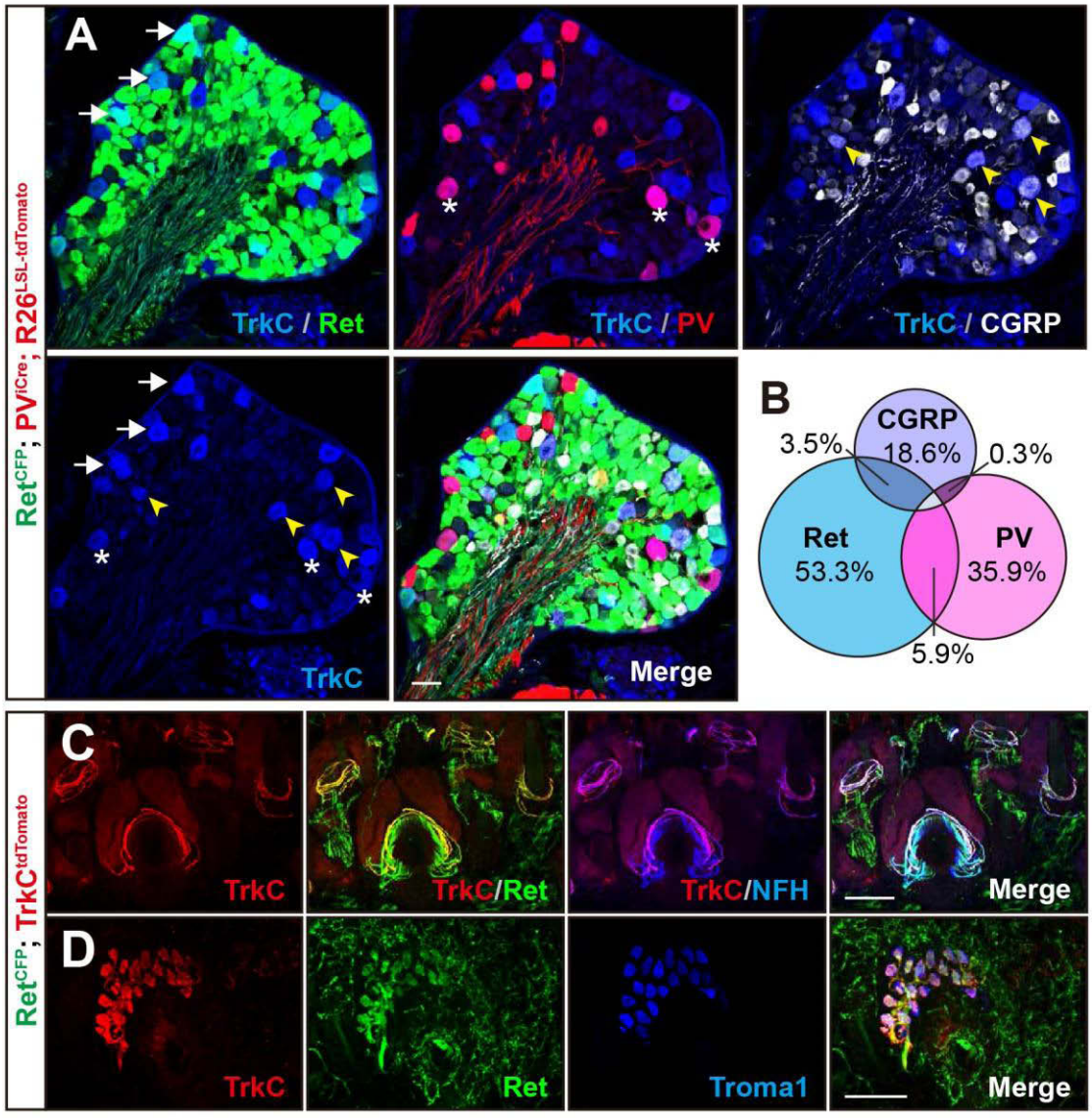
A
TrkC / Ret
TrkC / PV
TrkC / CGRP
TrkC
Merge
Ret^CFP; PV^iCre; R26^LSL-tdTomato
B
CGRP
18.6%
3.5%
0.3%
Ret
53.3%
PV
35.9%
5.9%
C
TrkC
TrkC/Ret
TrkC/NFH
Merge
D
TrkC
Ret
Troma1
Merge
Ret^CFP; TrkC^tdTomato

Figure 2.6 Intersectional genetic labeling strategies for Aβ SA1-LTMRs and neurons with NFH^+ circumferential endings.

(A) Diagram of the TrkC and Ret intersectional genetic labeling strategy.

(B) Quantification of the percentage of sensory endings labeled by CFP in (C) and (D).

(C) Double immunostaining of hairy skin sections from $TrkC^{CreER}$; $Ret^{f(CFP)}$ mice treated with 0.1 tamoxifen at P5 reveals that CFP specifically labels the majority of NFH^+ circumferential endings (79.6 ± 3.3%, 1142 terminals from 4 mice) and all of CFP^+ circumferential endings are NFH^+ (99.2 ± 0.2%, 904 terminals from 4 mice).

(D) Whole-mount immunostaining of hairy skin from $TrkC^{CreER}$; $Ret^{f(CFP)}$ mice treated with 3mg tamoxifen at E12.5 reveals that CFP specifically labels Aβ SA1-LTMRs innervating $Troma1^+$ Merkel cells (40 ± 4%, 78 terminals from 3 mice).

(E-G) Double immunostaining of GFP and TrkC (E), GFP and CGRP (F), GFP and PV (G) of thoracic DRG sections from P21 (E-F) or P10 (G) $TrkC^{CreER}$; $Ret^{f(CFP)}$ mice with postnatal tamoxifen reveals that neurons with NFH^+ circumferential endings labeled by CFP express TrkC (95.6 ± 1.3%) but do not express CGRP (1.7 ± 0.1%) or PV (0%).

(H-J) Double immunostaining of CFP and TrkC (H), CFP and CGRP (I), CFP and PV (J) of thoracic DRG sections from P21 (H-I) or P10 (J) $TrkC^{CreER}$; $Ret^{f(CFP)}$ mice with embryonic tamoxifen reveals that neurons with Merkel endings labeled by CFP express TrkC (98.5 ± 1.5%) but do not express CGRP (0%) or PV (2.2 ± 2.2%).

Scale bar: 50 μm (C, D, E-J).

Figure 2.6

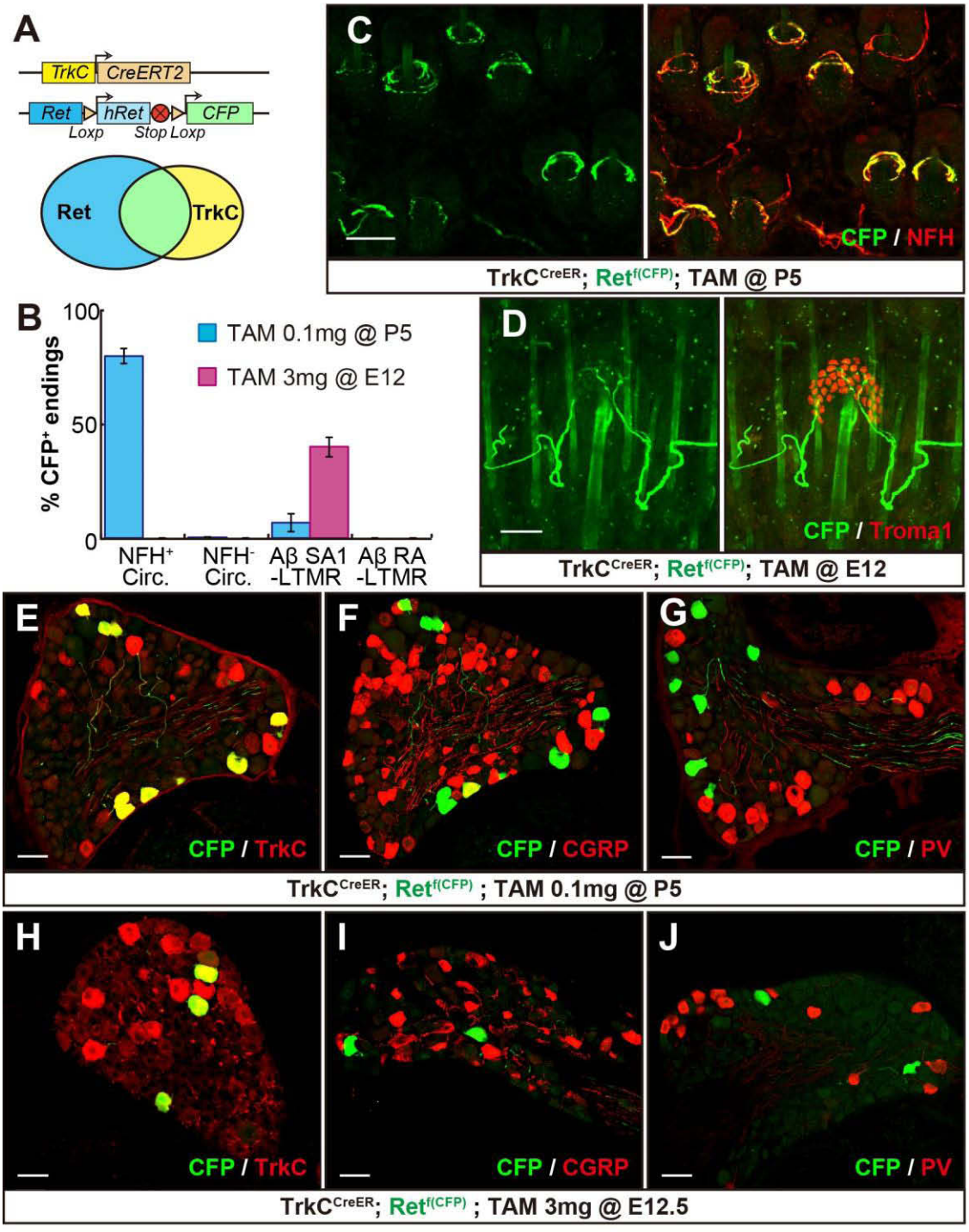
A
TrkC
CreERT2
Ret
hRet
CFP
Loxp
Stop Loxp
Loxp
Ret
TrkC
B
100
50
0
% CFP+ endings
TAM 0.1mg @ P5
TAM 3mg @ E12
NFH+ Circ.
NFH- Circ.
Aβ SA1 -LTMR
Aβ RA -LTMR
C
CFP / NFH
TrkCCreER; Ret f(CFP); TAM @ P5
D
CFP / Troma1
TrkCCreER; Ret f(CFP); TAM @ E12
E
CFP / TrkC
F
CFP / CGRP
G
CFP / PV
TrkCCreER; Ret f(CFP) ; TAM 0.1mg @ P5
H
CFP / TrkC
I
CFP / CGRP
J
CFP / PV
TrkCCreER; Ret f(CFP) ; TAM 3mg @ E12.5

Figure 2.7 NFH$^+$ neurons with circumferential endings are Aβ Field-LTMRs.

(A) The targeted *in vivo* DRG recording preparation.

(B) Representative responses of Aβ SA1-LTMR, Aβ RA-LTMR, and NFH$^+$ circumferential ending neurons to skin stroke delivered by a force controlled brush translated by an ultrasonic piezoelectric stage. The recorded holding force (black, ~5 mN) is shown at top. The stroke speed is 10 mm/sec.

(C) Quantification of stroke-evoked action potential firing rates in Aβ SA1-LTMR (n = 4), Aβ RA-LTMR (n = 5), and NFH$^+$ circumferential neurons (n = 10). Responses were computed as the average of the three highest firing rates observed in a 100 msec window which corresponds to the approximate time required for the brush to transit the full arbor of an Aβ LTMR. NFH$^+$ neurons responded to innocuous stroke with firing rates indistinguishable from those of other hairy skin LTMRs ($p = 0.27$ Welch's t-test).

(D) Conduction velocity measurements reveal that the conduction velocity of NFH$^+$ circumferential ending neurons is indistinguishable from that of other hairy skin Aβ RA and SA1-LTMRs recorded ($p = 0.871$, Welch's t-test).

(E) Von Frey threshold measurements reveal that the force thresholds of NFH$^+$ circumferential ending neurons are higher than those of other Aβ subtypes (90% bootstrap CI [21.2, 52.3] fold higher).

(F) Temporal patterns of responses to indentation. Representative peristimulus time histograms (PSTHs) show that NFH$^+$ circumferential neurons adapt more rapidly than Aβ SA1-LTMRs but lack the pronounced off-step responses of the Aβ RA-LTMRs. The indentation force recording (top) is aligned to the PSTH showing the mean firing rate computed across 15 stimulus presentations (7 msec bin widths).

(G) Representative spiking responses of NFH^+ circumferential ending neurons and Aβ RA-LTMR to deflection of guard hairs.

(H) Group data showing that all Aβ RA-LTMRs respond similarly to deflection of guard hairs and skin stroke ($p = 0.85$, paired t-test), while NFH^+ circumferential ending neurons are insensitive to guard hair deflection ($p = 0.017$, paired t-test). As in (C), evoked firing rates are computed over a 100 msec window.

Figure 2.7

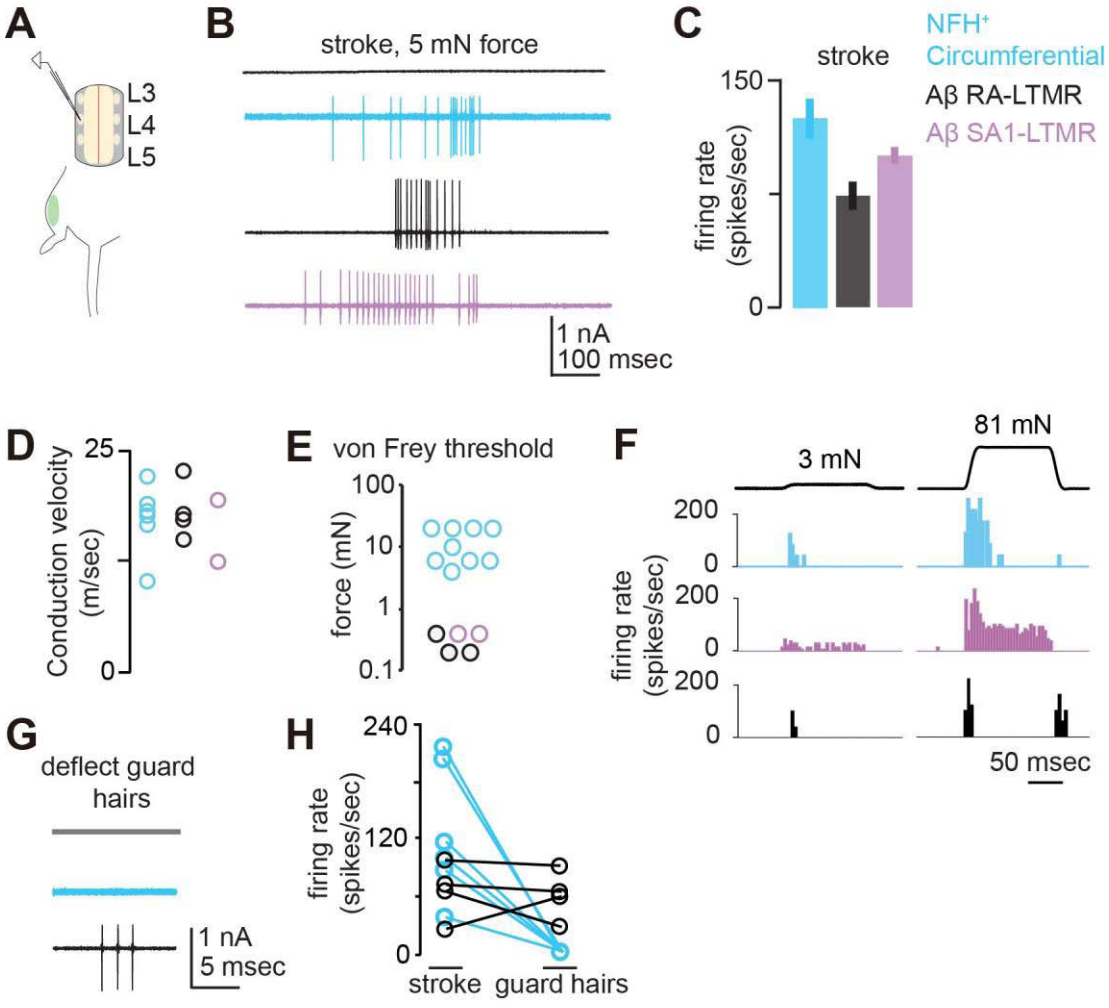
A
L3
L4
L5
B
stroke, 5 mN force
1 nA
100 msec
C
stroke
150
0
firing rate (spikes/sec)
NFH+
Circumferential
Aβ RA-LTMR
Aβ SA1-LTMR
D
25
0
Conduction velocity (m/sec)
E
von Frey threshold
100
10
1
0.1
force (mN)
F
3 mN
81 mN
200
0
firing rate (spikes/sec)
50 msec
G
deflect guard hairs
1 nA
5 msec
H
240
120
0
firing rate (spikes/sec)
stroke
guard hairs

Figure 2.8 ***Ex vivo*** **intracellular recordings of Aβ Field-LTMRs.**

(A) *Ex vivo* intracellular recordings reveal a suite of nociceptor properties recorded at 31 ± 1 ºC, including large amplitude inflected somal action potentials (black trace) that are significantly broader than the uninflected somal spikes of Npy2r-GFP^{+} Aβ RA-LTMRs (grey trace); inflection on the falling phase is revealed (arrow) in the lower spike derivative trace.

(B) Manual tugs on innervated hairs evoke vigorous bursts. Peak firing rate illustrated (including electrotonic potentials in the initial segment, arrows) is >550 Hz, which presumably exceeds the limiting rate at which the cell is capable of supporting somal action potentials.

(C) Controlled indentation of a hotspot with increasing forces applied using a 1 mm diameter blunt probe. The duration of applied forces was 5 sec. Raster plots of firing rates display only responses in the range of 0 - 50Hz to emphasize the sustained component (top), while the peak firing rates that occurred at the onset are indicated in parentheses.

(D) Same hotspot as in (C) but with controlled indentations applied through a sharp probe, revealing a leftward shift in sensitivity. (E) Same hotspot as in C and D but with controlled traction applied to an innervated hair. Note the vigor of the response to 1 mN relative to C and D.

Figure 2.8

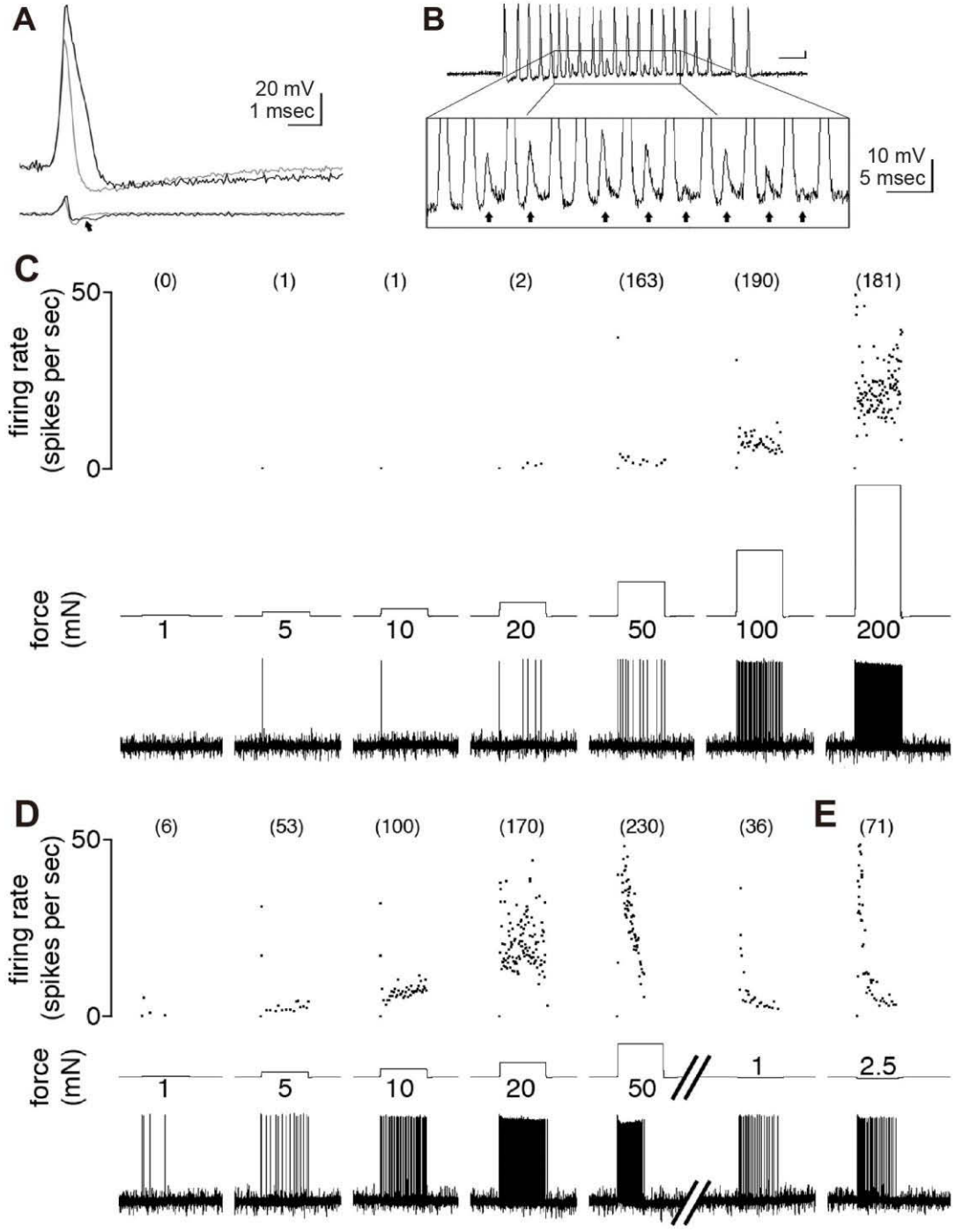
A
20 mV
1 msec
B
10 mV
5 msec
C
(0)
(1)
(1)
(2)
(163)
(190)
(181)
50
0
firing rate
(spikes per sec)
force
(mN)
1
5
10
20
50
100
200
D
(6)
(53)
(100)
(170)
(230)
(36)
E
(71)
50
0
firing rate
(spikes per sec)
force
(mN)
1
5
10
20
50
1
2.5

Chapter 3. The ultrastructure of hair follicle terminals underlying the sensitivity to stimuli across hair or skin

3.1. Aβ Field-LTMRs associate with hair follicles and yet they are insensitive to hair deflection

Our findings indicate that Aβ Field-LTMRs are insensitive to deflection of guard hairs even though they associate with all hair follicle types. Other studies have suggested that Aβ Field-LTMRs may respond to deflection of multiple hairs spanning a large stimulus "field", which may be explained by either simultaneous deflection of many hairs or the inevitable stimulation of skin that occurs when stroking a large group of hairs (Horch et al., 1977). To further investigate potential responses of Aβ Field-LTMRs following deflection of many hairs simultaneously, we developed an air puff stimulus that deflects groups of hairs, without simultaneous skin displacement. Using a Laser Doppler Vibrometer, we measured the extent of skin and hair displacement orthogonal to the skin and found that air puff stimuli could be titrated to elicit varying amounts of hair deflection with little to no skin displacement (Figure 3.1A). For comparison, indentation with a servo-actuated von Frey filament (20 mN) produced displacement of both hairs and skin (Figure 3.1A). Average power spectrums for multiple skin and hair displacement measurements show that air puff is a more potent stimulus for hair deflection than skin movement across a wide range of stimulus intensities (Figure 3.1B). Thus, air puff is primarily a hair deflection stimulus that can be readily controlled and titrated.

Next, we measured the response properties of Aβ Field-LTMRs to air puff-induced hair deflection in comparison to Aβ RA-LTMRs and Aβ SA1-LTMRs using *in vivo* cell-attached recordings as described in Figure 2.7. As expected, both air puff and skin stroking elicited robust spiking in Aβ RA-LTMRs (Figure 3.1C-D). Moreover, Aβ RA-LTMR spike frequency increased monotonically with increases in the speed of the air puff, and this response reached a plateau at an

air puff speed of 30 m/sec (Figure 3.1D). Remarkably, the response of Aβ RA-LTMRs to air puff was entirely dependent on the presence of hairs; experiments in which hairs were removed during the recording period showed that the response to air puff, but not to skin stroking, was abolished following hair removal (Figure 3.1C-D), further confirming that air puff elicits hair deflection with minimal skin indentation. In contrast, Aβ Field-LTMRs and Aβ SA1-LTMRs did not respond to air puff across a wide range of intensities, including those that saturate the Aβ RA-LTMRs (Figure 3.1C-D), although stroking of the same area of skin elicits a robust response in both of these LTMR subtypes (Figure 3.1C). Moreover, Aβ Field-LTMR responses to gentle stroking of the skin were similar before and after removing hairs (Figure 3.1C), indicating that stroking the skin does not rely on deflecting hair shafts to activate these neurons. Thus, while Aβ Field-LTMRs associate with hair follicles, they are categorically insensitive to hair deflection. Moreover, Aβ Field-LTMRs, Aβ RA-LTMRs and Aβ SA1-LTMRs have distinct response properties to mechanical stimulation of mouse hairy skin; while all three Aβ-LTMR subtypes respond to gentle stroking the skin, Aβ RA-LTMRs and Aβ SA1-LTMRs but not Aβ Field-LTMRs respond to gentle skin indentation, and only Aβ RA-LTMRs respond to hair deflection.

3.2. Micromechanical determinants of Aβ-LTMR sensitivity

Aβ Field-LTMRs and Aβ RA-LTMRs both form intimate contacts with hair follicles and yet they prefer different mechanical stimuli. We hypothesized that the ultrastructural architecture of their cutaneous endings, their ending positions relative to hair follicles, and the mechanics of the surrounding tissues may explain their markedly different sensitivities to hair deflection and skin indentation observed in our physiological recordings. We first performed transmission electron microscopy using ultrathin transverse sections of hair follicles to define the ultrastructural features of Aβ RA-LTMR and Aβ Field-LTMR terminals and their relationship to hair follicle epithelial cells. Interestingly, a cross sectional analysis of individual hair follicles clearly shows

that while both longitudinal lanceolate (Aβ RA-LTMR) and circumferential (Aβ Field-LTMR) endings are associated with hair follicles, they reside within distinct layers surrounding follicles. Aβ RA-LTMR longitudinal lanceolate endings are located within an inner region where they closely abut the basement membrane of hair follicle epithelia cells (Figure 3.2A and 3.2C, average distance between hair follicle epithelial cell and axonal membrane ~100 nm), as previously described (Li and Ginty, 2014). In contrast, Aβ Field-LTMR circumferential endings reside within an outer region of the follicle, surrounding the longitudinal lanceolate endings, and are thus considerably more distant from the follicle (Figure 3.2A and 3.2B; average distance 4 μm). Both ending types are associated with terminal Schwann cells, which are readily identified by the numerous pinocytotic vesicles on their membrane as well as their endoplasmic reticulum structure. Strikingly, both types of sensory endings are aligned with collagen fibers that are organized in parallel to the orientation of the axon terminals (Figure 3.2A-C). Indeed, a dense network of collagen fibers that are longitudinally oriented with respect to the hair follicle is observed in the extracellular space surrounding Aβ RA-LTMR longitudinal lanceolate endings while, conversely, Aβ Field-LTMR circumferential endings are embedded within a distinct network of circumferentially oriented collagen fibers in the outer region of the follicle.

The distinct ultrastructural features of longitudinal lanceolate and circumferential endings, their close or distant relationship with hair follicle epithelial cells, and their respective alignments within either longitudinally or circumferentially organized collagen networks around hair follicles, are strongly suggestive of an ultrastructural basis for the unique physiological tuning properties of Aβ RA-LTMRs and Aβ Field-LTMRs. We addressed this using a finite element model (FEM) of skin mechanics to estimate the extent to which hairy skin mechanical stimulation is transformed into strain acting upon longitudinal lanceolate endings and circumferential endings. The mechanical properties of the skin, hair, hair follicle and the two layers of collagen networks were estimated and considered in this model (see Experimental Procedures). For this analysis, we

simulated activation of axon terminals by delivering three stimuli: a 100 μm hair deflection stimulus applied 420 μm from the base of the hair, and 0.8 mN or 10 mN indentation stimuli in a 0.1 mm or 0.25 mm diameter area, respectively, applied to a skin region adjacent to the hair follicle (Figure 3.3A-C, bottom). These mimic the stimuli used for the electrophysiological analyses shown in Figures 2.7 and 3.1. Results of FEM simulations suggest that more strain acts upon longitudinal lanceolate endings than on circumferential endings in response to both hair deflection and skin indentation (Figure 3.1A-E). The maximum strain on lanceolate endings in response to 100 μm hair deflection or 0.8 mN skin indentation is comparable (~$2e^{-3}$), and is much higher than that acting on circumferential endings (~$5e^{-4}$) (Figure 3.1A-B and 3.1D-E). Simulations using 10 mN skin indentation, which is close to the von Frey threshold of Aβ Field-LTMRs, predicted the maximum strain acting on circumferential endings to be ~$6e^{-3}$ (Figure 3.1C), which is greater than their response to 100 μm hair deflection (18 fold) and 0.8 mN skin indentation (12 fold) and is slightly higher than the strain on lanceolate endings in response to 100 μm hair deflection and 0.8 mN skin indentation (3 fold). These simulated strain values acting on the two types of terminals are consistent with our physiological measurements of the relative sensitivities of the two neuronal types. We next modified the FEM to perform the same types of simulations in the absence of the two layers of collagen, which were observed by transmission electron microscopy. These simulations predicted that similar amounts of strain act on the longitudinal lanceolate endings in the presence or absence of the two layers of collagen. On the other hand, the strain acting on circumferential endings in response to indentation in the absence of two distinct collagen layers was estimated to be approximately 50 times greater than that when both collagen layers are present (Figure 3.1F). Taken together, these FEM simulations suggest that the strain acting on Aβ RA-LTMR longitudinal lanceolate endings is greater than the strain acting on the Aβ Field-LTMR circumferential endings following both hair deflection and skin

indentation, and that the outer collagen layer may serve to dampen responses of Aβ Field-LTMR circumferential endings to skin indentation.

Figure 3.1 Aβ Field-LTMRs are insensitive to hair deflection yet sensitive to direct stimulation of skin.

(A) Laser Doppler vibrometric measurements of skin and hair movement in response to air puff (left, 15m/sec at the source) and indentation (right, 2g von Frey filament). Shown are representative displacements of the base of a hair shaft and a nearby patch of skin.

(B) Group data showing the power spectral density averaged across stimulus presentations and measurement locations (n = 5 hairs, n = 5 skin locations). For air puff, the motion recorded at the base of hairs exceeds that of the surrounding skin by three orders of magnitude.

(C) Representative *in vivo* recordings of Aβ Field-LTMR (blue) and Aβ RA-LTMR (black) responses to air puff and stroke, before and after hair removal. The recording was maintained continuously in all cases.

(D) Air puff evoked spiking responses from Aβ Field-LTMRs (n = 6), Aβ SA1-LTMR (n = 3), Aβ RA-LTMRs (n = 4) and Aβ RA-LTMR after hair removal (n = 4). Firing rates computed over the entire 100 msec air puff are plotted against the speed of the air at the stimulator nozzle, which was placed 12mm above the skin. All Aβ RA-LTMR retained sensitivity to stroke after hair removal (C, data not shown), demonstrating that they remained mechanically sensitive despite loss of air puff responses. Traces are offset for clarity.

Figure 3.1

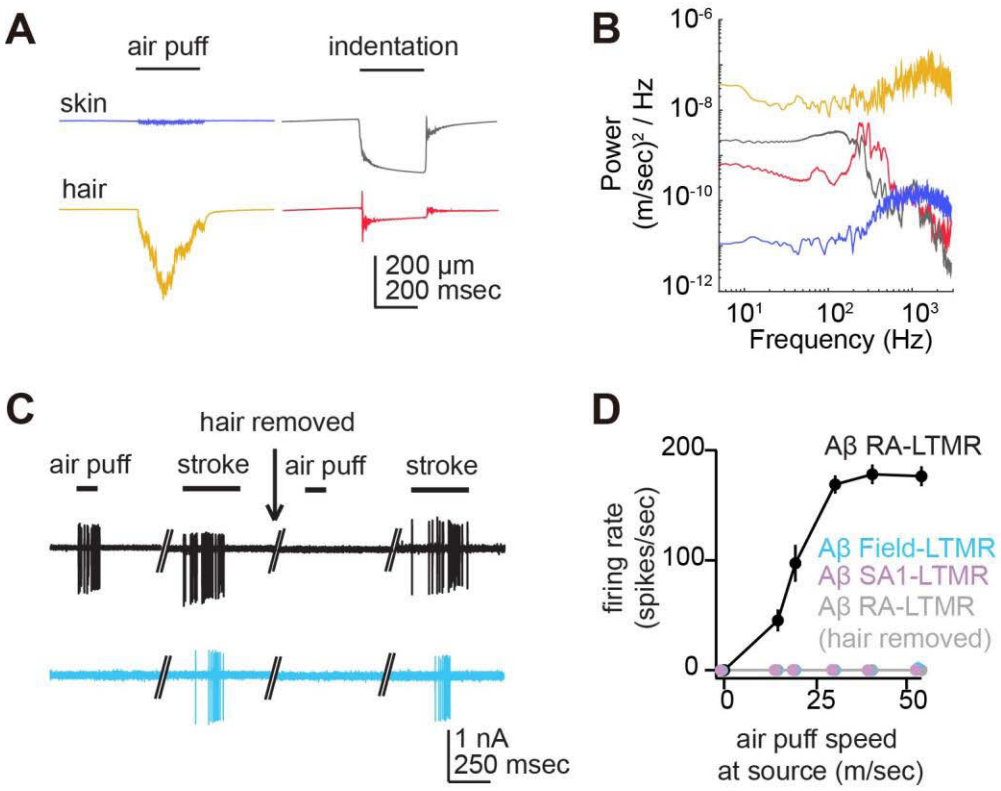
A
air puff
indentation
skin
hair
200 µm
200 msec
B
Power
(m/sec)² / Hz
10-6
10-8
10-10
10-12
10¹
10²
10³
Frequency (Hz)
C
hair removed
air puff
stroke
air puff
stroke
1 nA
250 msec
D
Aβ RA-LTMR
Aβ Field-LTMR
Aβ SA1-LTMR
Aβ RA-LTMR
(hair removed)
firing rate
(spikes/sec)
200
100
0
0
25
50
air puff speed
at source (m/sec)

Figure 3.2 The ultrastructure of lanceolate and circumferential endings.

(A-C) TEM images of cross-sections through a lanceolate and circumferential ending complex at a hair follicle. (B-C) Magnified view of the region in the red box of (A). The lanceolate ending (white asterisks) and terminal Schwann cell complexes are embedded in longitudinal oriented collagen fibers (L.C. with arrows) in close proximity to hair follicle epithelial cells. Circumferential endings (arrow heads) are embedded in circumferentially oriented collagen fibers (C.C.) in the outer layer. The lanceolate endings, circumferential endings, terminal Schwann cells, and hair follicle epithelia cells are pseudo colored in green, blue, and pink, and yellow, respectively.

Scale bar: 1 μm (A-C).

Figure 3.2

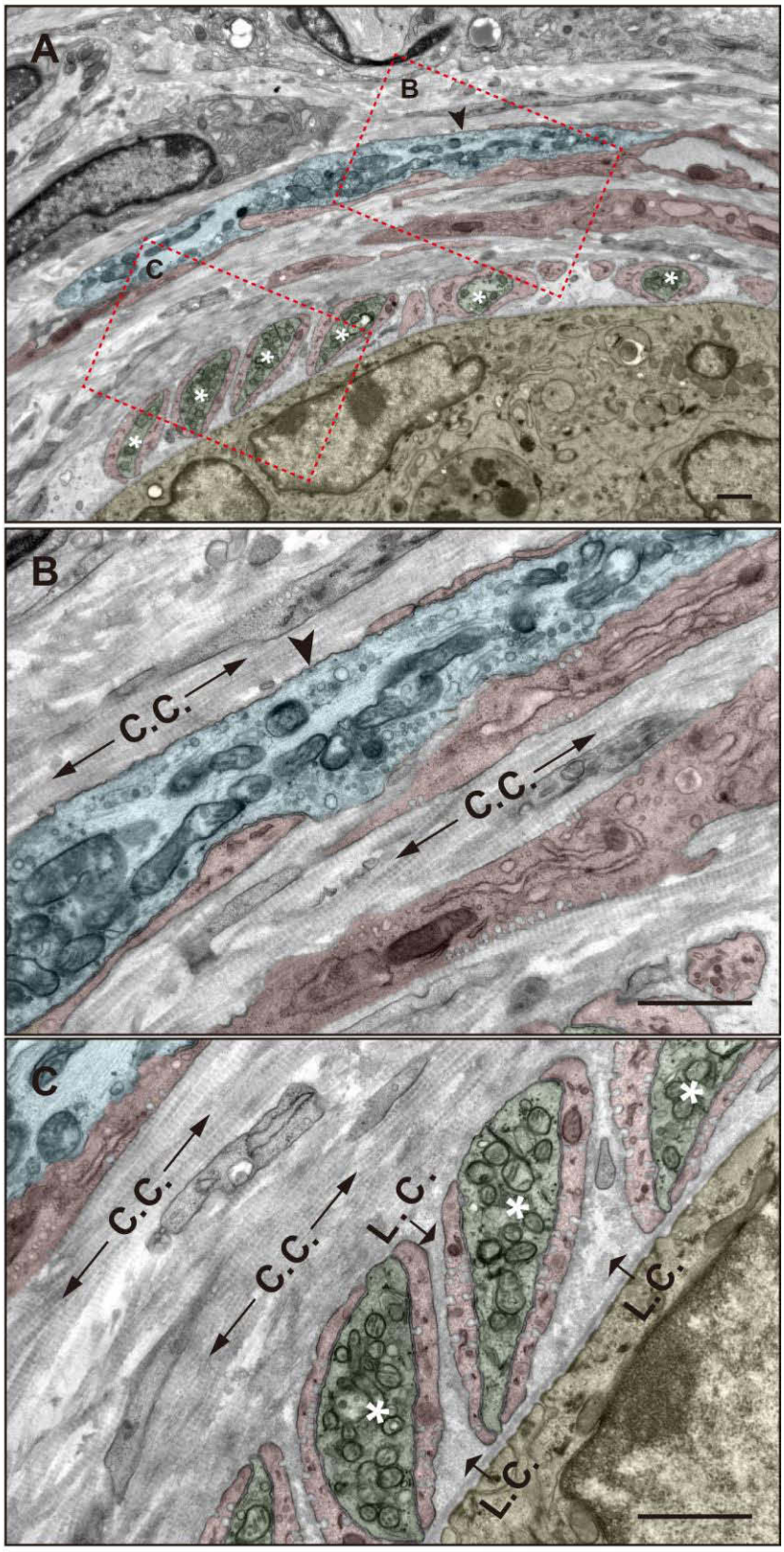

Figure 3.3 Finite Element Modeling reveals that the ultrastructure supports the unique tuning properties of Aβ RA-LTMRs and Aβ Field-LTMRs.

(A-F) Finite element modeling (FEM) simulations of the strain acting on lanceolate or circumferential endings in response to mechanical stimuli.

(A-B) Top: Contour plots of strain distribution along the lanceolate and circumferential endings in response to 100 μm hair deflection (A), 0.8 mN skin indentation (B), and 10 mN skin indentation (C). Bottom: schematic diagram of the stimulations.

(D-E) Plot of the average strain along different positions of lanceolate or circumferential terminals. The zero location is marked by the red asterisk in (A).

(F) The ratio of accumulated strain in the absence and the presence of collagen layers along lanceolate or circumferential endings under either 100 μm hair deflections or 0.8mN skin indentations.

Figure 3.3

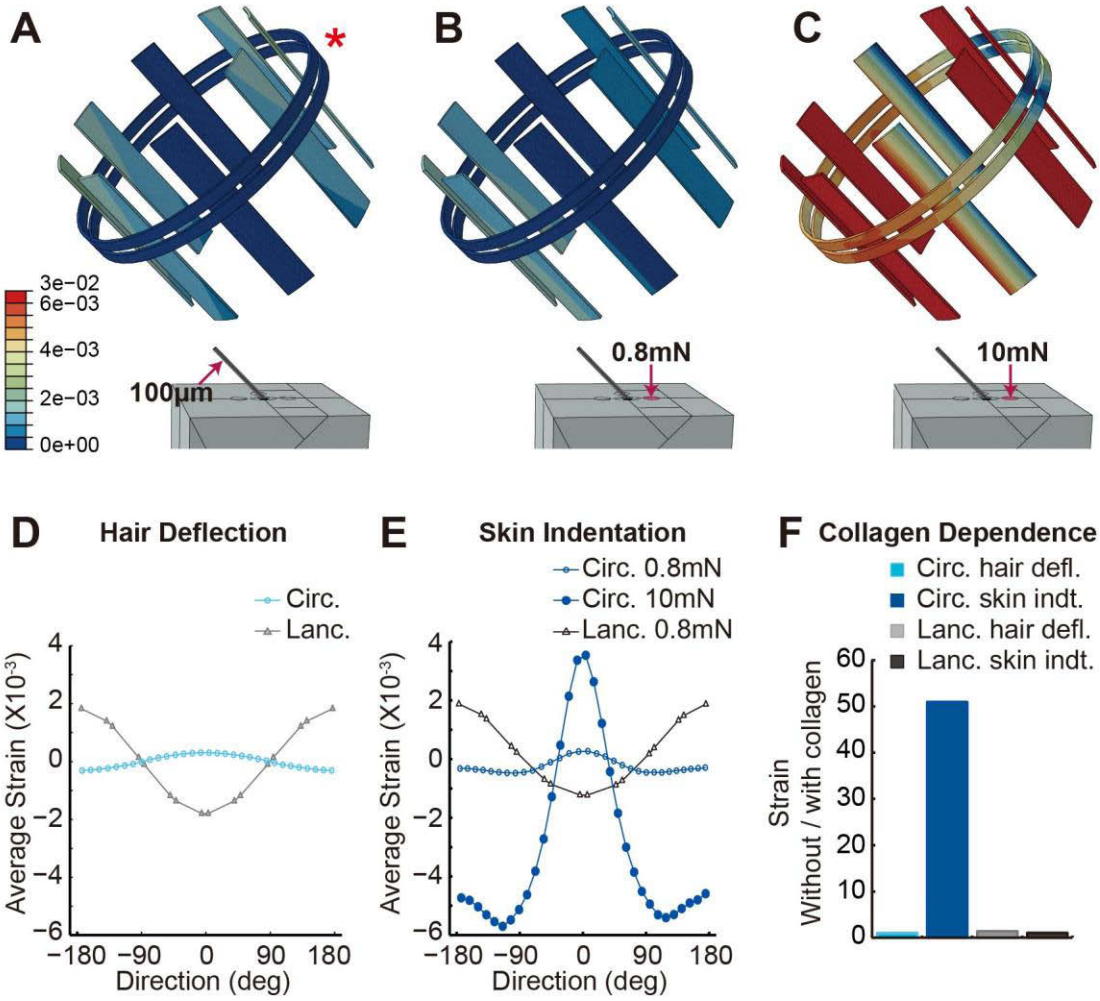
A
B
C
*
3e−02
6e−03
4e−03
2e−03
0e+00
100μm
0.8mN
10mN
D
Hair Deflection
Circ.
Lanc.
Average Strain (X10-3)
Direction (deg)
E
Skin Indentation
Circ. 0.8mN
Circ. 10mN
Lanc. 0.8mN
Average Strain (X10-3)
Direction (deg)
F
Collagen Dependence
Circ. hair defl.
Circ. skin indt.
Lanc. hair defl.
Lanc. skin indt.
Strain
Without / with collagen

Chapter 4. Aβ Field-LTMRs integrate tactile stimuli across large receptive fields enabling responsiveness to gentle stroking of the skin

Aβ Field-LTMRs respond to gentle stroking of skin, yet they are relatively insensitive to focal indentation and encode skin indentation in the noxious range. How do Aβ Field-LTMRs acquire sensitivity to gentle stroking across large areas of skin? One potential mechanism is that the sensory arbors of Aβ Field-LTMRs span large areas of skin, such that focal stimuli activate only a small fraction of endings that are weakly mechanosensitive, whereas stimuli that sweep across the entirety of an Aβ Field-LTMR's endings generates multiple receptor potentials that sum throughout the arbor and induce greater responses. Thus, we explored the idea that many weakly mechanosensitive endings of individual Aβ Field-LTMRs are elaborated over a large area of skin.

We first produced fine scale receptive field maps of Aβ Field-LTMRs using *in vivo* physiological recordings. Stimuli were delivered using a sharp-tipped (20 μm in diameter) force controlled indenter, which was systematically translated over the skin of the dorsal thigh at 50 μm intervals by an ultrasonic piezoelectric stage. This distance was chosen to match the spatial scale of hair follicles and the spacing between them (Figure 4.3B-C). The resulting spatial receptive field maps are composed of the spiking responses to indentations delivered to 3200 separate positions.

Strikingly, Aβ Field-LTMR responses to 27 mN step indentations showed that the punctuate "hotspots", described above in both *in vivo* and *ex vivo* recordings, are distributed over 3-4 mm^2 of the skin. Responses to stimulation of hotspots (half-width ~ 60 μm, n = 2 with full receptive fields) exceeded 100 Hz, and hotspots were separated by insensitive stretches where skin stimulation evoked 0-2 spikes (Figure 4.1A and 4.1C). In dramatic contrast, Aβ SA1-LTMRs exhibited a focal receptive field hotspot that was considerably larger than individual Aβ Field-LTMR hotspots, even when mapped using a much weaker force applied to the skin (Figure 4.1B

and 4.1D). In addition, while the Aβ Field-LTMR did not respond to 1 mN step-indentations, the Aβ SA1-LTMR responded with low firing frequency, which is consistent with the finding that Aβ Field-LTMRs have a much higher mechanical threshold to focal indentation stimuli compared to other Aβ-LTMR subtypes (Figure 2.7D and 2.8C). Taken together, individual Aβ Field-LTMRs exhibit unusually large receptive fields composed of weakly mechanosensitive "hotspots" distributed over a 3-4 mm^2 area of skin. The spatial scale of individual hotspots suggests that they span an area equivalent to one or a few hair follicles.

The newly generated *TrkC*^{CreER} mouse lines allow us to explore with single-cell resolution the cutaneous anatomy of Aβ Field-LTMRs that underlies their physiological receptive field properties. To achieve this, we titrated the dosage of tamoxifen (0.01 mg at P8) administered to *TrkC*^{CreER}*; Brn3a*$^{f(AP)}$ mice such that Cre-mediated recombination and AP expression occurred in only 10-50 Aβ Field-LTMRs or Aβ SA1-LTMRs per animal. This analysis revealed that individual Aβ SA1-LTMRs typically innervate only one or two touch domes (74% or 26%, respectively) associated with guard hair follicles (Figure 4.1F), consistent with physiological receptive fields measurements (Lesniak et al., 2014; Woodbury and Koerber, 2007; Wu et al., 2012) (Figure 4.1D). In dramatic contrast, individual Aβ Field-LTMR axons branch in the skin to give rise to circumferential endings associated with a remarkably large number of hair follicles (84 ± 4, Figure 4.1E, 4.3D and 4.3F). Despite a large range in the number of associated hair follicle endings (20-180 hair follicles per neuron), most Aβ Field-LTMRs innervate a large area of skin (3.1 ± 0.1 mm^2, Figure 4.1E, 4.3E and 4.3G). Importantly, these Aβ Field-LTMR morphological receptive fields bear striking resemblance to those measured electrophysiologically (Figure 4.1C), suggesting that individual or small groups of circumferential endings are the fundamental mechanosensitive units of Aβ Field-LTMRs.

How unique is the anatomy of the Aβ Field-LTMR? To address this, we next compared the morphological receptive fields of Aβ Field-LTMRs to all other hairy skin LTMRs, including Aβ SA1-LTMRs, Aβ RA-LTMRs, Aδ-LTMRs and C-LTMRs, using sparse genetic labeling strategies specific for each LTMR subtype (Figure 4.2A-E). Aβ RA-LTMRs, Aδ-LTMRs and C-LTMRs were labeled in Ret^{CreER}, $TrkB^{CreER}$ or TH^{iCreER} mice (Li et al., 2011; Luo et al., 2009; Rutlin et al., 2014), respectively, crossed with $Brn3a^{f(AP)}$, and treated with a low dose of tamoxifen. This comparative LTMR analysis revealed a striking dissimilarity of Aβ Field-LTMR receptive fields relative to all other hairy skin LTMRs. Indeed, Aβ RA-LTMRs (Figure 4.2B) associate with many fewer hair follicles (15.2 ± 0.9, Figure 4.3A, D, and F) and most of these neurons innervate a small skin area (1.6 ± 0.1 mm^2, Figure 4.3A, E, and G) compared to Aβ Field-LTMRs (Figure 4.2A and 4.3A). Interestingly, a small subset of Aβ RA-LTMRs does innervate skin areas comparable to the Aβ Field-LTMRs, suggesting the existence of two Aβ RA-LTMR subtypes (Figure 4.3G). The remaining hairy skin LTMRs have both smaller receptive fields and innervate fewer hair follicles, compared to Aβ Field-LTMRs: individual Aδ-LTMRs and C-LTMRs innervate 43 ± 2 and 22 ± 1 hair follicles arranged within relatively small areas of the skin, 0.51 ± 0.03 mm^2 and 0.30 ± 0.02 mm^2 , respectively (Figure 4.2D-E, 4.3A, and 4.3D-G). Thus, Aβ Field-LTMRs have unusually expansive receptive fields containing the largest number of specialized mechanosensory terminals of any known mammalian LTMR type, consistent with their selective sensitivity to stimuli acting across a large area of the skin.

Given the Aβ Field-LTMR's high sensitivity to gentle skin stroke, we next asked whether the expansive terminal fields of Aβ Field-LTMRs exhibit morphological features consistent with subthreshold integration across circumferential endings. For Aβ RA2-LTMRs, which associate with Pacinian corpuscles within the dermis or deep tissues, spike initiation occurs in an axonal segment that is immediately adjacent to the corpuscle (Loewenstein, 1969). Similarly, the Aβ SA1-LTMR spike initiation site (SIS), measured using morphological criteria, is thought to reside

within close proximity to Merkel cells (Lesniak et al., 2014). We therefore determined the length of unmyelinated axon segments spanning between an Aβ Field-LTMR's SISs and its circumferential terminals, and the findings were compared to those of Aβ SA1-LTMRs and Aβ RA-LTMRs. SISs were visualized using myelin basic protein (MBP) in combination of βIV-Spectrin immunostaining to localize ion channel scaffold complexes at the first heminode and sites of myelination initiation (Yang et al., 2007). Thus, the average distance between sensory terminals and the SIS was calculated for individual Aβ-LTMRs that are either genetically labeled (Aβ RA-LTMRs or Aβ Field-LTMRs) or immuno-labeled (Aβ SA1-LTMRs). Our analysis showed that SISs and initial myelination segments are uniformly localized within very close proximity to the sensory terminals of both Aβ SA1-LTMRs (18.8 ± 0.7 μm; Figure 4.4B and 4.4D) and Aβ RA-LTMRs (6.0 ± 1.7 μm; Figure 4.4A and 4.4D). In stark contrast, Aβ Field-LTMR SISs are found at variable distances (123 ± 49 μm; Figure 4.4C and 4.4D) from their circumferential terminals and thus their unmyelinated axon segments are significantly longer than those of Aβ SA1-LTMRs and Aβ RA-LTMRs (Figure 4.4D and 4.5A-C). In some cases, Aβ Field-LTMR SISs were located too far from the hair follicle to identify (Figure 4.5C, data not shown). Similar findings were obtained in experiments in which the three types of Aβ-LTMRs were immuno-labeled using NFH and the Merkel cell marker Troma1 (data not shown). Together, these findings indicate that a distinguishing feature of Aβ Field-LTMRs among hairy skin Aβ-LTMR subtypes is that their initial sites of myelination and SISs are often localized far from the circumferential endings around hair follicles. Thus, Aβ Field-LTMRs have large, spotty receptive fields containing many weakly mechanosensitive circumferential endings distributed across a large area of skin and SISs located at variable, often considerable distances from the hair follicles with which they associate. We propose that these unique physiological and morphological properties underlie the sensitivity of Aβ Field-LTMRs to gentle stroking across large fields of skin.

Figure 4.1 Aβ Field-LTMRs have large receptive fields comprising many weak mechanosensitive endings.

(A-B) *In vivo* loose patch electrophysiological recordings from an Aβ Field-LTMR (A) or Aβ SA-LTMR (B) in response to 1 mN (left) and 27 mN (right) spatially patterned skin indentations with a 20 μm tipped tungsten probe. The indenter moved across the skin in 50 μm steps, with adjacent steps corresponding to adjacent rows in the raster.

(C) Receptive field of an Aβ Field-LTMR mapped with a 27 mN indentation. Grid indentations of Aβ Field-LTMRs reveal punctuated "hotspots" that extend for 50-100 μm and are separated by insensitive patches (n = 3).

(D) Receptive field of an Aβ SA1-LTMR neuron mapped with a 1 mN indentations (note the lower force) reveal a single punctate focus.

(E-F) Whole-mount AP staining of hairy skin reveals peripheral terminals from individual Aβ Field-LTMRs or Aβ SA1-LTMRs (see experimental procedures for details).

Scale bar: 500 μm (C-F).

Figure 4.1

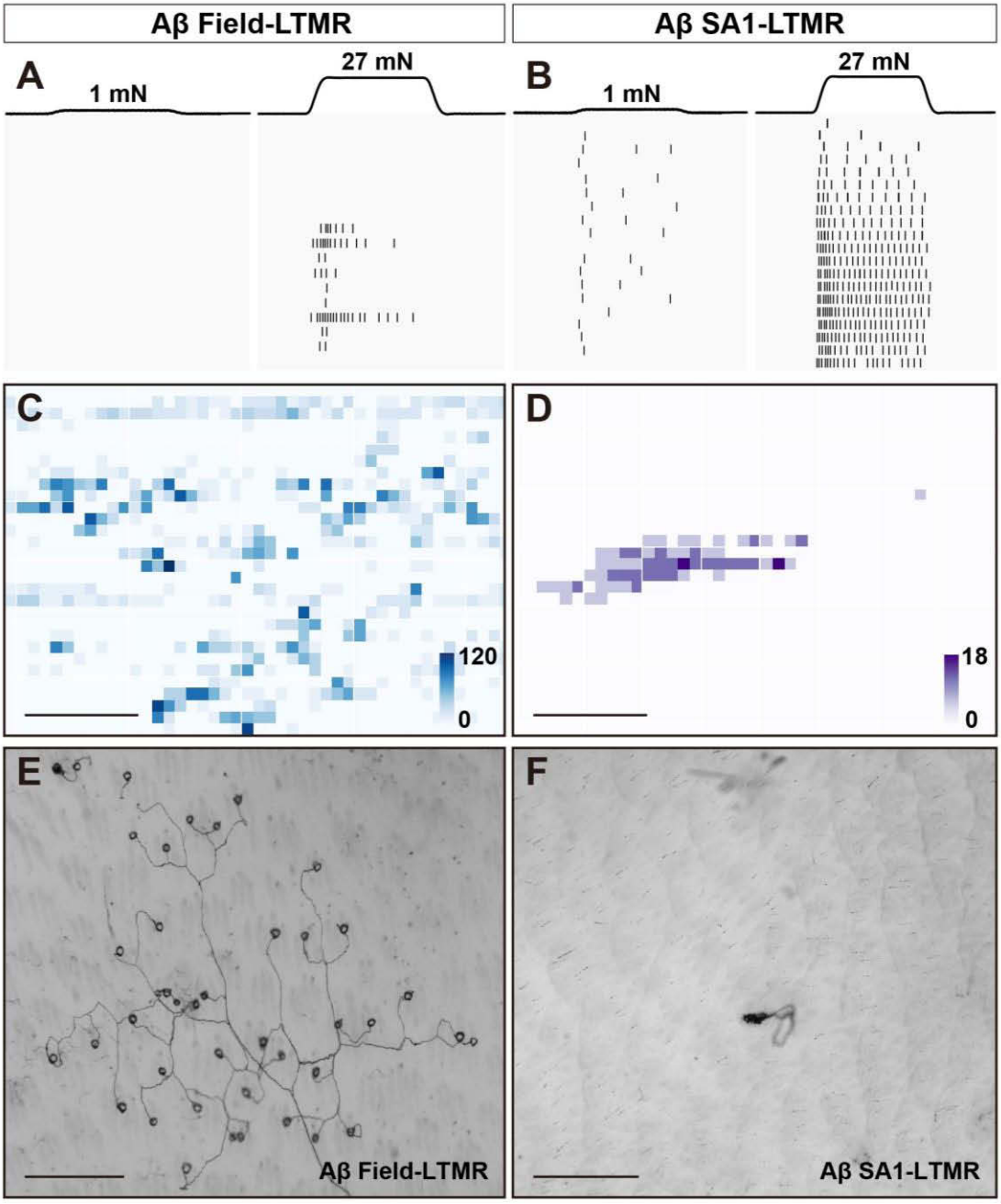
Aβ Field-LTMR
Aβ SA1-LTMR
A
1 mN
27 mN
B
1 mN
27 mN
C
120
0
D
18
0
E
Aβ Field-LTMR
F
Aβ SA1-LTMR

Figure 4.2 Comparison of the anatomical receptive field of Aβ Field-LTMRs and other LTMR subtypes.

(A-E) Whole-mount AP staining of hairy skin reveals peripheral terminals from Aβ Field-LTMRs (A), Aβ RA-LTMRs (B), Aβ SA1-LTMRs (C), Aδ-LTMRs (D), and C-LTMRs (E) sparsely labeled by a *Brn3a*$^{f(AP)}$ reporter line (see experimental procedures for details).

Scale bar: 500 μm (A-E).

Figure 4.2

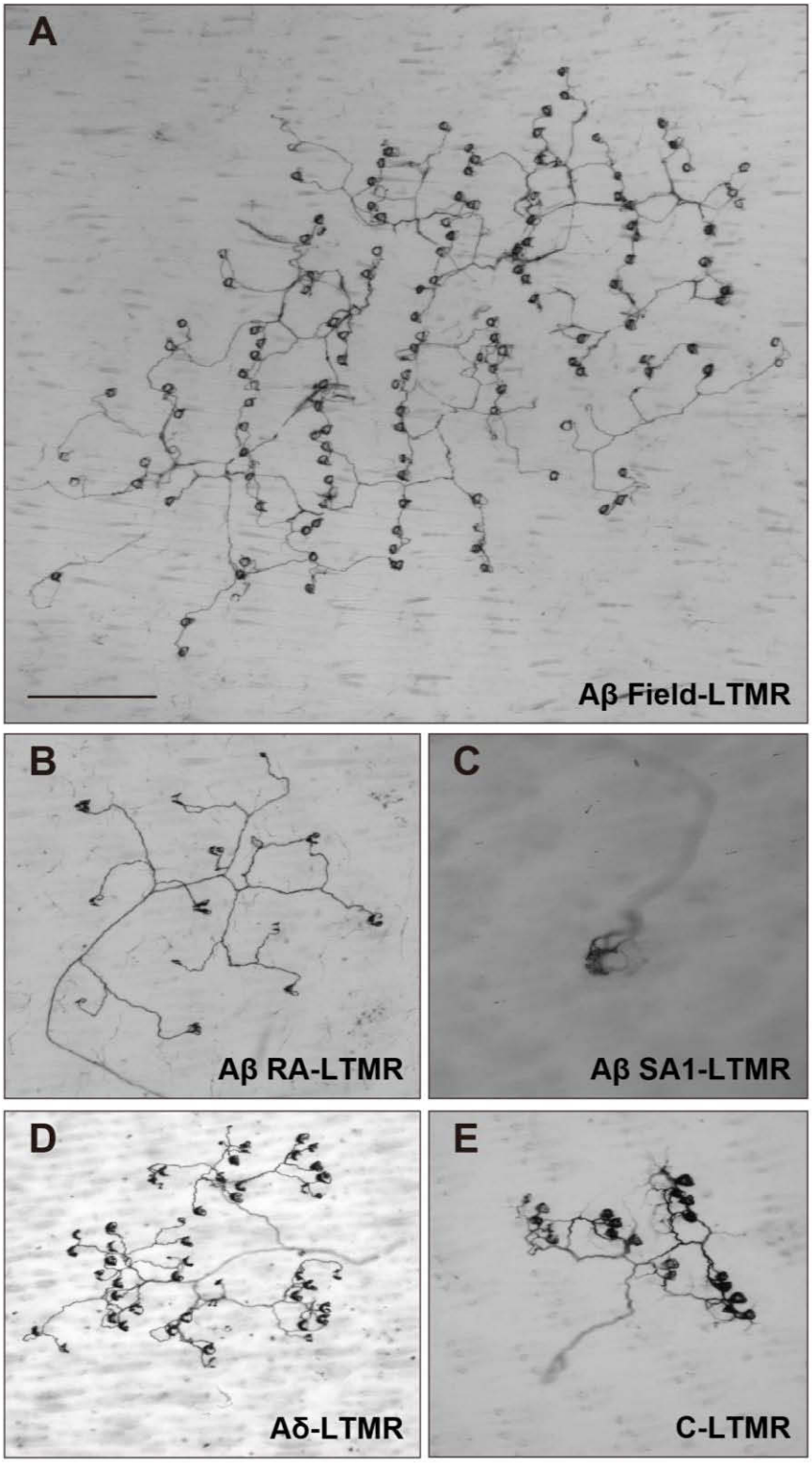

Figure 4.3 Distribution of hair follicle receptors and morphological receptive fields for LTMR subtypes.

(A-B) Quantification of the diameter of hair follicle receptors (A) and the minimum distance between hair follicle receptors (B) was performed after whole-mount immunostaining of CGRP and NFH on the back hairy skin of P21 mice. The diameter of hair follicle receptors is 31.9 ± 0.5 μm (300 terminals in n = 3 animals) and the spacing between them is 39.0 ± 1.3 μm (119 terminals in n = 3 animals).

(C-G) Quantification of the innervated hair follicle numbers (C, D and F) as well as receptive field area (C, E, and G) of LTMR subtypes after whole-mount AP staining of hairy skin using mouse lines described in Figure 6 and 7 (see extended experimental procedures for details). Each dot represents a single neuron in (C). Aβ Field-LTMRs (n = 125 neurons in 8 animals), Aβ RA-LTMRs (n = 127 neurons in 10 animals), Aδ-LTMRs (n = 55 neurons in 4 animals), and C-LTMRs (n = 41 neurons in 3 animals) innervate 84 ± 4, 15.2 ± 0.9, 43 ± 2, and 22 ± 1 hair follicles and cover an area of 3.1 ± 0.1 mm2, 1.6 ± 0.1 mm2, 0.51 ± 0.03 mm2 and 0.3 ± 0.02 mm2, respectively. Aβ SA1-LTMRs innervate only one or two touch domes (74% or 26%, respectively, n = 31 neurons in 19 animals). Both the number of innervated hair follicles and the skin area covered by the Aβ Field-LTMRs are significantly larger than other LTMR subtypes ($p < 0.001$, Student's t-test).

Figure 4.3

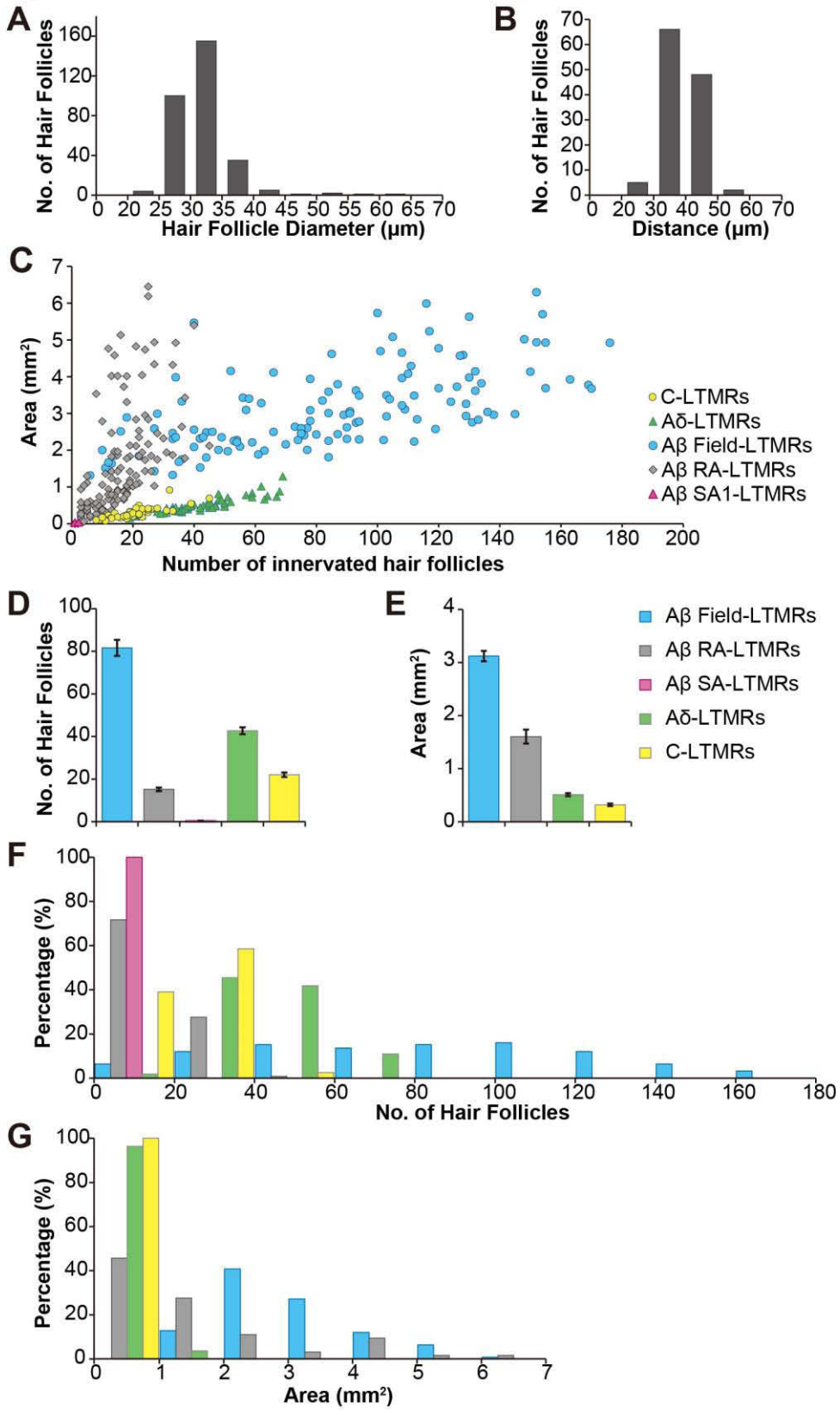
A
No. of Hair Follicles
Hair Follicle Diameter (μm)
B
No. of Hair Follicles
Distance (μm)
C
Area (mm²)
Number of innervated hair follicles
C-LTMRs
Aδ-LTMRs
Aβ Field-LTMRs
Aβ RA-LTMRs
Aβ SA1-LTMRs
D
No. of Hair Follicles
E
Area (mm²)
Aβ Field-LTMRs
Aβ RA-LTMRs
Aβ SA-LTMRs
Aδ-LTMRs
C-LTMRs
F
Percentage (%)
No. of Hair Follicles
G
Percentage (%)
Area (mm²)

Figure 4.4 Aβ Field-LTMRs have a long distance between their axon terminals and SISs.

(A-C) Whole-mount immunostaining of hairy skin reveals the relationship between Myelin Basic Protein, the spike initiation segment (SIS) as inferred from βIV-Spectrin and the terminals of three Aβ-LTMRs subtypes line (see experimental procedures for details). Arrows or arrow heads point out the SISs or nodes of Ranvier, respectively. Note that the red βIV-Spectrin puncta (arrow) in (G) is associated with a different myelinated axon that is not belong to the genetically labeled Aβ Field-LTMRs.

(D) Quantification of the distance of non-myelinated axons reveals that Aβ Field-LTMRs have longer non-myelinated axons (153 ± 50, 5 neurons) compared to Aβ RA-LTMRs (6.0 ± 1.8, 12 neurons) ($p = 0.03$, student t-test) and Aβ SA1-LTMRs (18.8 ± 0.7, 8 touch dome) ($p = 0.04$, student t-test).

Scale bar: 20 μm (A-D).

Figure 4.4

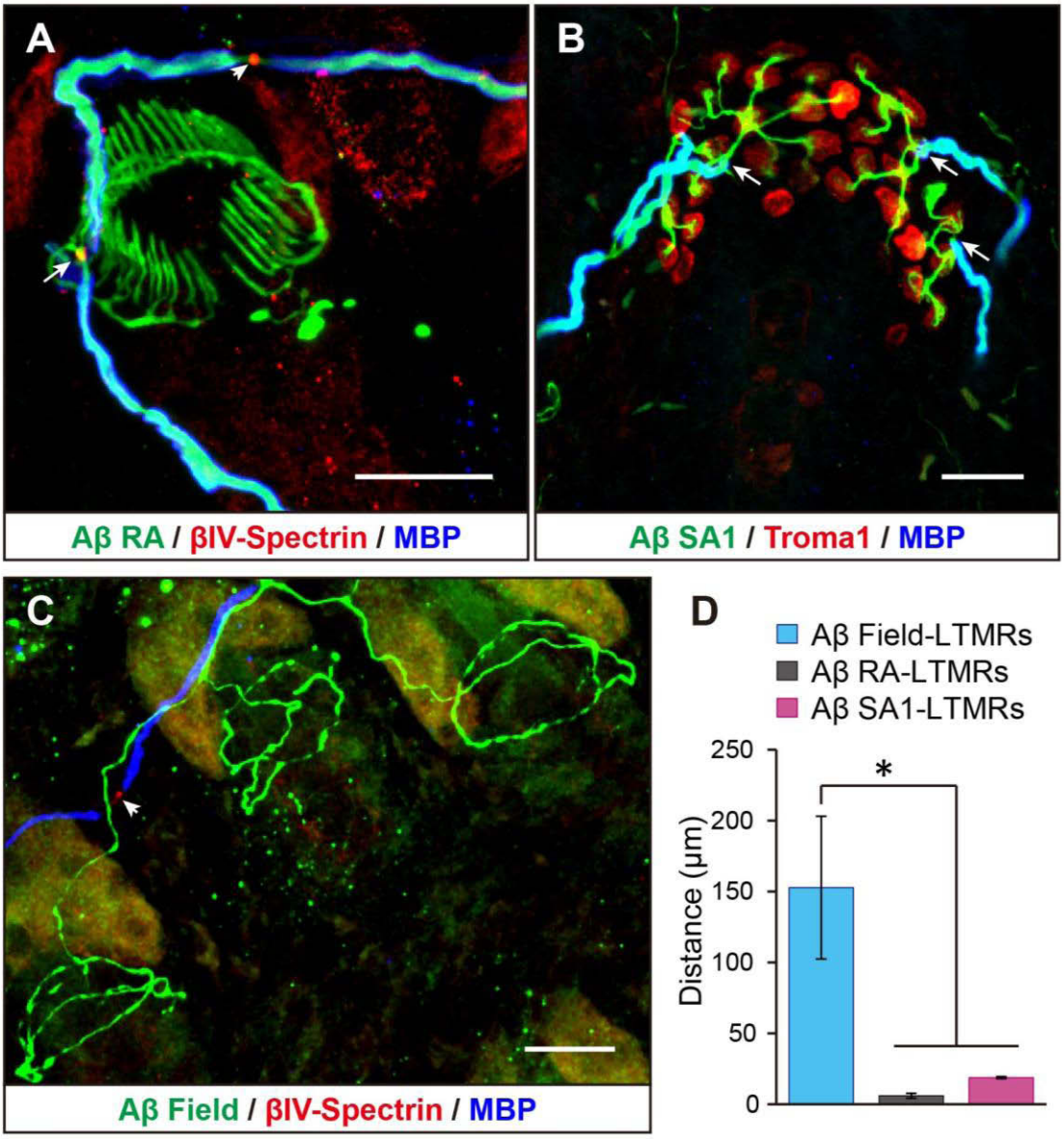
A
Aβ RA / βIV-Spectrin / MBP
B
Aβ SA1 / Troma1 / MBP
C
Aβ Field / βIV-Spectrin / MBP
D
Aβ Field-LTMRs
Aβ RA-LTMRs
Aβ SA1-LTMRs
Distance (μm)
250
200
150
100
50
0
*

Figure 4.5 Inferred SIS locations for Aβ Field-LTMRs and Aβ RA-LTMRs.

(A-C) Neuromantic tracing reveals the myelination of individual Aβ RA-LTMRs (A) and Aβ Field-LTMRs (B-C) after whole-mount staining of tdTomato and MBP of hairy skin from Ret^{CreER}; $R26^{LSL\text{-}tdTomato}$ (A) or $TrkC^{CreER}$; $R26^{LSL\text{-}tdTomato}$ (B-C) mice reveals the myelination of individual Aβ RA-LTMRs and Aβ Field-LTMRs. Tamoxifen treatment is the same as that in Figure 4.4A-C (see experimental procedures for details).

Scale bar: 500 μm (A-C).

Figure 4.5

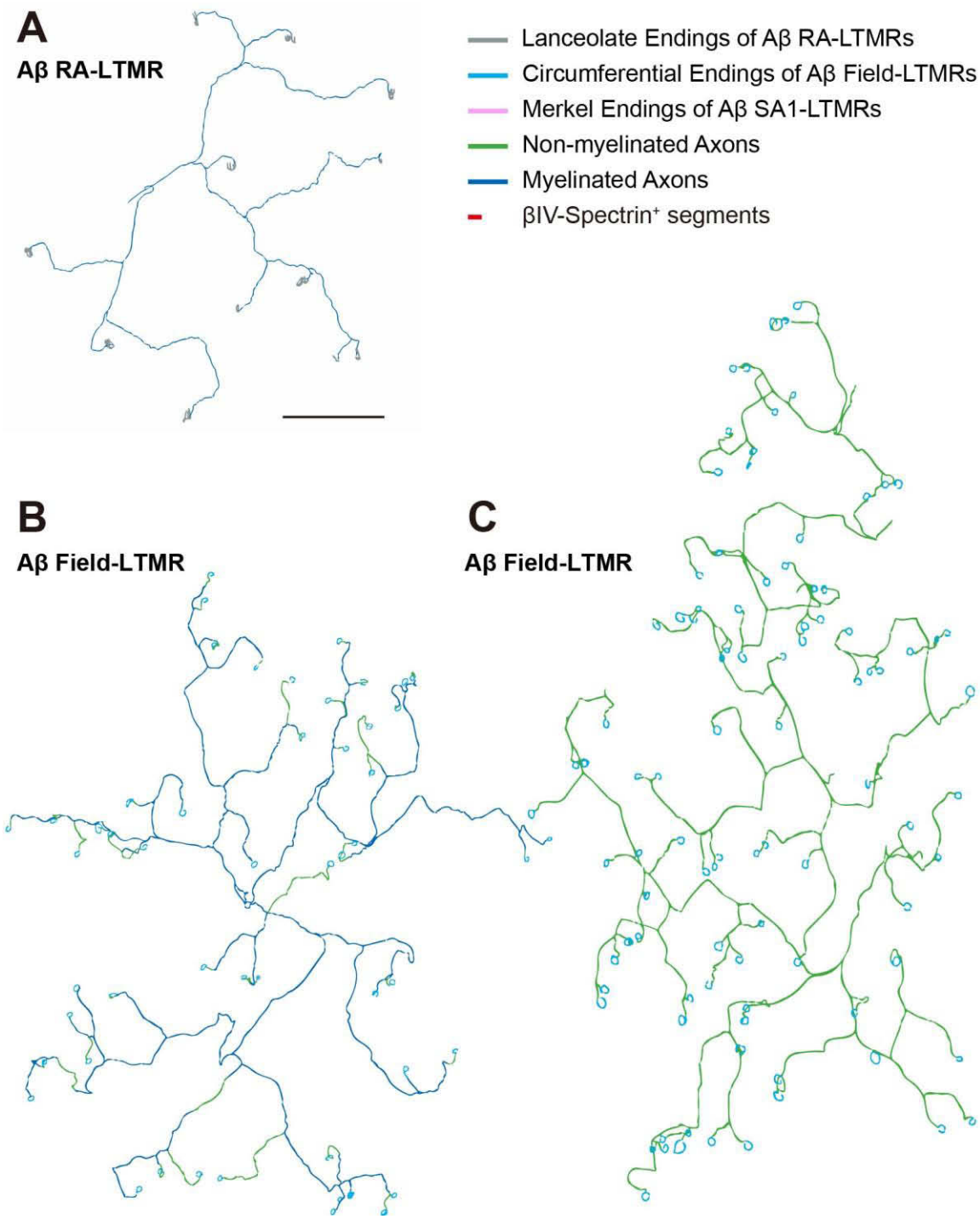
A
Aβ RA-LTMR
Lanceolate Endings of Aβ RA-LTMRs
Circumferential Endings of Aβ Field-LTMRs
Merkel Endings of Aβ SA1-LTMRs
Non-myelinated Axons
Myelinated Axons
βIV-Spectrin⁺ segments
B
Aβ Field-LTMR
C
Aβ Field-LTMR

Chapter 5. Integration of Aβ-LTMRs and PSDC projections in the DCN

Information of touch stimuli are firstly encoded by LTMR subtypes that are tuned to different mechanical stimuli. Next, signals are conveyed to the central nervous system, including the spinal cord and brainstem, where information is processed and relayed to higher level including brain. The DC of the spinal cord is a major ascending pathway that conveys touch information from the spinal cord to the first touch relay nuclei in the brainstem, the DCN, where touch information is further conveyed by DCN projection neurons to higher level including thalamus, superior colliculus, and cerebellum.

There are mainly two touch ascending pathways traveling through the DC to the DCN: the direct pathways from Aβ-LTMRs and the indirect pathways from the spinal cord PSDC neurons. In order to gain insight how information is processed in the DCN, which are major relay nuclei of touch information in the brainstem, we carried out a comprehensive analysis of the DCN innervation of different neuronal subtypes.

5.1. Aβ Field-LTMRs project to the deep spinal cord dorsal horn and the DCN

I first used the *TrkC*^{CreER}*; Ret*$^{f(CFP)}$ intersectional genetic labeling strategy to visualize the central axonal projections of Aβ Field-LTMRs. In the spinal cord of *TrkC*^{CreER}*; Ret*$^{f(CFP)}$ mice treated with tamoxifen at P5, in which the Aβ Field-LTMRs are specifically labeled by CFP, the central projections of CFP$^+$ neurons terminate within lamina II$_{iv}$ to lamina IV, partially overlapping with the PKCγ$^+$ interneurons of dorsal horn lamina II$_{iv}$ and III but not with IB4$^+$ terminals in lamina II$_{id}$ (Figure 5.1A-B). These spinal cord terminations overlap with, but are slightly more dorsal than those of other Aβ-LTMR subtypes, including Aβ RA-LTMRs (Li et al., 2011; Luo et al., 2009) and Aβ SA1-LTMRs that innervate laminar III to V (Figure 5.1E-F), and they resemble the spinal cord innervation patterns of a subset of myelinated nociceptors (Boada and Woodbury, 2008).

Furthermore, as predicted from our initial retrograde labeling findings, CFP^+ circumferential ending neurons have central projections that travel within the gracile and cuneate fasciculi of the DC (data not shown) and terminate in the gracile and the dorsal cuneate nuclei of the DCN, which are demarcated by the pattern of vGlut1 staining (Figure 5.1D). CFP^+ central axonal terminals are excluded from the ventral cuneate and external cuneate nuclei (Figure 5.1C). Thus, Aβ Field-LTMRs have central axons that resemble Aβ-LTMR subtypes that terminate within the deep dorsal horn and DCN.

5.2. Sparse genetic labeling reveals the central projection of individual Aβ-LTMR subtypes

Classical neuroanatomical and physiological studies have provided knowledge about the innervation of sensory afferents in the DCN (Horch et al., 1976). Using antidromic stimulation at the rostral DC in cat, Burgess and Horch had shown that although majority of Aβ-LTMRs project to the DCN, there's a differential innervation compared between rostral and caudal part of body. Recently, anatomical analysis using modern genetic labeling strategy has revealed that majority of Aβ RA-LTMRs directly innervate the DCN, while proprioceptors at caudal level failed to form direct projection to the DCN (Niu et al., 2013).

In order to visualize the central projections of individual Aβ Field-LTMRs, we next used a sparse genetic labeling strategy, employing $TrkC^{CreER}$ in combination with $Brn3a^{f(AP)}$, a Cre-dependent alkaline phosphatase (AP) reporter that is expressed in most of NFH^+ DRG neurons but not in the spinal cord (Badea et al., 2012). We treated mice with a low dose of tamoxifen (0.001 mg) at P8, thus cre recombination and AP expression only occurred in one or two neurons per animal. We next carried out skin, spinal cord, and brainstem whole-mount AP staining to identify labeled DRG neurons based on their peripheral terminal structures (Figure 5.2A and 5.2C). This analysis revealed that the central projections of individual Aβ Field-LTMRs bifurcate upon innervating the spinal cord, then project in both the rostral and caudal directions within the

DC and sprout multiple collaterals that span 3.7 ± 0.3 spinal segments (Figure 5.2E and 5.3A). Moreover, the rostral axonal branch of each Aβ Field-LTMRs projects to the DCN where it forms collaterals (100%, 34/34 neurons) (Figure 5.2B and 5.3A). These central projection patterns resemble other hairy skin Aβ-LTMR subtypes including Aβ RA-LTMRs (Niu et al., 2013) and Aβ SA1-LTMRs, which form collaterals spanning 3.9 ± 0.2 spinal segments (Figure 5.2F and 5.3B) and innervate the DCN (Figure 5.2D) although, interestingly, this analysis revealed that the majority of Aβ SA1-LTMRs in DRGs below T10 do not project to the DCN (73%, 16/22 neurons fail to project to the DCN, Figure 5.3B). Together, while Aβ RA-LTMRs and Aβ Field-LTMRs convey information directly to the brainstem, Aβ SA1-LTMRs must reach there through an indirect pathway, possibly through the postsynaptic dorsal column (PSDC) pathway.

5.3. Retrograde labeling revealed PSDC neurons, a spinal cord population projecting to the DCN

The DCN also receive ascending innervation from PSDC neurons, which are located in the deep lamina of spinal cord dorsal horn and relay touch and pain information to the brainstem (Britain, 1988; Cliffer and Cliffer, 1985; Madsen, 1984). In order to visualize PSDC neurons in mice, Victoria Abraira, a postdoc in the lab, piloted retrograde labeling by injecting CTB-555 into the rostral DC at the first cervical level (C1). Transverse section reveals that CTB-555 labeled PSDC neurons are located in laminae III-IV of the spinal cord dorsal horn at cervical, thoracic, and lumbar level (Figure 5.4A-B) and do not overlap with laminae innervated by $IB4^{+}$ nociceptors or $TrkB\text{-}GFP^{+}$ Aδ-LTMRs (Figure 5.4B and 5.4C). These laminae are also densely innervated by Aβ-LTMRs, including Aβ SA1-LTMRs, Aβ Field-LTMRs, and Aβ RA-LTMRs that are genetically labeled by $TrkC^{CreER}$; $Ret^{f(CFP)}$ or Npy2r-GFP mice which have been described previously (Figure 5.4B', 5.4D-E), suggesting PSDC neurons may receive input from Aβ-LTMRs. By injecting CTB into the DC of $vGlut2^{Cre}$; $Tau^{LSL\text{-}lacZ}$ or $vGat^{iCre}$; $Tau^{LSL\text{-}lacZ}$ mice, I

further showed that all the CTB^+ PSDC neurons are excitatory (98.2 ± 0.8%, n = 4, Figure 5.5A) but not inhibitory (3.3% ± 1.2%, n = 3, Figure 5.5B).

To further visualize the distribution pattern of PSDC neurons, I injected CTB-488 into the C1 DC to label PSDC neurons and cleared the whole spinal cord with BABB after tissue fixation. A dorsal view of the spinal cord reveals that PSDC neurons are evenly distributed from medial to lateral at the thoracic level (Figure 5.6A and 5.6F). However, there's a dramatic enrichment of PSDC neurons at the medial region of the lumbar spinal cord (Figure 5.6B, 5.6C, and 5.6F). The medial region of lumbar spinal cord is known to receive input from hindpaw glabrous skin in rat and cat (Fuchs; Takahashi et al., 2002), suggesting that the PSDC enriched spinal cord region might be involved in processing stimuli on glabrous skin, which has high spatial acuity. In order to test this hypothesis, I further injected CTB-546 or CTB-647 into different regions of the hind leg to retrogradely label cutaneous DRG neuron and their central terminals in the spinal cord. Indeed, the CTB labeled glabrous skin neurons innervate the medial most region of the lumbar spinal cord (Figure 5.6B'), while CTB labeled hind paw hairy skin region, including the lateral side and the back of the paw, innervate a more lateral region(Figure 5.6B' and 5.6C'). These regions have the highest density of PSDC neurons (Figure 5.6F). In contrast, CTB labeled thigh hairy skin neurons innervate the lateral most region of the spinal cord (Figure 5.6C'), where the density of PSDC neurons is much lower (Figure 5.6F).

5.4. The direct (sensory) and indirect (PSDC) pathways converge in the DCN following somatotopic organization

The DCN is known as an important relay center for the touch sensation. Touch information ascends to the DCN through both Aβ-LTMRs (the direct pathway), and the PSDC neurons (the indirect pathway). There information is further processed and conveyed to higher levels of central nervous system. To gain insight into the logic of touch information processing in the DCN, I

examined the anatomical organization of central endings from Aβ-LTMRs and PSDC neurons in this region. Classical physiological and anatomical studies demonstrated that the DCN are organized somatotopically in a caudal-medial and rostral-lateral manner: the caudal body is represented in the gracile nuclei which is located in the medial region, while the rostral body is represented in the cuneate nuclei which locate in the lateral region of the DCN (Millar and Basbaum, 1975). In order to better visualize the somatotopic organization of the direct pathway, I first decided to trace the central projections of sensory neurons innervating different dermatome. AAV2/1-Cre virus was injected into the forepaw glabrous skin, hindpaw glabrous skin, or back hairy skin of $R26^{LSL\text{-}syn\text{-}tdTomato}$ mice to retrogradely infect DRG neurons and visualize their brainstem axonal projections. In the transverse section of the DCN, tdTomato^{+} synaptic boutons from forepaw glabrous skin neurons innervate the ventral-lateral region of cuneate nuclei (Figure 5.7A, D, and G), those from hindpaw glabrous skin neurons occupied the main region of the gracile nuclei (Figure 5.7C, F and I), while those from back hair skin are located between the forepaw and hindpaw innervated DCN region and are located in the medial region of cuneate nuclei (Figure 5.7B, E, and H). Interestingly, tdTomato^{+} neurons from glabrous skin labeling tend to form more synaptic boutons in the DCN and occupy larger region, consistent with the homunculus of touch information representation in the DCN in which limb region are represented in a larger region.

In order to further reveal the fine structure of DCN somatotopic organization, I developed a dual labeling strategy to compare the DCN innervation pattern of neurons projecting to adjacent skin regions. Here AAV2/1-Flpo and AAV2/1-Cre viruses were injected into adjacent locations on the skin of $R26^{LSL\text{-}GFP}/R26^{FSF\text{-}tdTomato}$ mice (Figure 5.8A-E). I found that neurons projecting to forepaw hairy skin and glabrous skin innervate adjacent but non-overlapping region of the DCN, in which the glabrous skin projecting neurons innervate more medial and caudal region of the cuneate, while the hairy skin projecting neurons innervate a region that is more dorsal and rostral

(Figure 5.8B-B''). A similar adjacent but non-overlapping innervation is found for neurons innervating the dorsal and ventral side of the forelimb (Figure 5.8A-A"), adjacent skin region on the back hairy skin (Figure 5.8C-D"), or the glabrous skin and hairy skin of the hindpaw (Figure 5.8E-E"), though their axonal arborizations occupied a smaller area of the DCN compared to the forepaw projecting neurons.

The anatomical analysis using virus tracing confirmed that the DCN innervation from cutaneous sensory neurons (the direct pathway) are organized somatotopically. Meanwhile, the central innervations of the direct and indirect pathways are overlapping in the DCN. Thus it appears that the direct and indirect pathways responding to the same dermatome stimulation may converge onto a similar region in the DCN. To test this idea, I used a dual recombination dependent reporter line *RC::FrePe* (*Rosa*$^{frt\text{-}stop\text{-}frt\text{-}loxp\text{-}mCherry\text{-}stop\text{-}loxp\text{-}EGFP}$) which we obtained from Dr. Susan Dymecki. AAV2/1-Flpo virus was injected into the spinal cord dorsal horn at cervical, thoracic, or lumbar levels to infect both spinal cord neurons as well as DRG neurons located in or projecting to the injection site. By combining virus injections with the dual recombination reporter line *RC::FrePe* and the primary sensory specific Cre line *Advillin*^{Cre}, PSDC neurons and DRG neurons nearby the injection site will be labeled by either mCherry or EGFP, respectively. Indeed, we found that the terminations of PSDC neurons and DRG neurons converge onto the same region of the DCN following somatotopic organization: neurons labeled by cervical spinal cord injection innervate the ventral lateral region of the cuneate nuclei (Figure 5.9A-A'), those labeled by lumbar spinal cord injection innervate the gracile nuclei (Figure 5.9C-C'), while those labeled by thoracic spinal cord injection innervate a narrow band between the gracile and cuneate nuclei (Figure 5.9B-B'), resembling the somatotopic map revealed by cutaneous sensory neuron labeling.

Taken together, using a combination of retrograde tracing and genetic sparse labeling, I found that PSDC neurons and the majority of the Aβ-LTMRs directly project through the DC to the DCN of the brainstem. Genetic labeling in combination with anterograde tracing from the skin or spinal cord revealed that innervation by Aβ-LTMRs as well as PSDCs converge within the DCN in a somatotopic manner, suggesting a mechanism of tactile information integration across different ascending pathways.

Figure 5.1 Aβ Field-LTMRs innervate lamina II_{iv} to V of the dorsal spinal cord as well as the DCN of the brainstem.

(A-B) In transverse spinal cord sections from *TrkC*^{CreER}*; Ret*$^{f(CFP)}$ mice treated with tamoxifen postnatally (0.1mg at P5 by intraperitoneal injection), the central projections of Aβ Field-LTMRs labeled by CFP (green) are located in lamina II_{iv} through IV (n = 9 animals). These central projects are ventral to the lamina II_{id} labeled by IB4 (red) (A) and are partially overlapping with lamina II_{iv} labeled by PKCγ (red) (B).

(C-D) Transverse brainstem sections from *TrkC*^{CreER}*; Ret*$^{f(CFP)}$ mice treated with tamoxifen postnatally reveal the innervation pattern in the DCN, which is marked by vGlut1 (red). Aβ Field-LTMRs labeled by CFP (green) innervate gracile nucleus and dorsal cuneate nucleus, but do not innervate external cuneate nucleus or ventral cuneate nucleus.

(E-F) In transverse spinal cord sections from *TrkC*^{CreER}*; Ret*$^{f(CFP)}$ mice treated with tamoxifen embryonically (3mg at E12.5 by oral gavage), the central projections of Aβ SA1-LTMRs labeled by CFP (green) are located in lamina III through V (n = 4 animals), ventrally to the lamina II_{id} and lamina II_{iv} labeled by IB4 (E) and PKCγ (F), respectively.

Scale bar: 100 μm (A-F)

Figure 5.1

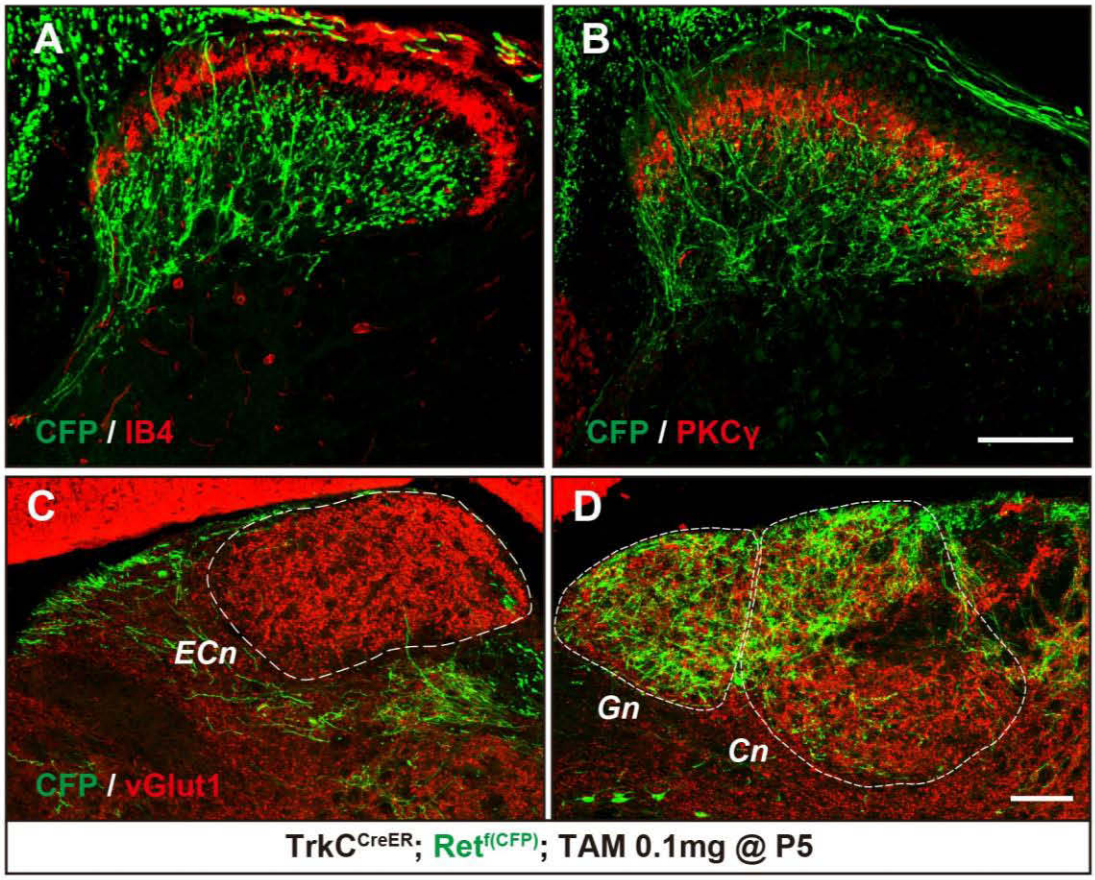
A
CFP / IB4
B
CFP / PKCγ
C
ECn
CFP / vGlut1
D
Gn
Cn
TrkC^CreER; Ret^f(CFP); TAM 0.1mg @ P5
E
CFP / IB4
F
CFP / PKCγ
TrkC^CreER; Ret^f(CFP); TAM 3mg @ E12.5

Figure 5.2 Sparse labeling reveals the central projection of individual Aβ-LTMRs.

(A-F) Whole-mount AP staining of the skin (A and C), brainstem (B and D), and spinal cord (E and F) from *TrkC^{CreER}; Brn3a$^{f(AP)}$* mice treated with 0.001mg tamoxifen at P8 (by intraperitoneal injection) reveals the peripheral terminals and central projections of a single Aβ Field-LTMR or Aβ SA1-LTMR. Using this strategy, one to two neurons are labeled per animal. Only neurons forming circumferential or Merkel endings in skin are further used for central projection analysis (n = 34 neurons with circumferential endings and n = 50 neurons with Merkel endings).

(A, C) Axonal branches from individual neurons arborize and form circumferential endings (A) or Merkel endings (C) on thoracic hairy skin of the left side of the animal.

(B, D, E and F) Dorsal view of the left DCN (B and D) and left thoracic spinal cord (E and F) reveals that axons from labeled Aβ Field-LTMRs and Aβ SA1-LTMRs project into the spinal cord at the level of T12 (E) or T11 (F), branching to form collaterals in both the rostral and caudal directions that cover three spinal segments (E and F). The rostral end of this axon extends to the DCN, where it forms collaterals (B and D).

Scale bar: 200 μm (A-F).

Figure 5.2

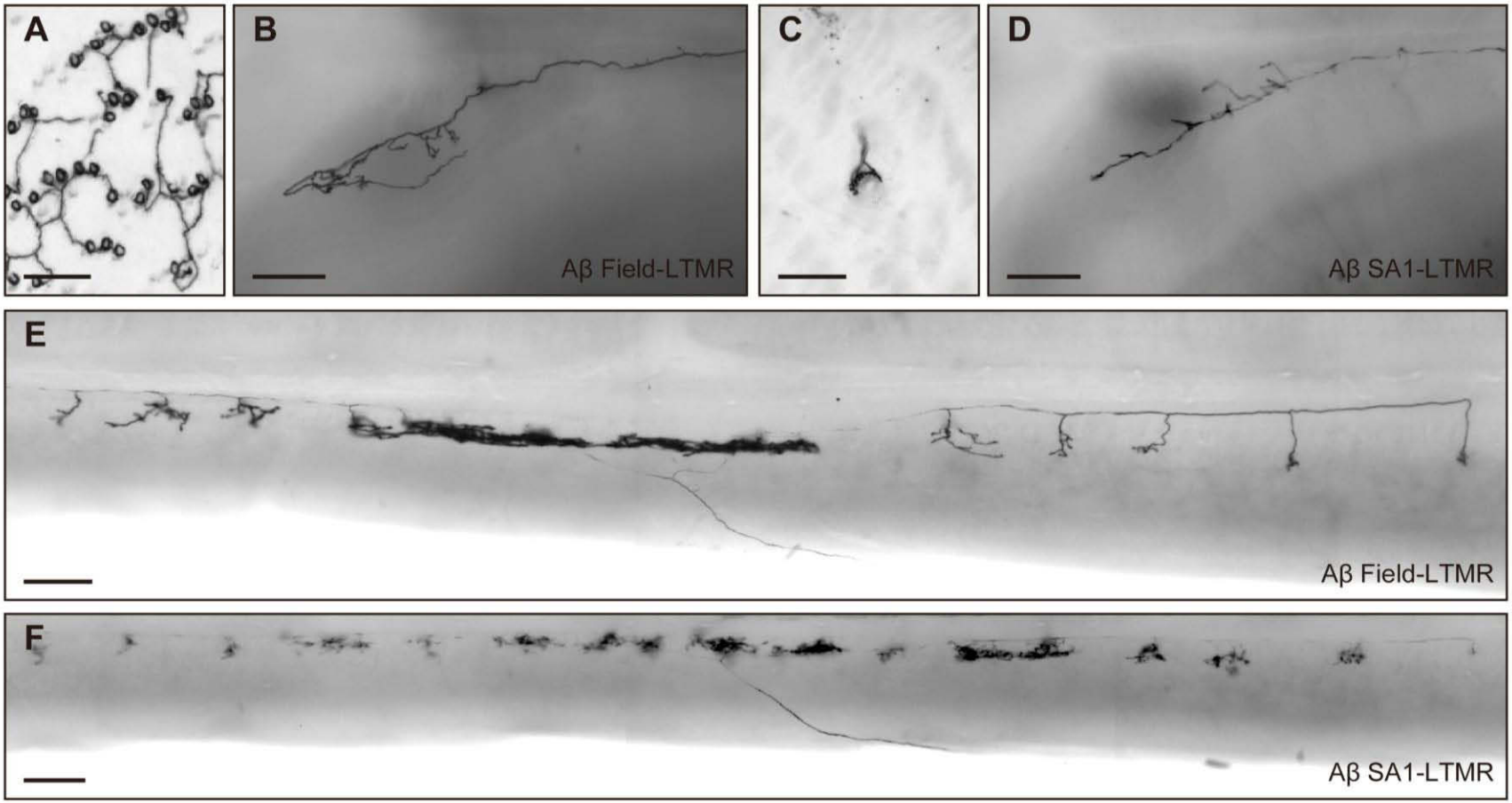

Figure 5.3 Sparse genetic labeling reveals the central projection pattern of Aβ Field-LTMRs and Aβ SA1-LTMRs.

(A-B) Summary of central projection patters of ascending axons and collaterals of 34 Aβ Field-LTMRs from 34 animals (A) and 50 hairy skin Aβ SA1-LTMRs from 50 animals (B). Black dots indicate where the cell bodies are located; blue lines indicate the ascending axons; red lines indicate the levels in which axonal collaterals for each neuron are present. All Aβ SA1-LTMRs rostral to T11 (28/28 neurons) and all Aβ Field-LTMRs (34/34 neurons) directly project to DCN, whereas only 27% of hairy skin Aβ SA1-LTMRs caudal to T10 (6/22 neurons) reach the DCN.

Figure 5.3

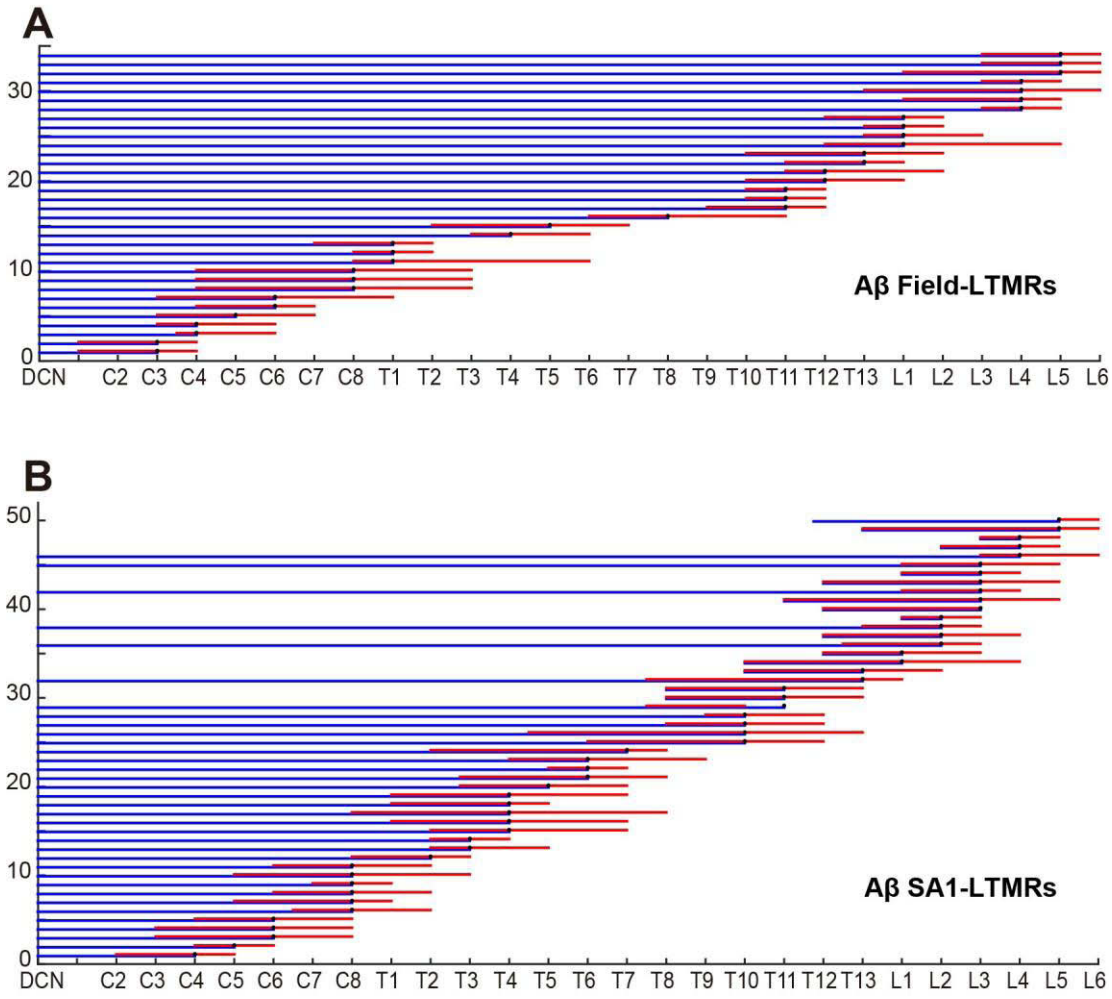
A
30
20
10
0
Aβ Field-LTMRs
DCN C2 C3 C4 C5 C6 C7 C8 T1 T2 T3 T4 T5 T6 T7 T8 T9 T10 T11 T12 T13 L1 L2 L3 L4 L5 L6
B
50
40
30
20
10
0
Aβ SA1-LTMRs
DCN C2 C3 C4 C5 C6 C7 C8 T1 T2 T3 T4 T5 T6 T7 T8 T9 T10 T11 T12 T13 L1 L2 L3 L4 L5 L6

Figure 5.4 Retrograde labeling reveals that PSDC neurons are located in the LTMR recipient zone.

(A) Transverse sections of spinal cord showing the distribution of PSDC neurons at cervical, thoracic, and lumbar levels. Note the cervical section is close to the injection site (C1-C2, DC) so there may be non-specific labeling.

(B-D) Transverse spinal cord sections from the following mouse lines to label distinct LTMR and PSDC neuronal populations: *TrkC*^{CreER}*; Ret*$^{f(CFP)}$ mice treated with 0.1mg Tamoxifen at P5 (B and B'), *TrkB*^{mGFP} mice (C), *TrkC*^{CreER}*; Ret*$^{f(CFP)}$ mice treated with 3mg Tamoxifen at E12.5 (D), and *Npy2r-GFP* mice (D) with CTB-555 DC injection. The CTB retrogradely-labeled PSDC neurons are located in the recipient zone of Aβ SA1-LTMRs (B'), Aβ Field-LTMRs (D), and Aβ RA-LTMRs (E), but do not overlap with the central terminals of Aδ-LTMRs (C).

Scale bar: 100 μm (B-E).

Figure 5.4

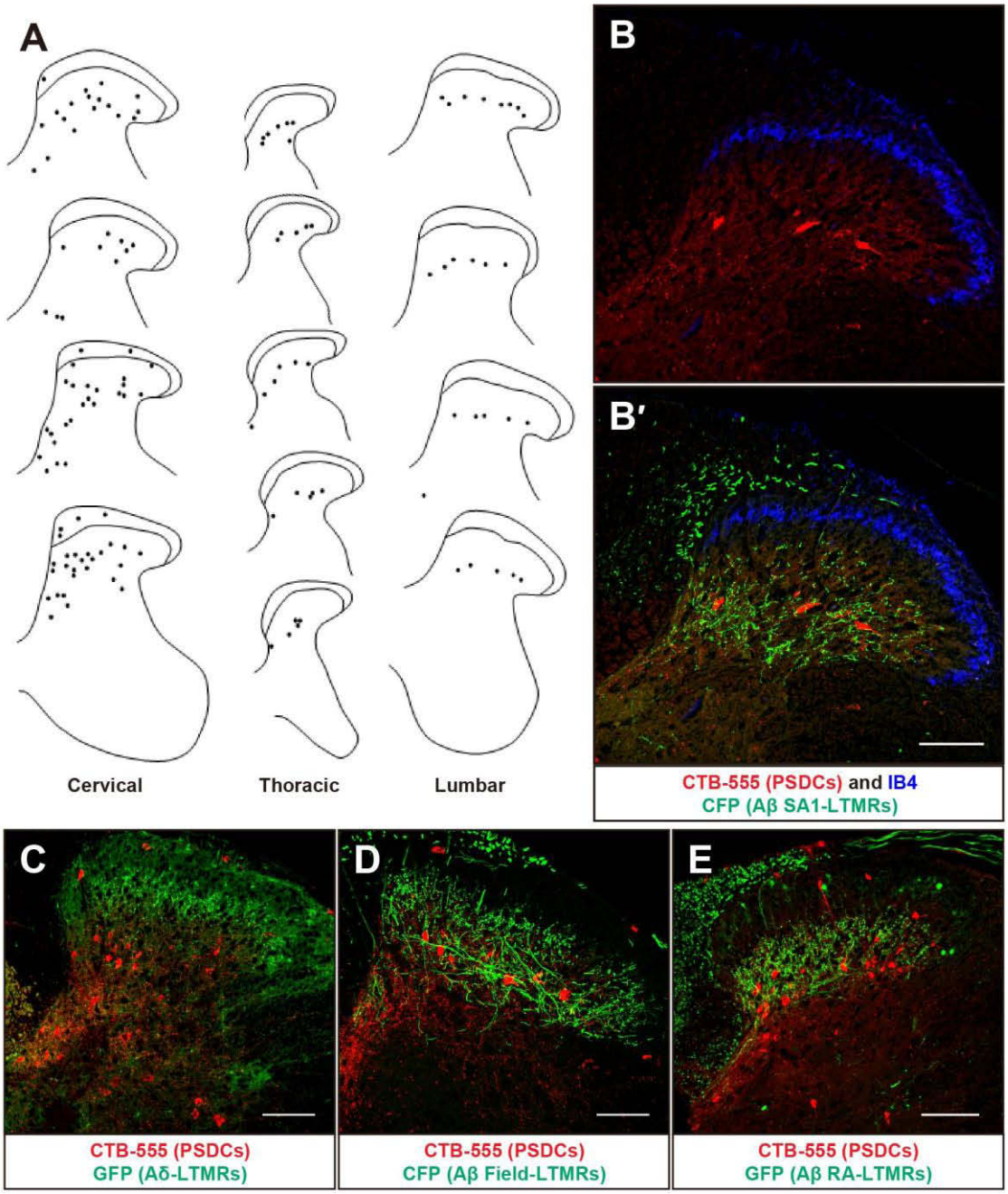
A
Cervical
Thoracic
Lumbar
B
B′
CTB-555 (PSDCs) and IB4
CFP (Aβ SA1-LTMRs)
C
CTB-555 (PSDCs)
GFP (Aδ-LTMRs)
D
CTB-555 (PSDCs)
CFP (Aβ Field-LTMRs)
E
CTB-555 (PSDCs)
GFP (Aβ RA-LTMRs)

Figure 5.5 PSDC neurons are excitatory.

(A-B) Sagittal spinal cord sections from *vGlut2*^{Cre}*; Tau*$^{LSL\text{-}lacZ}$ (A) or *vGat*^{iCre}*; Tau*$^{LSL\text{-}lacZ}$ (B) mice after CTB-488 DC injection. All CTB-488^{+} PSDC neurons are βGal^{+} from *vGlut2*^{Cre}*; Tau*$^{LSL\text{-}lacZ}$ mice (A) and thus are excitatory (98.2 ± 0.8%, n = 4). CTB-488^{+} PSDC neurons are βGal^{-} from *vGat*^{iCre}*; Tau*$^{LSL\text{-}lacZ}$ mice (B), and thus are not inhibitory (3.3% ± 1.2%, n =3).

Scale bar: 200 μm (A-B).

Figure 5.5

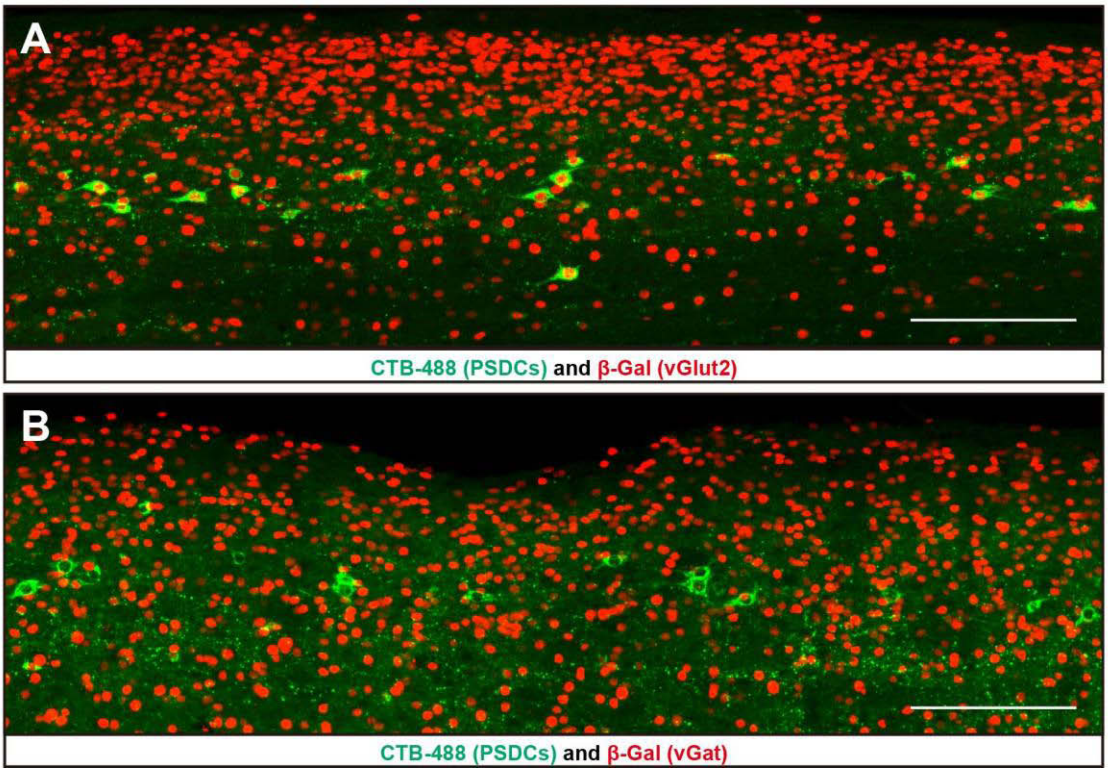

Figure 5.6 PSDC neurons are enriched in the glabrous skin-innervating zones in the spinal cord.

(A-D) CTB-488 C1 DC injection and CTB-546/647 skin injection reveal the distribution of PSDC neurons compared to the central innervation pattern of neurons innervating different skin regions. (A-C) Dorsal view of the right side of the spinal cord after BABB clearance shows that CTB-488+ PSDC neurons are evenly distributed from medial to lateral at the thoracic level (A), while they are enriched at the medial region of the lumbar spinal cord (B and C). CTB-546 or CTB-647 injections reveal that the medial region of lumbar spinal cord receives inputs from hindpaw glabrous skin (CTB-546, B'), while the lateral region of lumbar spinal cord receives inputs from other region of the hind paw, including dorsal hairy skin (CTB-647, B'), lateral side of hindpaw (CTB-647, D), and thigh hairy skin (CTB-546, D).

(D-E) Transverse spinal cord sections reveal the distribution of PSDC neurons (CTB-488),compared to the central innervation pattern of lateral hind paw (CTB-647) or the thigh (CTB-546). The locations of sections are marked on (C').

(F) Quantification of the density of PSDC neurons through medial to lateral regions at lumbar and thoracic spinal cord levels.

Scale bar: 500 μm (A-E).

Figure 5.6

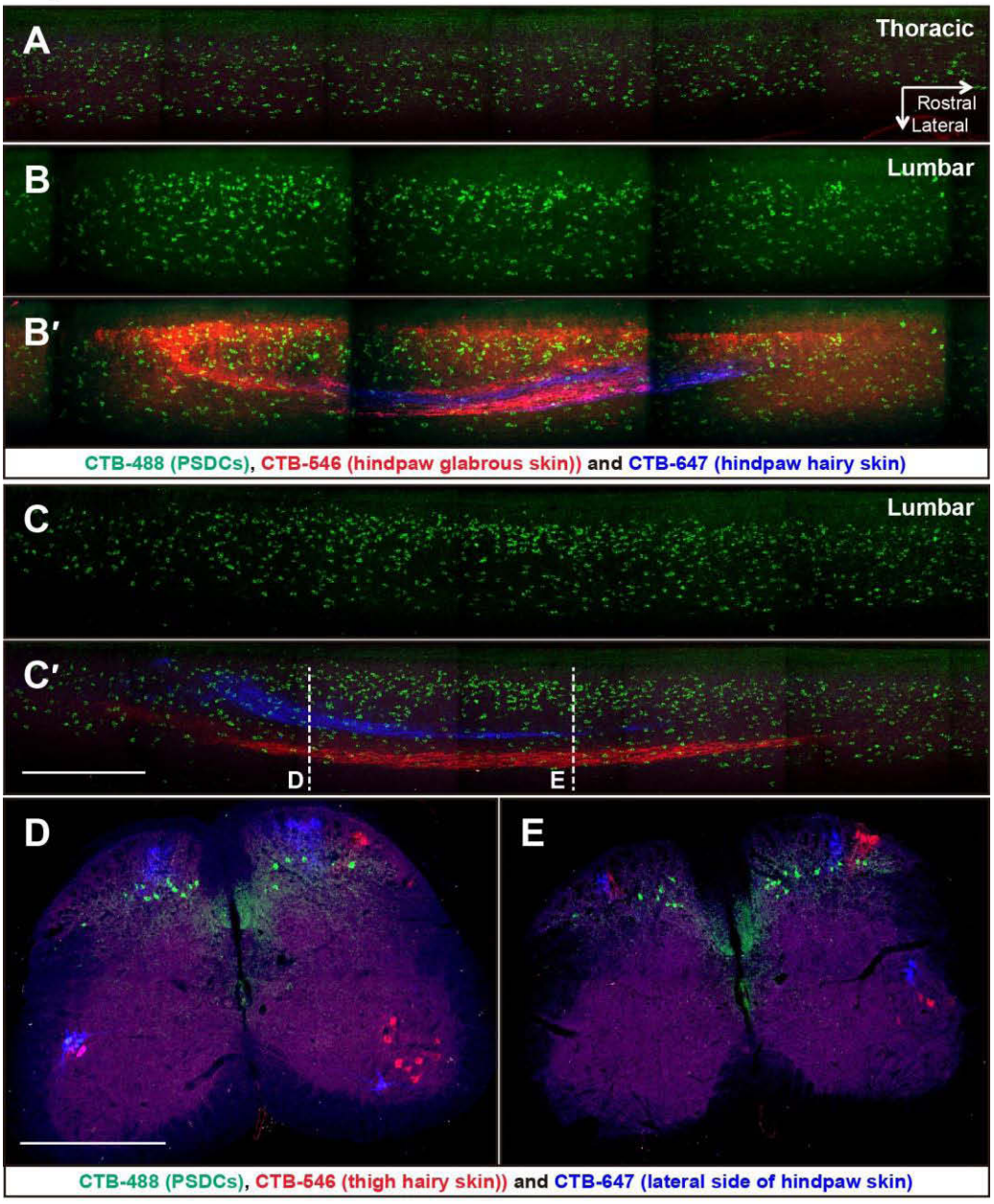
A
Thoracic
Rostral
Lateral
B
Lumbar
B′
CTB-488 (PSDCs), CTB-546 (hindpaw glabrous skin)) and CTB-647 (hindpaw hairy skin)
C
Lumbar
C′
D
E
D
E
CTB-488 (PSDCs), CTB-546 (thigh hairy skin)) and CTB-647 (lateral side of hindpaw skin)

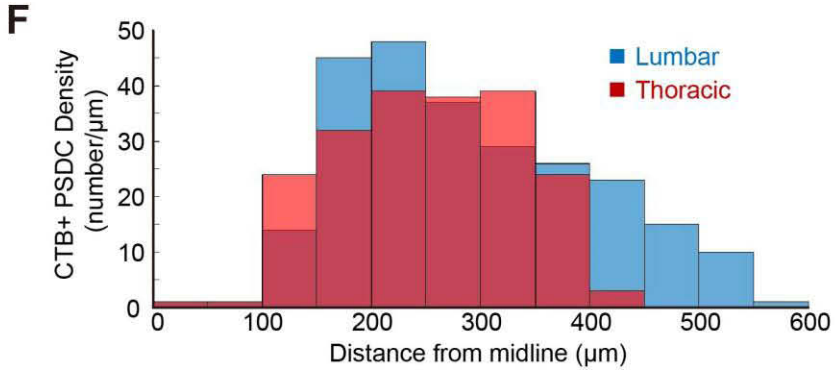
F
CTB+ PSDC Density
(number/µm)
50
40
30
20
10
0
0
100
200
300
400
500
600
Distance from midline (µm)
Lumbar
Thoracic

Figure 5.7 LTMRs innervating the DCN exhibits a somatotopic organization.

(A-I) The forepaw glabrous skin (A, D, and G), back hairy skin (B, E, and H), and hindpaw glabrous skin (C, F and I) of $R26^{LSL\text{-}tdTomato}$ mice was injected with AAV2/1-Cre virus to infect DRG neurons and visualize their central projection pattern in the DCN.

(A-C) Schematic shows the injection sites of AAV2/1-Cre virus.

(D-I) Double immunostaining of vGlut1 and tdTomato of transverse brainstem sections reveals the rostral (D-F) and caudal (G-I) DCN projections of $tdTomato^{+}$ DRG neurons that are infected by AAV2/1-Cre skin injection. The gracile nuclei and cuneate nuclei of the DCN are marked with dashed lines. Gn: gracile nucleus; Cn: cuneate nucleus.

Scale bar: 100 μm (D-I).

Figure 5.7

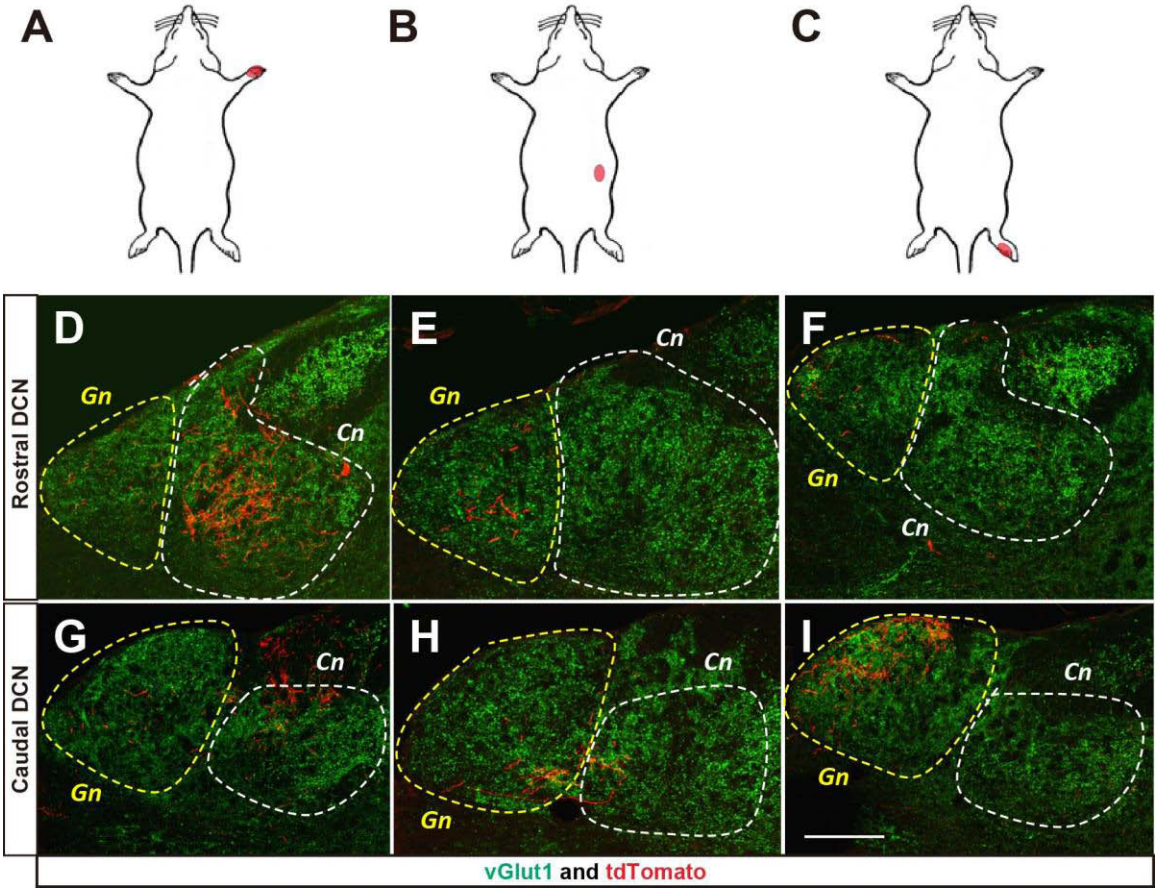

Figure 5.8 Dual virus injection reveals the DCN innervation pattern from adjacent skin regions.

(A-E) Adjacent skin regions of $R26^{LSL\text{-}GFP}/R26^{FSF\text{-}tdTomato}$ mice were injected with AAV2/1-Flpo and AAV2/1-Cre viruses to infect DRG neurons and label them with tdTomato or GFP reporter, respectively. Left: Schematic shows the injection sites of AAV2/1-Cre virus (green) and AAV2/1-Flpo virus (red). Right: Immunostaining of vGlut1, GFP, and tdTomato of transverse brainstem sections reveals the rostral (A'-E') and caudal (A"-E") DCN projections of GFP^+ and $tdTomato^+$ DRG neurons that innervate adjacent skin regions as indicated in the schematics (A-E).

Scale bar: 200 μm (A-E).

Figure 5.8

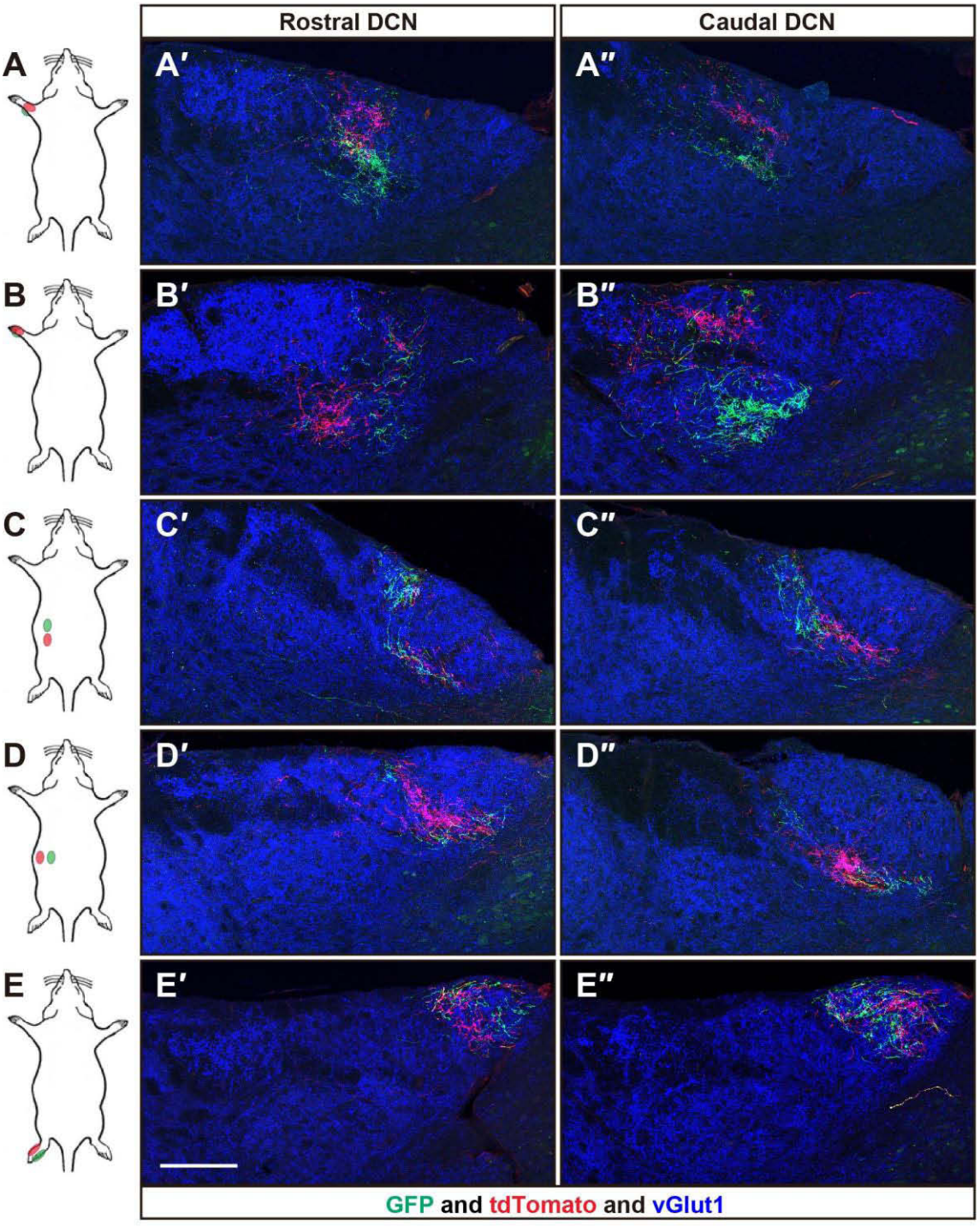
Rostral DCN
Caudal DCN
A
A′
A″
B
B′
B″
C
C′
C″
D
D′
D″
E
E′
E″
GFP and tdTomato and vGlut1

Figure 5.9 Axonal projections of LTMRs and PSDCs converge in the DCN and exhibit somatotopic organization.

(A-C) The cervical (A and A'), thoracic (B and B'), and lumbar (C and C') spinal cord dorsal horn of *Advillin*^{Flpo}*; R26::FrePe* mice were injected with AAV2/1-Cre to infect DRG neurons and spinal cord neurons and label them with GFP or mCherry, respectively. Immunostaining of vGlut1, GFP, and tdTomato of transverse brainstem sections reveals the rostral (A-C) and caudal (A'-C') DCN projections of GFP^{+} sensory neurons and tdTomato^{+} spinal cord PSDC neurons from cervical (A-A'), thoracic (B-B'), and lumbar regions (C-C').

Scale bar: 100 μm (A-C).

Figure 5.9

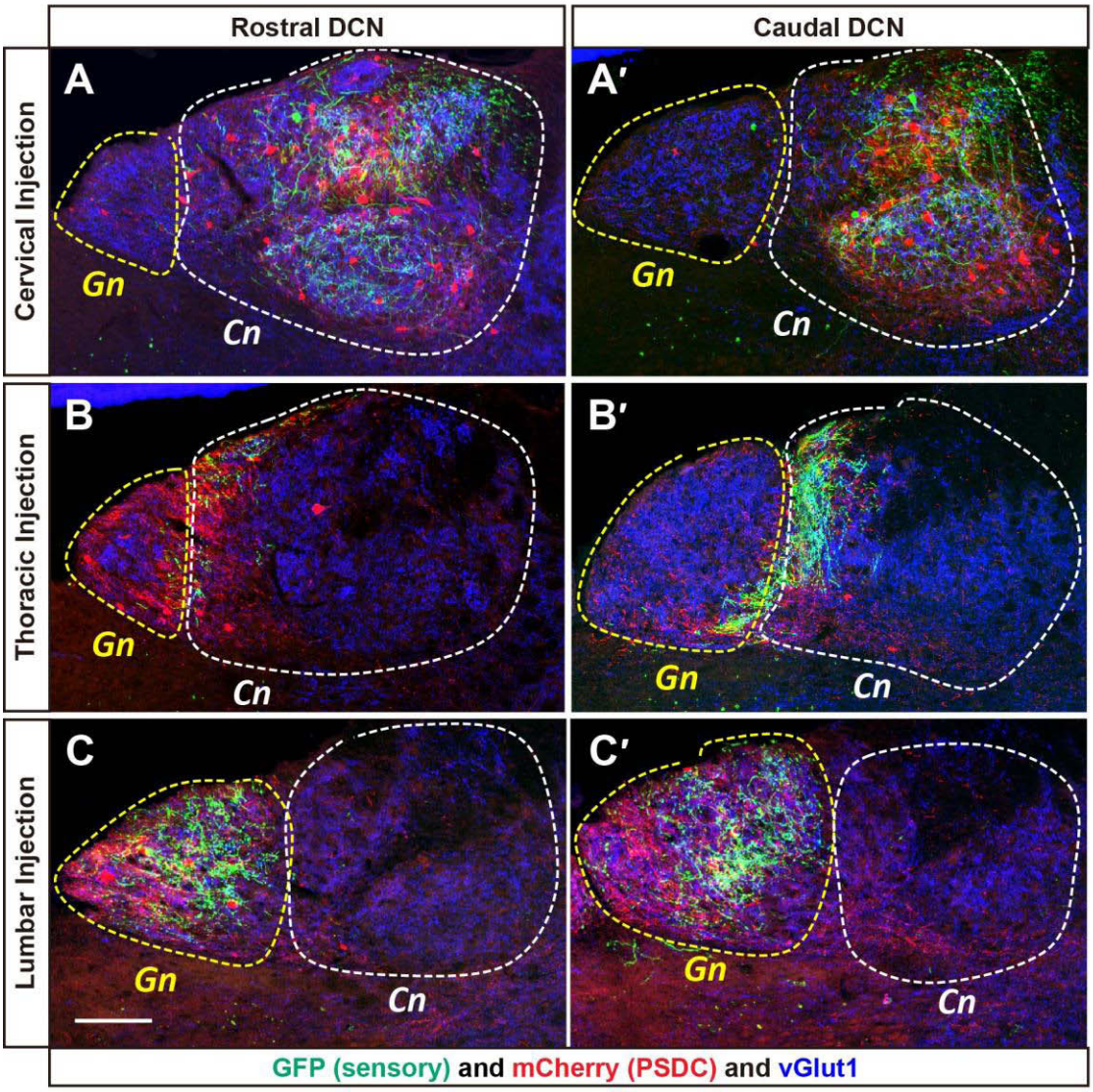
Rostral DCN
Caudal DCN
Cervical Injection
Thoracic Injection
Lumbar Injection
A
A′
B
B′
C
C′
Gn
Cn
GFP (sensory) and mCherry (PSDC) and vGlut1

Chapter 6. The function of the DC pathway in peripheral neuropathic pain

Classic lesion studies in cats, non-human primates, and human patients have revealed that the DC is involved in the discriminative touch sensation. In contrast, the anterolateral tract (ALT), which ascends through ventral or lateral regions of the spinal cord, is known to carry temperature, itch and pain sensations. However, the functions of the two major ascending pathways under pathological conditions have not yet been tested. It is thought that the ALT is also required for cutaneous pain under most of the pathological conditions due to its important role in pain sensation under non-pathological status, though this hypothesis lacks of direct evidence.

In this chapter, I focus on one type of pathological condition, named traumatic peripheral neuropathic pain, which is a chronic pain caused by injury of peripheral axons of somatosensory neurons. Decades of studies have identified molecular and cellular mechanisms underlying the traumatic peripheral neuropathy, which are believed to converge onto the spinal cord projection neurons ascending through the ALTs. However, lesion studies in rat have suggested an involvement of the DC pathway, instead of the ALT, in the development of traumatic peripheral neuropathy. In this chapter, I examined the hypothesis that traumatic peripheral neuropathic pain develops through a non-traditional pain pathway, the DC pathway, and further dissect out the spinal cord ascending circuits involved in this process using a combination of molecular genetics, retrograde virus tracing, and mouse behavioral studies.

6.1. The dorsal column pathway is required for the development of peripheral neuropathic pain after SNI

I first examined the effects of severing the dorsal column of the mouse spinal cord at the C1-C2 level to disrupt the DC pathway bilaterally, or hemisecting the left spinal cord at C8 level (but sparing the left DC) to disrupt the ALT for the right side of the body. The sham control mice for

these experiments underwent similar surgery but without spinal cord lesions. The DC lesion has been confirmed using *Avil*^{Flpo}*; R26*$^{FSF\text{-}GFP}$ mice in which all sensory neurons are labeled by GFP. In the sham control or spinal cord hemisection mice, GFP^{+} somatosensory neurons innervate the DCN in the brainstem (Figure 6.1A and 6.1C), while in the DC lesioned mice, the DCN innervation is fully abolished (Figure 6.1B), reveal the DC lesion is efficient to disrupt the DC ascending pathway.

After behavioral testing, I also injected AAV2/1-tdTomato virus into the right side of lumbar spinal cord to infect spinal cord neurons and DRG neurons close to the injection site. Lesions of spinal cord were confirmed by visualizing the projections of tdTomato^{+} axons in the DC and the ALT (data not shown). The rostral DC and DCN projections were fully abolished after the DC lesion. While in the spinal cord hemisected mice, the lateral component of ALT are fully abolished. These ALT axons innervate the parabrachial nuclei, superior colliculus, and the thalamus, as observed in serial sections. However, there are a small group of axons located at the medial region of the ALT that are spared, probably due to their deep and medial location. These axons innervate the inferior olive which originates from the intermediate or ventral regions of spinal cord (Flavell et al., 2014) and may not belong to somatosensory ascending pathways.

Four weeks after the lesion, behavioral tests were carried out to examine general motor function, thermal responses, and mechanical responses before/after the peripheral nerve injury. Firstly, there is no difference between the DC lesion group and sham control group on the rotarod and wire hang tests, suggesting that motor function of the lesioned mice recover to a normal level following surgery (Figure 6.2A-B). The DC lesion group showed no differences on the thermal behavior tests, including Hargreaves test and hot/cold plate test (Figure 6.3A-D), consistent with the idea that DC pathway is not involved in thermal pain. In contrast, hemisection of the left C8 spinal cord led to an mild increase of withdraw latency of the right hindpaw in the Hargreaves

test (Figure 6.3D), suggesting a contribution of ALT in the thermal pain detection. The same group of hemisection mice showed no difference in the hot/cold plate (Figure 6.3A-C). This may due to a requirement of both left and right side of body in the hot/cold plate test, or the compensation between different somatosensory ascending pathways, or a spinal cord reflex underlies the behavior response. What's more, there is also no difference between the lesion group and sham group of the glabrous skin mechanical threshold examined by von Frey filament, or the hairy skin mechanical sensitivity examined by the tactile PPI (Orefice et al., 2016) (Figure 6.2C-F and 6.4), which may reflect the redundancy and compensation of those two pathways in the detection of touch stimuli.

After baseline testing, I induced peripheral neuropathic pain using the spare nerve injury (SNI) model, a well-established injury model to study the traumatic peripheral neuropathy, and examined the mechanical response at 2 days, 8 days, and 26 days after the SNI or sham surgery. Two types of behavioral tests were carried out to examine their mechanical sensitivity after nerve injury. On one hand, I measured the 50% paw withdraw threshold after stimulating the glabrous skin of the hindpaw using von Frey filament--a thin filament with calibrated force (Figure 6.4C-D and 6.4G-H). Neither the dorsal column lesion nor the spinal cord hemisection changed the paw withdrawal threshold compared to the sham control group, which may reflect redundancy of the two ascending pathways in the detection of touch stimuli. After SNI, the control group without lesions are hypersensitive to von Frey indentation, which is revealed by a reduction of their withdraw thresholds on the ipsilateral side of SNI but not on the contralateral side (Figure 6.4C-D and 6.4G-H). This hypersensitivity is fully abolished in the DC lesion group, and the von Frey threshold is back to the level observed in sham mice without SNI (Figure 6.4C). In contrast, the spinal cord hemisection group, in which the ALT is disrupted, still developed mechanical hypersensitivity after SNI and is comparable to the group without spinal cord lesion (Figure 6.4G). This result suggests that the DC pathway, but not the ALT, is required for the development

of mechanical hypersensitivity after SNI, which is consistent with a previous lesion study in rats (Ossipov et al., 2002; Sun et al., 2001).

I also used a dynamic touch assay to examine mechanical allodynia (Figure 6.4A-B and 6.4E-F). In the dynamic touch assay, gentle stroking is applied across the lateral side of the hindpaw using a soft paintbrush, and the behavior response is quantified based on a well-established allodynia scoring system (Duan et al., 2014). Normally, a naïve mouse does not respond, or it only makes a quick paw withdrawal for less than one second following gentle stroking, which would be scored as zero, as shown in the sham group without SNI. After SNI, mice developed mechanical allodynia in response to gentle brushing, including either a sustained withdrawal that is scored as 1, a lateral kicking of the hind paw that is scored as 2, or paw flinching or licking that is scored as 3. A higher score indicates more severe mechanical allodynia, as shown in the SNI group. Mice without the spinal cord lesion developed a strong allodynia behavior after SNI in response to gentle brushing (Figure 6.4A and 6.4E). A similar allodynia behavior was found in the spinal cord hemisection group (Figure 6.4E). In contrast, the DC lesion group did not develop mechanical allodynia following SNI (Figure 6.4A). This result further supports the idea that the DC pathway is required for the development of peripheral neuropathic pain.

6.2. PSDC neurons are required for the development of peripheral neuropathic pain after SNI

Next we sought to determine which components of the dorsal column pathway are required for the development of peripheral neuropathic pain. Both the somatosensory ascending pathways and the descending corticospinal tracts (CSTs) travel through the dorsal column. In this section, I will focus on testing the necessity and sufficiency of the PSDC indirect pathway in the development

of peripheral neuropathic pain, though the contribution of the direct Aβ-LTMRs ascending pathway and the descending CST modulation could not be excluded.

In order to specifically manipulate the activity of PSDC neurons, I developed an intersectional genetic strategy utilizing two orthogonal recombinase systems, with Cre and Flpase. AAV2/1-Flpo fas injected to the DC at the C1-C2 level to infect neurons projecting to the DCN, including both the direct and indirect pathways. In order to restrict the labeling to the indirect pathway, I utilized *Lbx1-Cre* mice in which Cre expression is restricted to a large population of spinal cord dorsal horn neuron and some brainstem populations (Gross et al., 2002). To confirm the expression pattern of *Lbx1-Cre*, I crossed mice with the $Tau^{LSL\text{-}LacZ}$ reporter mice to label the neurons from the $Lbx1^{+}$ lineage with a lacZ reporter, and injected CTB-488 into the rostral DC to label PSDC neurons. Indeed, the majority of CTB-488^{+} PSDC neurons are β-Gal^{+} (96.4 ± 2.2%, N=3), while none of the DRG neurons are labeled by β-Gal (data not shown), indicating the *Lbx1-Cre* mice can be used as a spinal cord Cre line to label PSDC neurons. To silence PSDC neurons, I utilized a dual recombinase dependent tetanus toxin line, *RC::PF-Tox* mice, to silence the synaptic output from neurons that express both Cre and Flpase. The labeling specificity and efficiency of the PSDC neurons was examined using a similar dual recombinase reporter line, *RC::FrePe*, which express GFP in Cre^{+} and Flp^{+} neurons and express mCherry in neurons that are only Flp^{+}. The GFP^{+} neurons labeled with this intersectional strategy are located in deep spinal cord dorsal horn within lamina III-IV (Figure 6.5C) and are excluded from higher brain region including cortex (Figure 6.5D), midbrain (Figure 6.5E), and brainstem (Figure 6.5F). Further characterization using CTB injection into the C3 DC revealed that 56 ± 12% of CTB^{+} PSDC neurons are GFP^{+} (n = 4), while 56 ± 5% of GFP^{+} neurons are CTB^{+} (n = 4) (Figure 6.5C), suggesting that the intersectional genetic strategy specifically labels a majority of PSDC neurons.

Four to five weeks after the AAV2/1-Flpo injection, I examined the behavior of PSDC neuron silenced mice. There was no difference between the PSDC silencing group and control group on the rotarod test and wire hang test, suggesting normal general motor function after silencing the PSDC neurons (Figure 6.6A-B). There were also no differences of the thermal threshold measured by Hargreaves or hot/cold plate (Figure 6.7E-I), nor the tactile threshold measured by von Frey filament (glabrous skin) or tactile PPI (hairy skin) (Figure 6.7C-D and 6.6C-F), suggesting that PSDC neurons are not required for thermal or general tactile detection, or that their functions can be compensated for by alternative pathways. Interestingly, after SNI, while the control group developed mechanical hypersensitivity in the von Frey test, the PSDC-silenced mice have a von Frey threshold close to the sham group without SNI surgery (Figure 6.7C-D). Similar results were found using the dynamic brush test, in which mechanical allodynia induced by the SNI was fully abolished in the PSDC-silenced mice (Figure 6.7A-B). Together, these results suggest that the indirect DC pathway from the PSDC neurons is required for the development peripheral neuropathic pain under the SNI model.

6.3. The function of Aβ-LTMRs in the peripheral neuropathic pain

Silencing experiments have suggested that PSDC neurons, which ascend through the DC pathway, are both necessary to induce mechanical hypersensitivity and allodynia. But what is the sensory input to the PSDC neurons? And does those inputs changes after the development of peripheral neuropathy? To address these questions, I examined the primary sensory inputs for peripheral neuropathic pain, which mediate mechanical stimuli detection.

It has been shown that ablation of Nav1.8^{+} nociceptors does not affect mechanical hypersensitivity after spinal nerve ligation (SNL), which is another animal model for the peripheral neuropathic pain (Abrahamsen et al., 2008). Recently, indirect evidence has suggested an involvement of Aβ-LTMRs in the development of mechanical hypersensitivity following

peripheral neuropathy (Abrahamsen et al., 2008; Campbell et al., 1988; Xu et al., 2015; Yamamoto et al., 2008). In order to directly examine the role of Aβ-LTMRs in peripheral neuropathic pain, I designed intersectional genetic strategies to specifically silence or ablate Aβ-LTMRs and examine the behavior response after SNI. Since the majority of Aβ-LTMRs project directly to the DCN, I inject AAV2/1-Cre virus to the DC at C1-C2 level to infect the DCN projecting neurons, including Aβ-LTMRs. I further crossed in Advillin-Flpo mice, which specifically labels the majority of primary somatosensory neurons (Figure 6.8), thus only DCN projecting Aβ-LTMRs will express both Cre and Flp. In order to examine the function of Aβ-LTMRs in the neuropathic pain, I silenced those neurons using the dual recombinase dependent tetanus toxin line, the *RC::PF-Tox*. There was no difference between the Aβ-LTMR silencing group and control group on the rotarod test and wire hang test, suggesting normal general motor function after silencing the Aβ-LTMRs (Figure 6.9A-B).

Preliminary results suggest that there is no change in response to von Frey indentation or brush stroking after Aβ-LTMR ablation (Figure 6.10A-B). There is also no difference in tactile PPI test between the Aβ-LTMR ablation and control groups (Figure 6.9C-F). Together, these results suggest that ablation of DC projecting Aβ-LTMR does not change the response to low threshold mechanical stimulation in either glabrous skin or hairy skin. This is possibly due to 1) inefficient labeling using virus retrograde tracing; 2) non-DC projecting Aβ-LTMRs that are spared by the retrograde labeling strategy; 3) other LTMR subtypes which may have a compensation effect. What's more, we didn't observe a difference between silencing group and control group on the hot/cold plate (Figure 6.10C-D). However, there is a slightly increase of the withdraw latency in the Hargreaves test (Figure 6.10F). It is still unclear whether DC projecting Aβ-LTMRs are involved in thermal pain or not. These behavioral experiments need to be further repeated and histology experiments are required to examine the labeling specificity and efficiency.

I also tested behavioral responses after SNI using Aβ-LTMR silencing mice. Interestingly, preliminary result showed that mechanical hypersensitivity is reduced in the Aβ-LTMR silencing group, which was revealed by measuring the von Frey withdraw threshold (Figure 6.10A). On the other hand, mechanical allodynia induced by SNI was also reduced in the Aβ-LTMR ablation group, which was tested using the dynamic brush stroking assay (Figure 6.10B). These preliminary findings suggest that the Aβ-LTMRs, but not nociceptors, are required for development of mechanical hypersensitivity and allodynia after SNI.

If Aβ-LTMRs are required for the development of peripheral neuropathic pain, one may predict that specific activation of Aβ-LTMRs may induce pain after SNI, which may represent a nocifensive response in mice. To further test the contribution of Aβ-LTMRs in peripheral neuropathic pain, I designed an intersectional optogenetic experiment to specifically activate Aβ-LTMRs before and after the SNI. Here I utilized a dual recombinase dependent ReaChR mouse line, $R26^{LSL\text{-}FSF\text{-}ReaChr\text{-}mCitrien}$, which express a red-shifted variant of channelrhodopsin and mCitrin reporter under the control of both Cre and Flpase. Similar to the Aβ-LTMR ablation experiments, I injected AAV2/1-Cre into the rostral DC of the $Advillin^{Flpo}$, $R26^{LSL\text{-}FSF\text{-}ReaChr\text{-}mCitrin}$ mice at P13, thus ReaChR and mCitrine are specifically expressed in the DC projecting Aβ-LTMRs.

Histological experiments revealed that in DRG, the mCitrine$^+$ neurons are large diameter and myelinated (NFH$^+$), and majority of them are CGRP$^-$ (Figure 6.11B). DC injection of CTB-555 also confirmed that those mCitrine$^+$ neurons project to the DCN (Figure 6.11B). In spinal cord, mCitrine$^+$ neurons project to the deep laminae of dorsal horn and intermediate zone of spinal cord (Figure 6.11A), which is consistent with the projection patterns of Aβ-LTMRs and proprioceptors, further confirm the intersectional genetic strategy specifically labels Aβ-LTMRs. In the glabrous skin, the mCitrine$^+$ axons innervate Merkel cells and Meissner's corpuscles, as well as a small percentage of muscle spindles (Figure 6.12A-B and 6.12D), suggesting that at

least Aβ SA1-LTMRs, Aβ RA1-LTMRs, and proprioceptors are labeled. Interestingly, mCitrine^{+} axons also form free nerve endings that are weakly NFH^{+} (Figure 6.12C and 6.13A). Further genetic experiments and histology reveals that those DC retrogradely labeled free nerve endings are TrkC^{+}, CGRP^{-}, and IB4^{-} (Figure 6.13A-C), suggesting it belongs to a unique population that is distinct from the classical peptidergic and non-peptidergic nociceptors.

6 weeks after the virus injection, I delivered blue light (473nm wavelength) to the hindpaw glabrous skin and examined the behavior response (Figure 6.14A). Mice expressing ReaChR in Aβ-LTMRs exhibited a quick withdrawal, similar to the response induced by the gentle brush stroking. In contrast, control mice which did not express ReaChR did not have any response to the light, suggesting that the withdrawal response is not induced by heating from the laser or the visual cue (data not shown). Next, I carried out the same test after SNI surgery. Interestingly, mice expressing ReaChR in Aβ-LTMRs developed a nocifensive behavior in response to the same light stimulation, including lateral kicking, flinching, and licking of the paw. These behavior responses were quantified using the allodynia scoring system, which was used in the dynamic brush assay, and I found that the light induced behavioral response was similar to the response induced by gentle stroking of paintbrush. Taken together, our results suggest that Aβ-LTMRs, but not nociceptors, are both necessary and sufficient for the development of peripheral neuropathic pain under the SNI model.

6.4. PSDC neurons receive inputs from Aβ-LTMRs

So far I've found that the PSDC neurons, which ascend through the DC pathway, are both necessary and sufficient to induce mechanical hypersensitivity/allodynia following peripheral neuropathy. For the sensory neurons, I found that Aβ-LTMRs, but not nociceptors, are both necessary and sufficient for development of mechanical allodynia under peripheral neuropathic pain conditions. Unfortunately, due to technical issues, it is difficult to directly examine the

contribution of the DC projections versus the spinal cord projections from Aβ-LTMRs. However, since both PSDC neurons and Aβ-LTMRs are necessary to induce mechanical allodynia under peripheral neuropathy, and histological analysis revealed that spinal cord collaterals of Aβ-LTMRs are closely adjacent of the PSDC neurons (Figure 5.4B and 5.4D-E), we hypothesized that Aβ-LTMRs are required for allodynia development through interaction with PSDC neurons.

Indeed, histological analysis revealed that at least subsets of Aβ-LTMRs form synaptic boutons onto PSDC neurons (Figure 6.15A-C). PSDC neurons were retrogradely labeled by Rabies-ΔG-GFP injected into the caudal gracile nuclei of the DCN, while the synaptic terminals of Aβ RA-LTMRs were labeled by $R26^{LSL\text{-}Syn\text{-}tdTomato}$ *(Ai34)* crossed with Ret^{CreER}, an Aβ RA-LTMR specific CreER line. The synaptic boutons were further confirmed by staining using a postsynaptic marker, Homer1. The synaptic connections between Aβ RA-LTMRs and PSDC neurons was also examined by spinal cord slice physiological recordings, which were done by Anda Chirila, a postdoc in the lab. Using Ret^{CreER}; $R26^{LSL\text{-}ChR2\text{-}YFP}$ *(Ai32)* mice, we found that PSDC neurons received strong excitatory input after light activation of Aβ RA-LTMRs, which is revealed as an inward current when the PSDC neuron is held at -60mV. This inward current is fully blocked by NBQX, the AMPA receptor antagonist. Thus both histological and physiological results have suggested that PSDC neurons receive excitatory input from Aβ-LTMRs. We are currently examining whether this connection undergoes changes after SNI.

In summary, I have shown that after SNI, it is the DC pathway, not the ALT pathway, that is required for development of peripheral neuropathic pain, including mechanical hypersensitivity and allodynia. I've also demonstrated that PSDC neurons, which constitute the indirect dorsal column pathway, are required for mechanical hypersensitivity/allodynia under SNI, and activation of PSDC neurons evokes a behavioral phenotype that resembles peripheral neuropathy. We've further shown that PSDC neurons receive synaptic inputs from Aβ-LTMRs,

which are also required for mechanical hypersensitivity/allodynia development under peripheral neuropathic pain conditions. Our findings suggest a novel ascending pathway underlies the development of peripheral neuropathy, which may help us understand its mechanism and developing pharmaceutical treatments.

Figure 6.1 Histology confirms that the DCN innervation of Aβ LTMRs is abolished following DC lesion.

(A-C) Immunostaining of GFP and vGlut1 on brainstem sections (100 μm in thickness) of *Advillin*^{Flpo}*; R26*$^{FSF\text{-}GFP}$ reveal the sensory innervation of the dorsal column nuclei (labeled by red dashed lines) after sham surgery (A), DC lesion (B), and hemisection of the left side of spinal cord (C). The DCN innervation from GFP^{+} sensory neurons is fully abolished after the DC lesion (B) compared to sham control and spinal cord hemisection (A and C).

Scale bar: 800 μm (A-C).

Figure 6.1

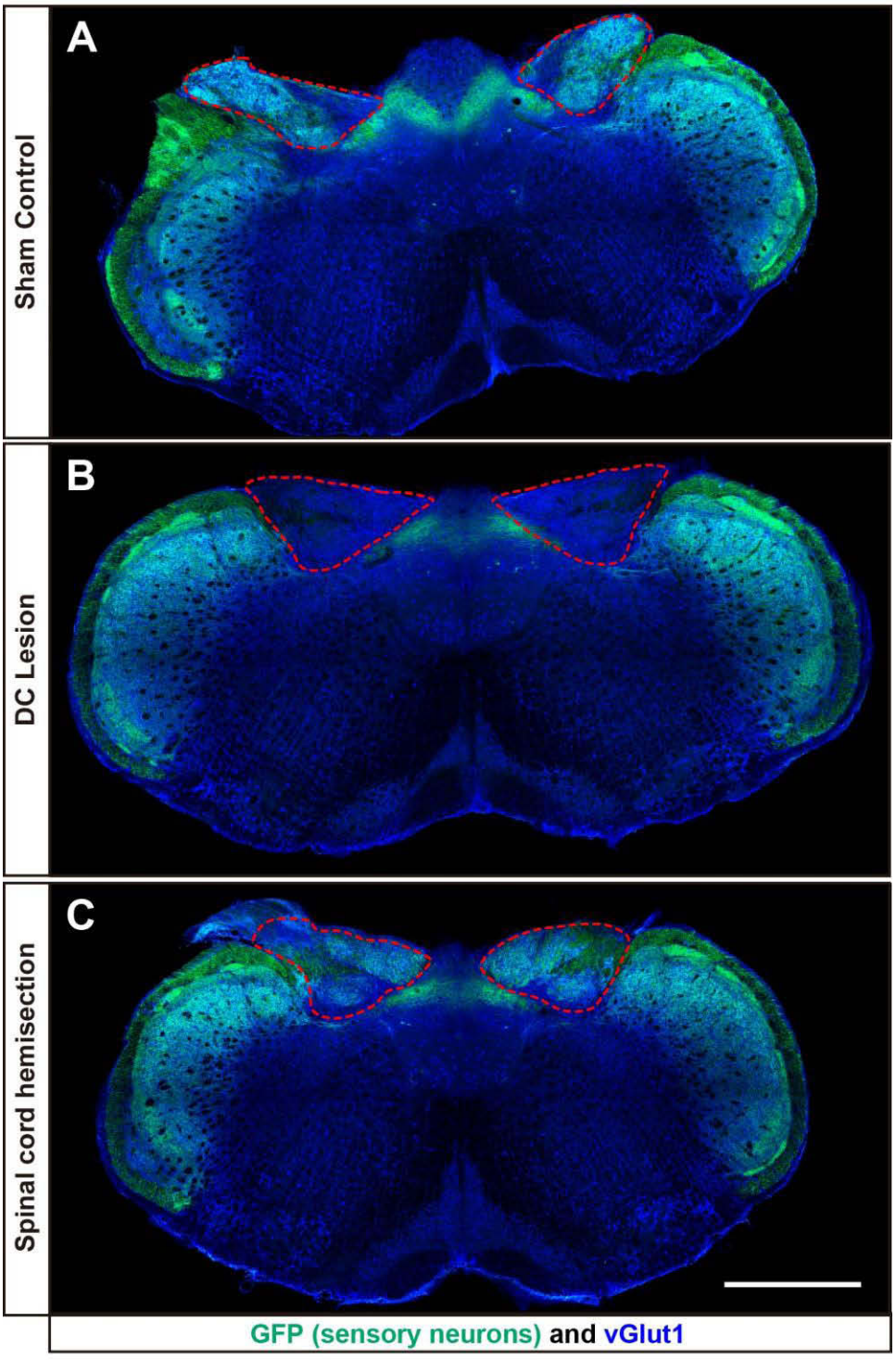
A
Sham Control
B
DC Lesion
C
Spinal cord hemisection
GFP (sensory neurons) and vGlut1

Figure 6.2 DC lesion doesn't affect motor function or innocuous touch sensitivity.

(A-F) Motor coordination tests and tactile tests reveal no difference between the DC lesioned mice and sham control mice. (Welch's t-test for A, C, and D; Two-way ANOVA for B, D and F).

(A-B) Latency to fall during the wire hang test (A) or rotarod test (B).

(C) Response to an 80-dB acoustic noise (50 ms) in DC lesioned mice and sham control mice.

(D) Percentage inhibition of the startle response to a 125-dB noise (pulse), when the startle noise was preceded by a weaker acoustic noise at different intensities (PP3 at 68 dB, PP6 at 71 dB, PP9 at 74 dB, PP12 at 77 dB, and PP15 at 80 dB)

(E) Response to a light air puff (0.9 PSI, 50ms) applied to the back hairy skin.

(F) Percentage inhibition of the startle response to a 125-dB noise (pulse), when the startle noise was preceded by a light air puff (prepulse, 0.9 PSI) at multiple inter-stimulus intervals (ISIs) between the prepulse and the pulse.

Figure 6.2

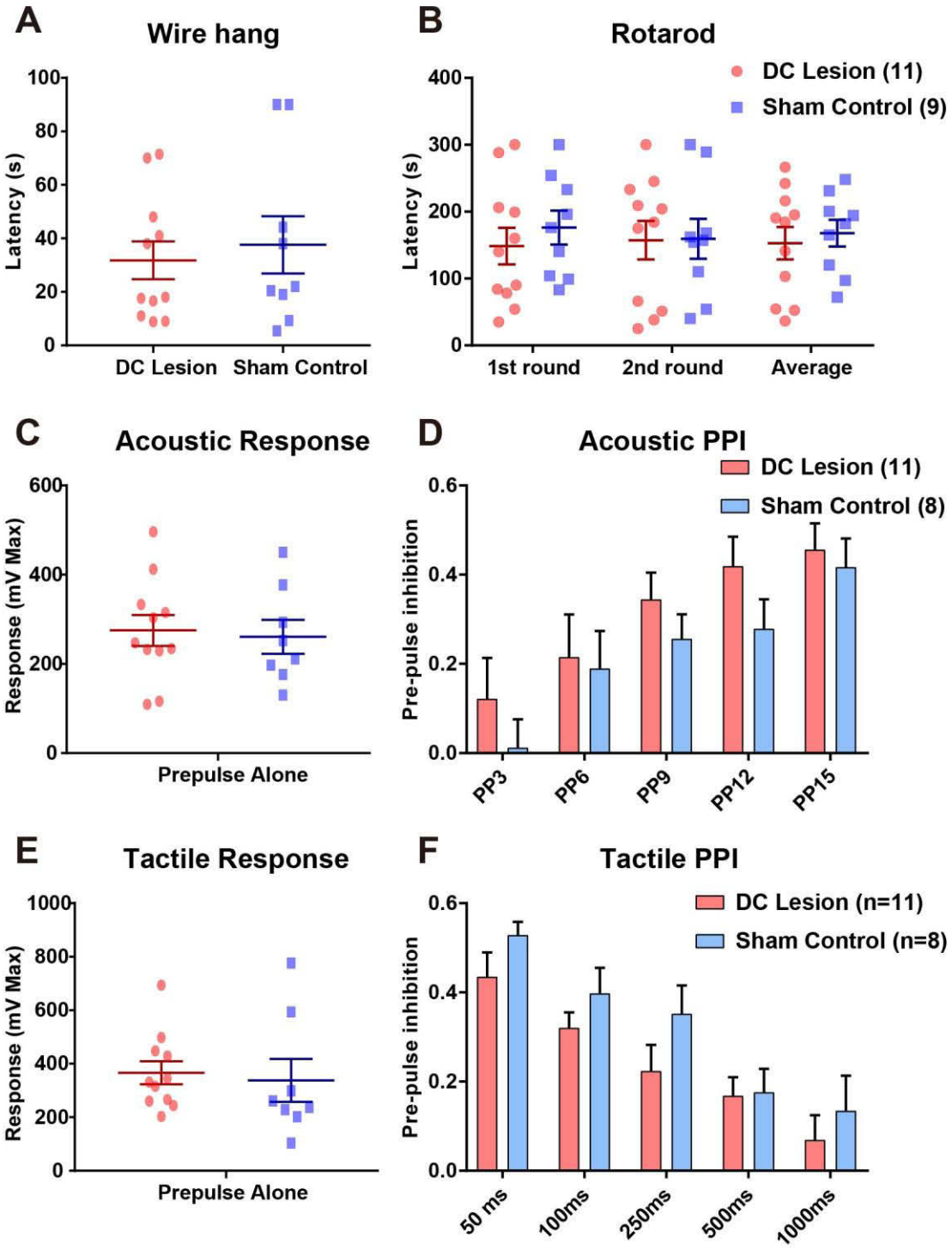
A
Wire hang
Latency (s)
100
80
60
40
20
0
DC Lesion
Sham Control
B
Rotarod
DC Lesion (11)
Sham Control (9)
Latency (s)
400
300
200
100
0
1st round
2nd round
Average
C
Acoustic Response
Response (mV Max)
600
400
200
0
Prepulse Alone
D
Acoustic PPI
DC Lesion (11)
Sham Control (8)
Pre-pulse inhibition
0.6
0.4
0.2
0.0
PP3
PP6
PP9
PP12
PP15
E
Tactile Response
Response (mV Max)
1000
800
600
400
200
0
Prepulse Alone
F
Tactile PPI
DC Lesion (n=11)
Sham Control (n=8)
Pre-pulse inhibition
0.6
0.4
0.2
0.0
50 ms
100ms
250ms
500ms
1000ms

Figure 6.3 Thermal and Capsaicin test after the lesion of DC and ALT.

(A-C) Latency of responses measured by hot/cold plate assay show there are no differences between the sham control mice, DC lesioned mice, and left spinal cord hemisected mice in thermal pain sensation (two-way ANOVA).

(D) Latency of response measured by Hargreaves assay shows there is an increased latency to respond to the stimulus in the right hindpaw of left spinal cord hemisected mice. (Two-way ANOVA: $p = 0.0003$, $F[2,20] = 12.66$, post hoc Sidak's test: ****$p < 0.0001$)

(E) Time spent licking the paw after a 5μg Capsaicin intraplantar injection shows no differences between sham control and spinal cord hemisected mice (two-way ANOVA). Note the n number is low for both groups.

Figure 6.3

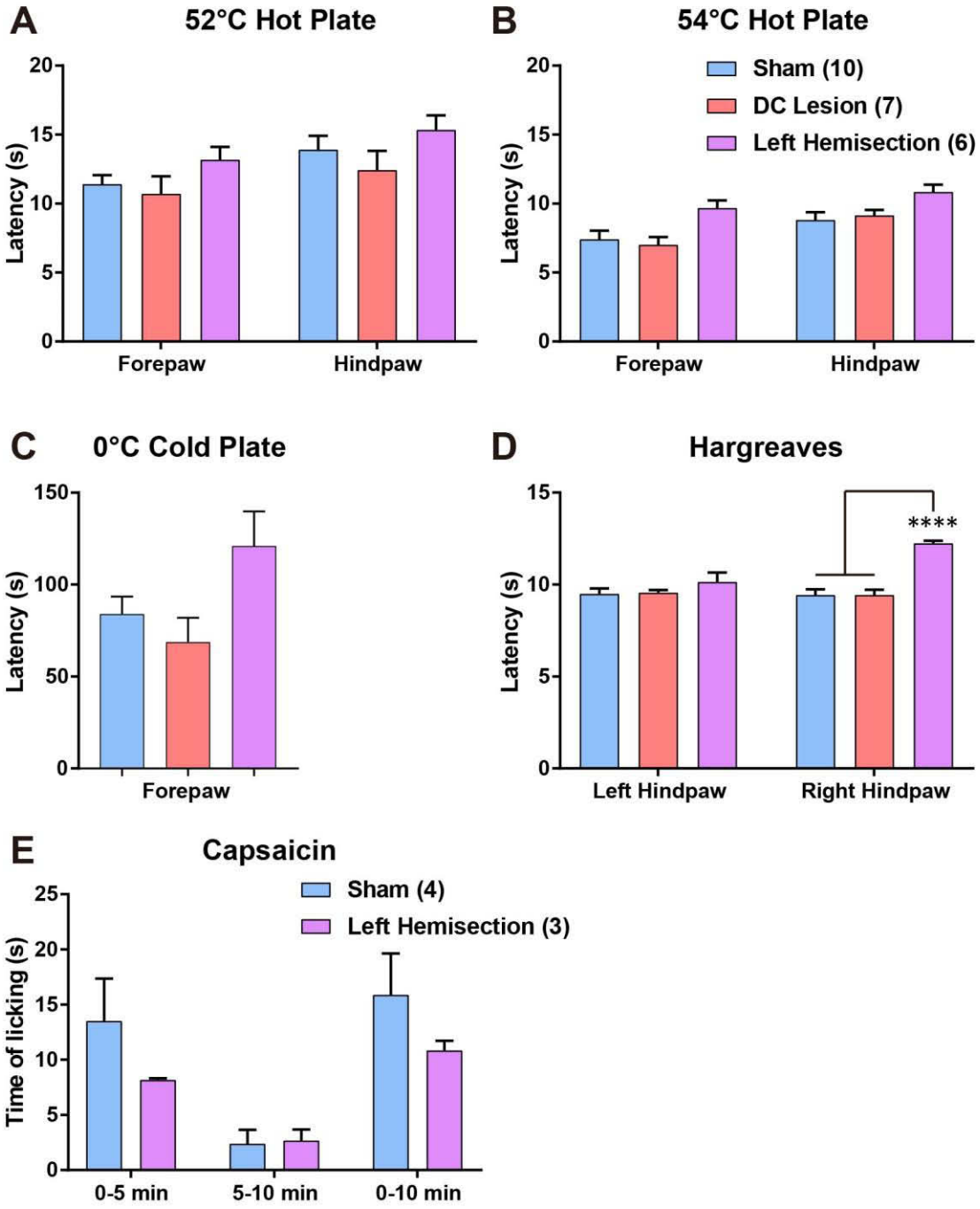
A
52°C Hot Plate
Latency (s)
20
15
10
5
0
Forepaw
Hindpaw
B
54°C Hot Plate
Sham (10)
DC Lesion (7)
Left Hemisection (6)
Latency (s)
20
15
10
5
0
Forepaw
Hindpaw
C
0°C Cold Plate
Latency (s)
150
100
50
0
Forepaw
D
Hargreaves
Latency (s)
15
10
5
0
****
Left Hindpaw
Right Hindpaw
E
Capsaicin
Sham (4)
Left Hemisection (3)
Time of licking (s)
25
20
15
10
5
0
0-5 min
5-10 min
0-10 min

Figure 6.4 Disruption of DC, but not ALT, abolished the mechanical allodynia/hypersensitivity phenotype following SNI.

(A-B) Allodynia score measured by brush assay reveals that mechanical allodynia is developed only in the ipsilateral paw of the control SNI group, which receives SNI after sham spinal cord surgery (****$p < 0.0001$ compared to the other three groups). (A) Two-way ANOVA: $p < 0.0001$, $F[3, 39] = 230.9$. Post hoc Tukey's test: ****$p < 0.0001$.

(C-D) Fifty percent paw withdrawal threshold measured by von Frey assay reveals that mechanical sensitivity is increased on the ipsilateral paw of the control SNI group (*$p < 0.05$ or **$p < 0.01$ compared to the other three groups). (C) Two-way ANOVA: $p = 0.0028$, $F[3,39] = 5.56$. Post hoc Turkey's test: *$p < 0.05$ or **$p < 0.01$.

(E-F) Allodynia score measured by brush assay reveals that mechanical allodynia is developed in the ipsilateral paw of both control SNI group and hemisected SNI group compared to other Sham group without SNI (****$p < 0.0001$). (E) Two-way ANOVA: $p < 0.0001$, $F[3, 53] = 83.78$. Post hoc Tukey's test: ****$p < 0.0001$.

(G-H) 50% paw withdrawal threshold measured by von Frey assay reveals that mechanical sensitivity is increased in the ipsilateral paw of both control SNI group and hemisected SNI group compared to other sham group (****$p < 0.0001$). (G) Two-way ANOVA: $p < 0.0001$, $F[3,53] = 28.25$. Post hoc Turkey's test: ****$p < 0.0001$.

Figure 6.4

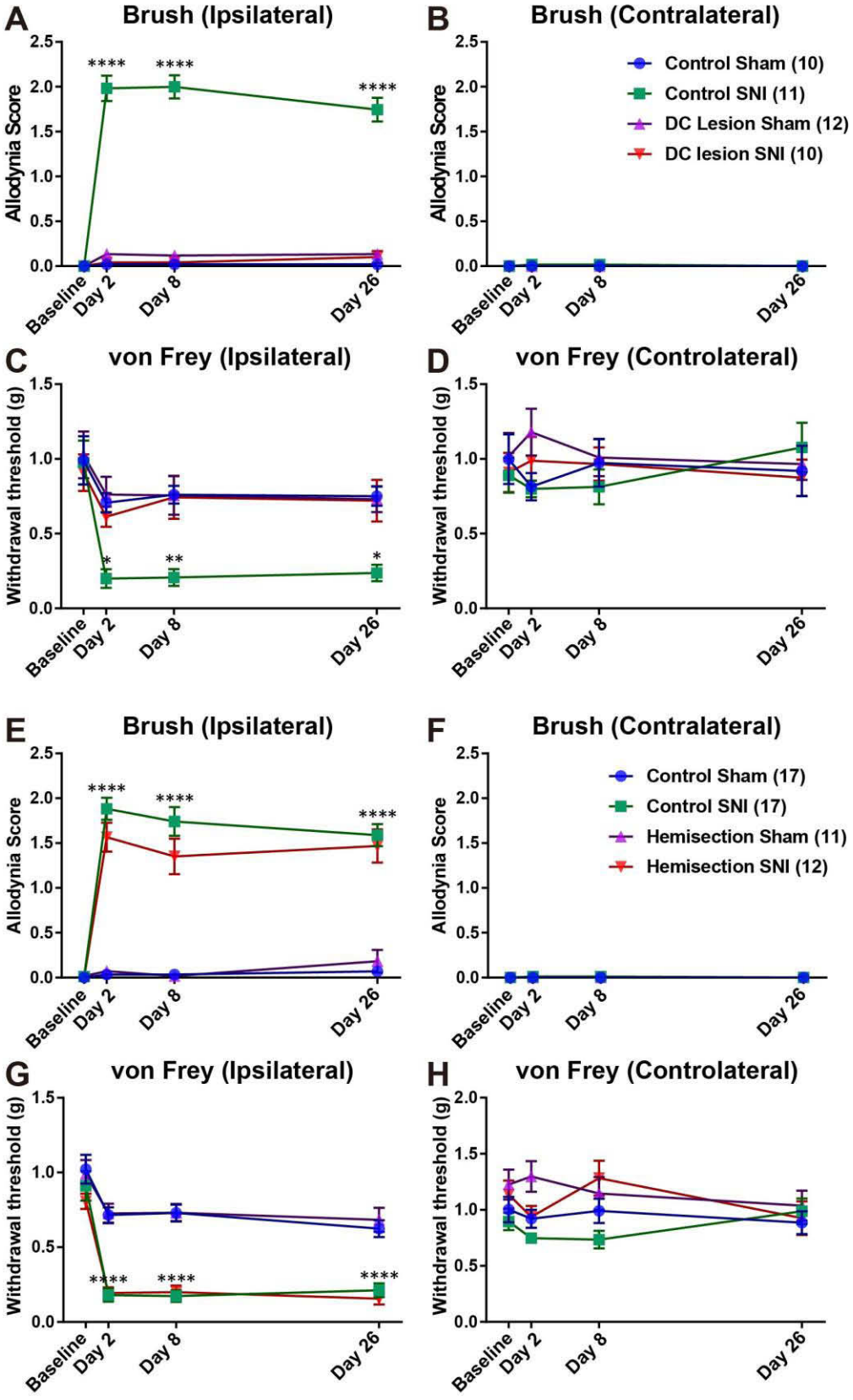
A
Brush (Ipsilateral)
Allodynia Score
B
Brush (Contralateral)
Control Sham (10)
Control SNI (11)
DC Lesion Sham (12)
DC lesion SNI (10)
C
von Frey (Ipsilateral)
Withdrawal threshold (g)
D
von Frey (Controlateral)
E
Brush (Ipsilateral)
F
Brush (Contralateral)
Control Sham (17)
Control SNI (17)
Hemisection Sham (11)
Hemisection SNI (12)
G
von Frey (Ipsilateral)
H
von Frey (Controlateral)
Baseline
Day 2
Day 8
Day 26

Figure 6.5 Intersectional genetic strategy specifically labels PSDC neurons.

(A) Sagittal spinal cord sections from *Lbx1*^{Cre}*; Tau*$^{LSL\text{-}lacZ}$ mice after CTB-488 C1 DC injection shows that the vast majority of CTB-488^{+} PSDC neurons are βGal^{+} (96.4 ± 2.2%, n = 3).

(B-F) Intersectional genetic strategy utilizes dual recombinase reporter *RC::FrePe* (or *RC::FP-Tox* for PSDC silencing experiments in Figure 6.6 and 6.7), *Lbx1*^{Cre} and AAV2/1-Flpo C1 DC injection to specifically label PSDC neurons, as shown in the schematic (B). (C) Spinal cord transverse section shows the GFP+ neurons are partially overlapping with neurons retrogradely labeled by CTB-555 DC injection: 56 ± 12% of CTB^{+} PSDC neurons are GFP^{+} (n = 4) and 56 ± 5% of GFP^{+} neurons are CTB^{+} (n = 4). (D-F) Transverse sections of the brain show that majority of labeled neurons are mCherry+ and GFP- (thus do not express the tetanus toxin) in the cortex (D), midbrain (E), and brainstem (F). Note there are some GFP+ cells sparsely distributed in the brainstem that are not specifically located in any nucleus (F).

Scale bar: 200 μm (A, C-F).

Figure 6.5

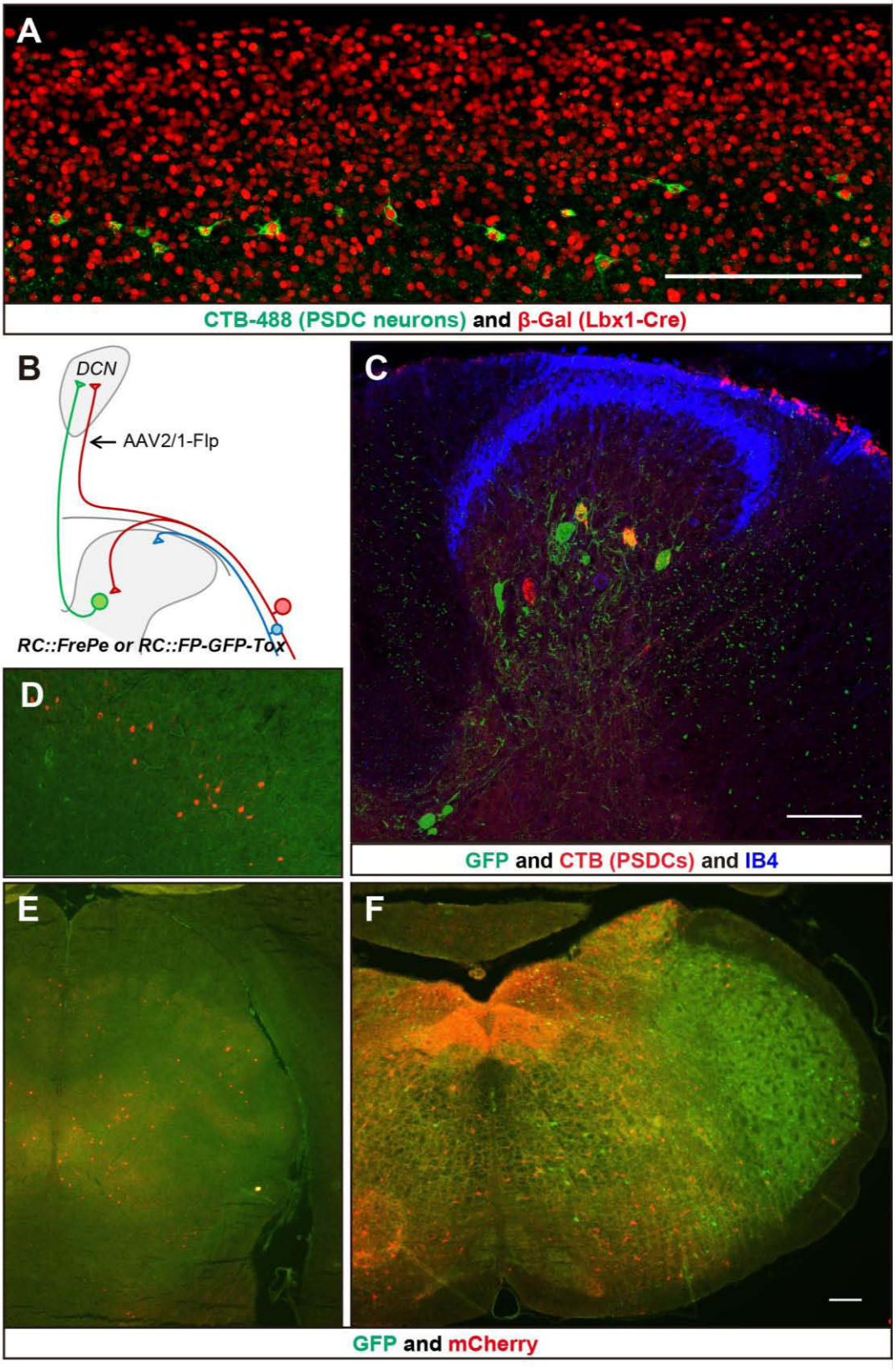
A
CTB-488 (PSDC neurons) and β-Gal (Lbx1-Cre)
B
DCN
AAV2/1-Flp
RC::FrePe or RC::FP-GFP-Tox
C
GFP and CTB (PSDCs) and IB4
D
E
F
GFP and mCherry

Figure 6.6 PSDC silencing doesn't affect motor function or innocuous touch sensitivity.

(A-F) Motor coordination tests and tactile tests reveal no abnormalities in the PSDC silencing mice. PSDC silencing group: *Lbx1^{Cre}; RC::FP-Tox* mice with AAV2/1-Flpo C1 DC injection at P14. Control group: *Lbx1^{Cre}; RC::FP-Tox* mice with AAV2/1-Cre C1 DC injection, or *RC::FP-Tox* mice with AAV2/1-Flpo C1 DC injection. (Welch's t-test for A, C, and D; Two-way ANOVA for B, D and F)

(A-B) Latency to fall during the wire hang test (A) or rotarod test (B)

(C) Response to 80-dB acoustic noise in PSDC silencing mice and control mice.

(D) Percentage inhibition of the startle response to a 125-dB noise (pulse), when the startle noise was preceded by a weaker acoustic noise at different intensities (PP3 at 68 dB, PP6 at 71 dB, PP9 at 74 dB, PP12 at 77 dB, and PP15 at 80 dB)

(E) Response to a light air puff (0.9 PSI, 50ms) applied to the back hairy skin.

(F) Percentage inhibition of the startle response to a 125-dB noise (pulse), when the startle noise was preceded by a light air puff (prepulse, 0.9 PSI) at multiple inter-stimulus intervals (ISIs) between the prepulse and the pulse.

Figure 6.6

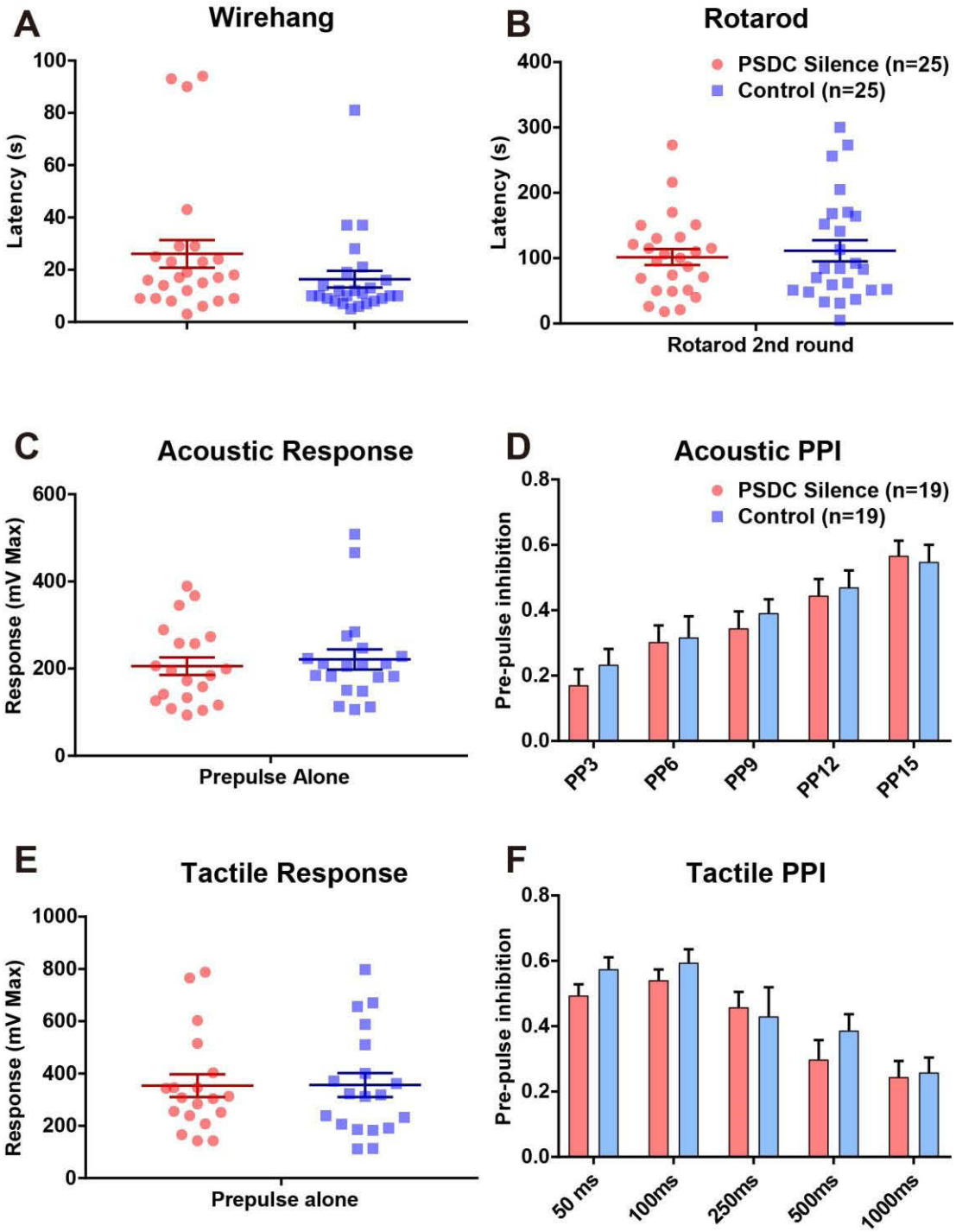
A
Wirehang
Latency (s)
100
80
60
40
20
0
B
Rotarod
PSDC Silence (n=25)
Control (n=25)
Latency (s)
400
300
200
100
0
Rotarod 2nd round
C
Acoustic Response
Response (mV Max)
600
400
200
0
Prepulse Alone
D
Acoustic PPI
PSDC Silence (n=19)
Control (n=19)
Pre-pulse inhibition
0.8
0.6
0.4
0.2
0.0
PP3
PP6
PP9
PP12
PP15
E
Tactile Response
Response (mV Max)
1000
800
600
400
200
0
Prepulse alone
F
Tactile PPI
Pre-pulse inhibition
0.8
0.6
0.4
0.2
0.0
50 ms
100ms
250ms
500ms
1000ms

Figure 6.7 PSDC silencing doesn't alter response to thermal or capsaicin-induced pain stimuli, but specifically abolishes mechanical allodynia/hypersensitivity after SNI.

(A-B) Allodynia scores as measured by the brush assay reveal that mechanical allodynia is only developed in the ipsilateral paw of the control SNI group (****$p < 0.0001$ compared to the other three groups including PSDC silencing mice with SNI). (A) Two-way ANOVA: $p < 0.0001$, $F[3, 34] = 28.48$. Post hoc Tukey's test: ****$p < 0.0001$.

(C-D) Fifty percent paw withdrawal threshold measured by the von Frey assay reveals that mechanical sensitivity is only increased on the ipsilateral paw of the control SNI group (*$p < 0.05$ or **$p < 0.01$ compared to the other three groups). (C) Two-way ANOVA: $p = 0.0018$, $F[3,34] = 6.218$. Post hoc Turkey's test: **$p < 0.01$.

(E-H) Latency of responses measured by hot/cold plate assay (E-G) and Hargreaves assay (H) show there are no differences between control mice and PSDC silencing mice in thermal pain sensation (two-way ANOVA).

(I) Time spent on licking after 5μg Capsaicin intraplantar injection shows no differences between the control mice and PSDC silencing mice (two-way ANOVA).

Figure 6.7

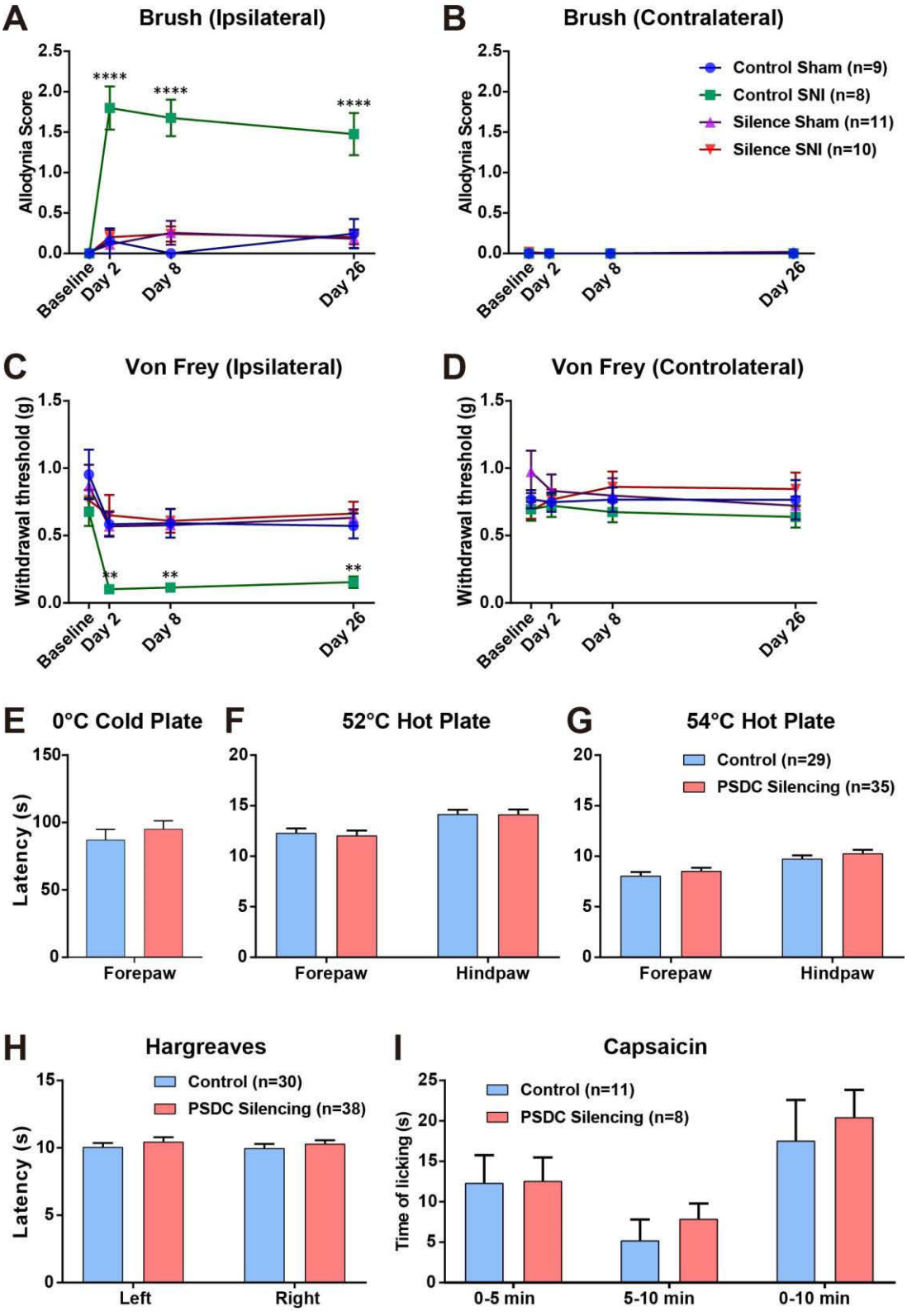
A
Brush (Ipsilateral)
Allodynia Score
2.5
2.0
1.5
1.0
0.5
0.0
****
****
****
Baseline
Day 2
Day 8
Day 26
B
Brush (Contralateral)
Allodynia Score
Control Sham (n=9)
Control SNI (n=8)
Silence Sham (n=11)
Silence SNI (n=10)
C
Von Frey (Ipsilateral)
Withdrawal threshold (g)
1.5
1.0
0.5
0.0
**
**
**
D
Von Frey (Controlateral)
Withdrawal threshold (g)
E
0°C Cold Plate
Latency (s)
150
100
50
0
Forepaw
F
52°C Hot Plate
20
15
10
5
0
Forepaw
Hindpaw
G
54°C Hot Plate
Control (n=29)
PSDC Silencing (n=35)
Forepaw
Hindpaw
H
Hargreaves
Control (n=30)
PSDC Silencing (n=38)
Latency (s)
15
10
5
0
Left
Right
I
Capsaicin
Control (n=11)
PSDC Silencing (n=8)
Time of licking (s)
25
20
15
10
5
0
0-5 min
5-10 min
0-10 min

Figure 6.8 Characterization of *Advillin*^{Flpo} line.

(A-E) Double immunostaining of mCherry with NeuN (A), NFH (B), CGRP (C), TH and IB4 (D) on adult thoracic DRG sections of *Advillin*^{Flpo}*; RC::FrePe* mice reveals that the majority of DRG neurons are labeled by *Advillin*^{Flpo}. (B) Quantifications of the percentage of each neuronal population that are labeled with mCherry.

(F) Transverse section of the spinal cord of *Advillin*^{Flpo}*; RC::FrePe* mouse shows the central projection of mCherry^{+} DRG neurons. Note there isn't non-specific labeling in the spinal cord.

(G) Transverse section of the brainstem of *Advillin*^{Flpo}*; RC::FrePe* mouse shows the DCN innervations of mCherry^{+} DRG neurons and trigeminal innervations from mCherry^{+} trigeminal ganglion neurons.

(H) Double immunostaining of mCherry and TH shows that mCherry is not expressed in TH labeled sympathetic ganglion neurons of *Advillin*^{Flpo}*; RC::FrePe* mouse.

Scale bar: 200 μm (A-G).

Figure 6.8

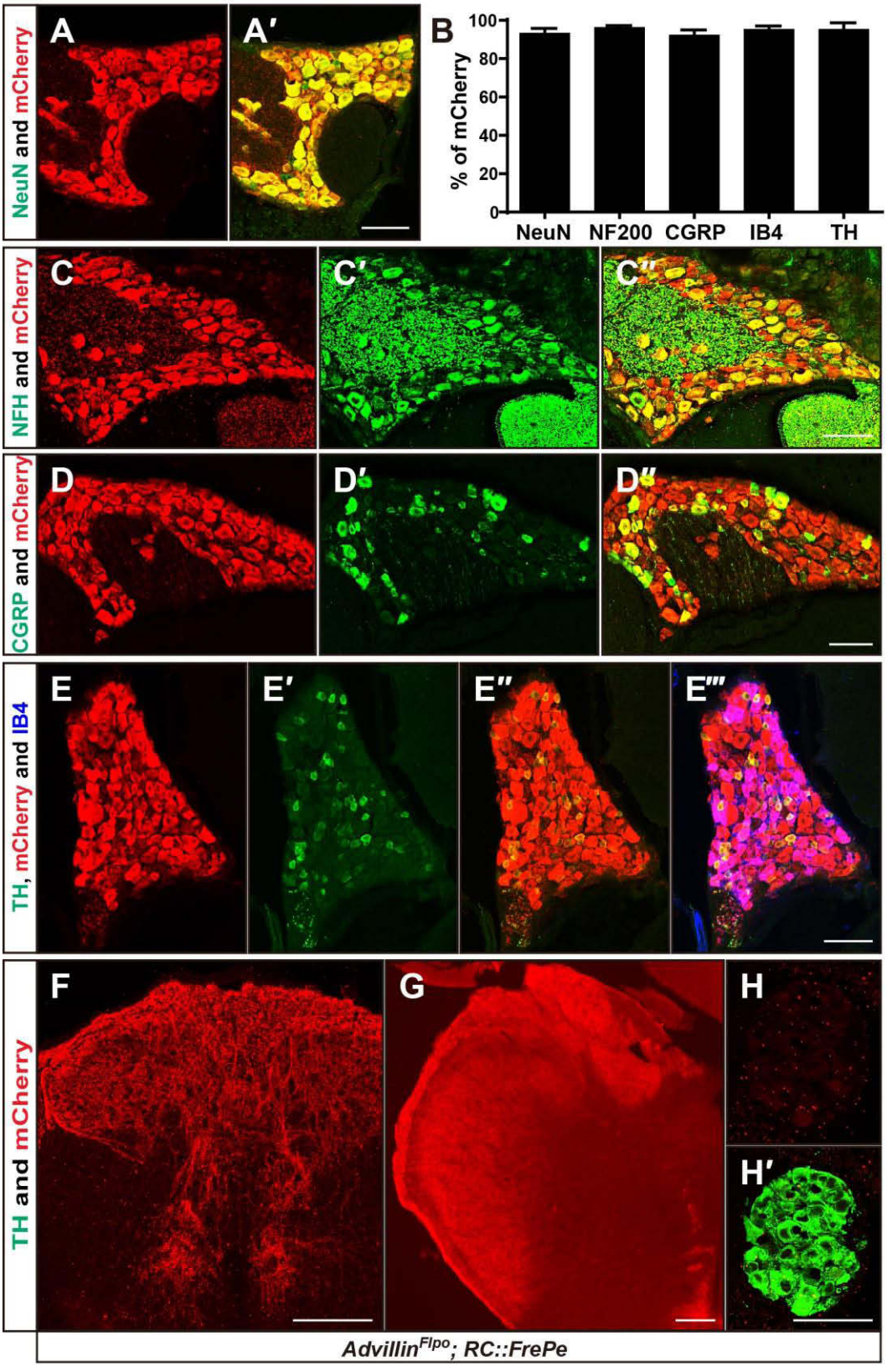
NeuN and mCherry
A
A′
B
100
80
60
40
20
0
% of mCherry
NeuN
NF200
CGRP
IB4
TH
NFH and mCherry
C
C′
C″
CGRP and mCherry
D
D′
D″
TH, mCherry and IB4
E
E′
E″
E‴
TH and mCherry
F
G
H
H′
Advillin^Flpo; RC::FrePe

Figure 6.9 Aβ-LTMR silencing doesn't change motor function and innocuous touch sensitivity.

(A-F) Motor coordination tests and tactile tests reveal no defect in the Aβ-LTMR silencing mice. Aβ-LTMR silencing group: *Advillin^{Cre}; RC::FP-Tox* mice with AAV2/1-Flpo C1 DC injection at P14. Control group: *Advillin^{Cre}; RC::FP-Tox* mice with AAV2/1-Cre C1 DC injection, or *RC::FP-Tox* mice with AAV2/1-Flpo C1 DC injection.

(A-B) Latency to fall in the wire hang test (A) or rotarod test (B)

(C) Response to 80-dB acoustic noise in PSDC silencing mice and control mice.

(D) Percentage inhibition of the startle response to a 125-dB noise (pulse), when the startle noise was preceded by a weaker acoustic noise at different intensities (PP3 at 68 dB, PP6 at 71 dB, PP9 at 74 dB, PP12 at 77 dB, and PP15 at 80 dB)

(E) Response to a light air puff (0.9 PSI, 50ms) applied to the back hairy skin.

(F) Percentage inhibition of the startle response to a 125-dB noise (pulse), when the startle noise was preceded by a light air puff (prepulse, 0.9 PSI) at multiple inter-stimulus intervals (ISIs) between the prepulse and the pulse.

Figure 6.9

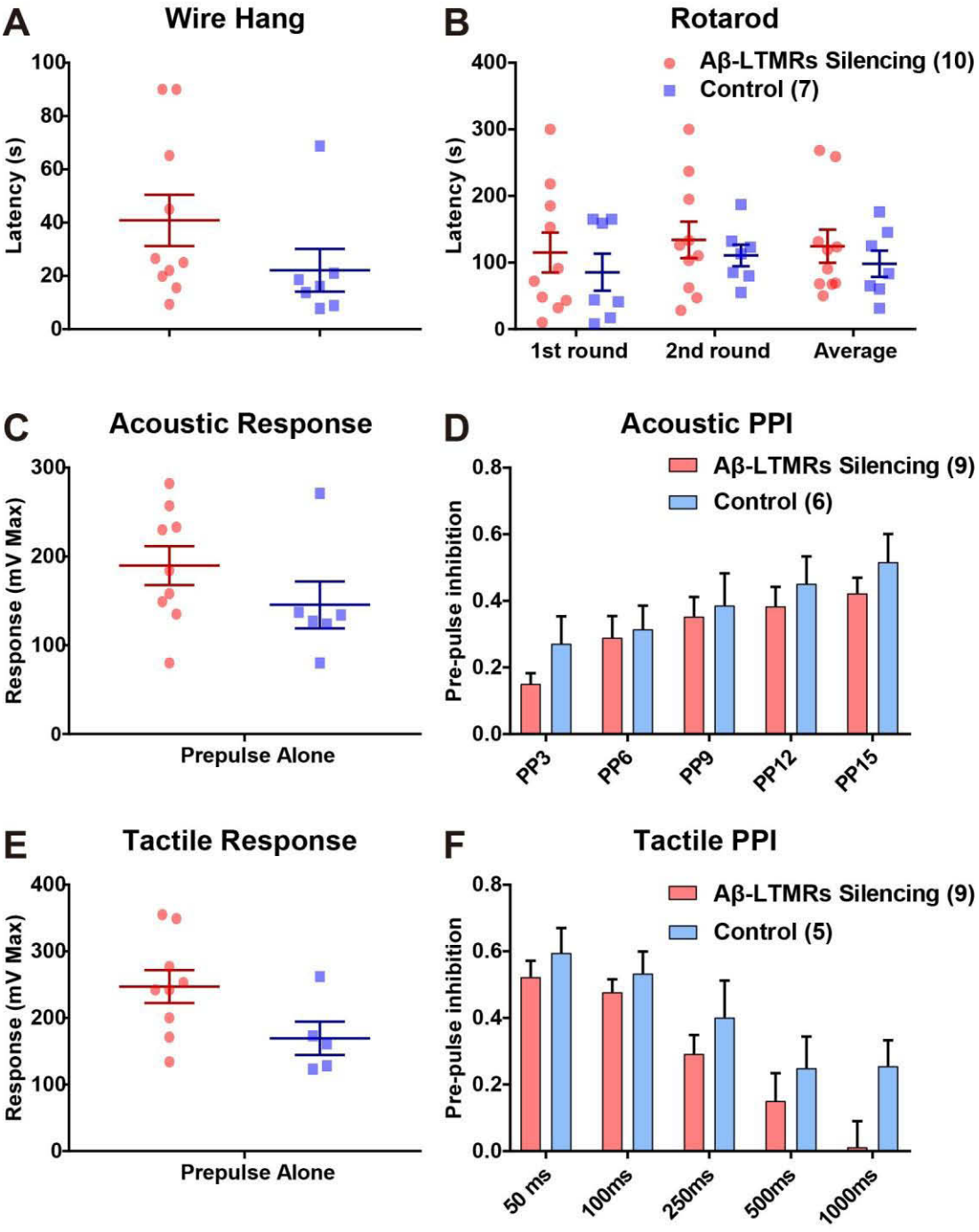
A
Wire Hang
Latency (s)
100
80
60
40
20
0
B
Rotarod
Aβ-LTMRs Silencing (10)
Control (7)
Latency (s)
400
300
200
100
0
1st round
2nd round
Average
C
Acoustic Response
Response (mV Max)
300
200
100
0
Prepulse Alone
D
Acoustic PPI
Aβ-LTMRs Silencing (9)
Control (6)
Pre-pulse inhibition
0.8
0.6
0.4
0.2
0.0
PP3
PP6
PP9
PP12
PP15
E
Tactile Response
Response (mV Max)
400
300
200
100
0
Prepulse Alone
F
Tactile PPI
Aβ-LTMRs Silencing (9)
Control (5)
Pre-pulse inhibition
0.8
0.6
0.4
0.2
0.0
50 ms
100ms
250ms
500ms
1000ms

Figure 6.10 Aβ-LTMR silencing may abolish mechanical allodynia/hypersensitivity after SNI.

(A) Fifty percent paw withdrawal threshold measured by von Frey assay reveals that mechanical hypersensitivity induced by SNI is reduced in the Aβ-LTMR silencing group (**p < 0.01). Two-way ANOVA: p = 0.0183, F[1,5] = 11.88. Post hoc Sidak's test: **p < 0.01. Note the n number is low.

(B) Allodynia score measured by brush assay reveals that mechanical allodynia induced by SNI is reduced in the Aβ-LTMR silencing group (***p < 0.01). Two-way ANOVA: p = 0.0015, F[1,7] = 25.39. Post hoc Sidak's test: ***p < 0.001. Note the n number is low.

(C-E) Latency of responses measured by the hot/cold plate assay show there are no differences between the control mice and Aβ-LTMR silencing mice in thermal pain sensitivity (two-way ANOVA).

(F) Latency of response measured by Hargreaves assay shows that there is an increase in latency to remove the right hindpaw during stimulus application of Aβ-LTMR silencing mice (p=0.001) but not the left hindpaw (p=0.062). (Two-way ANOVA: p = 0.0023, F[1,14] = 13.86, post hoc Sidak's test: **p < 0.001)

Figure 6.10

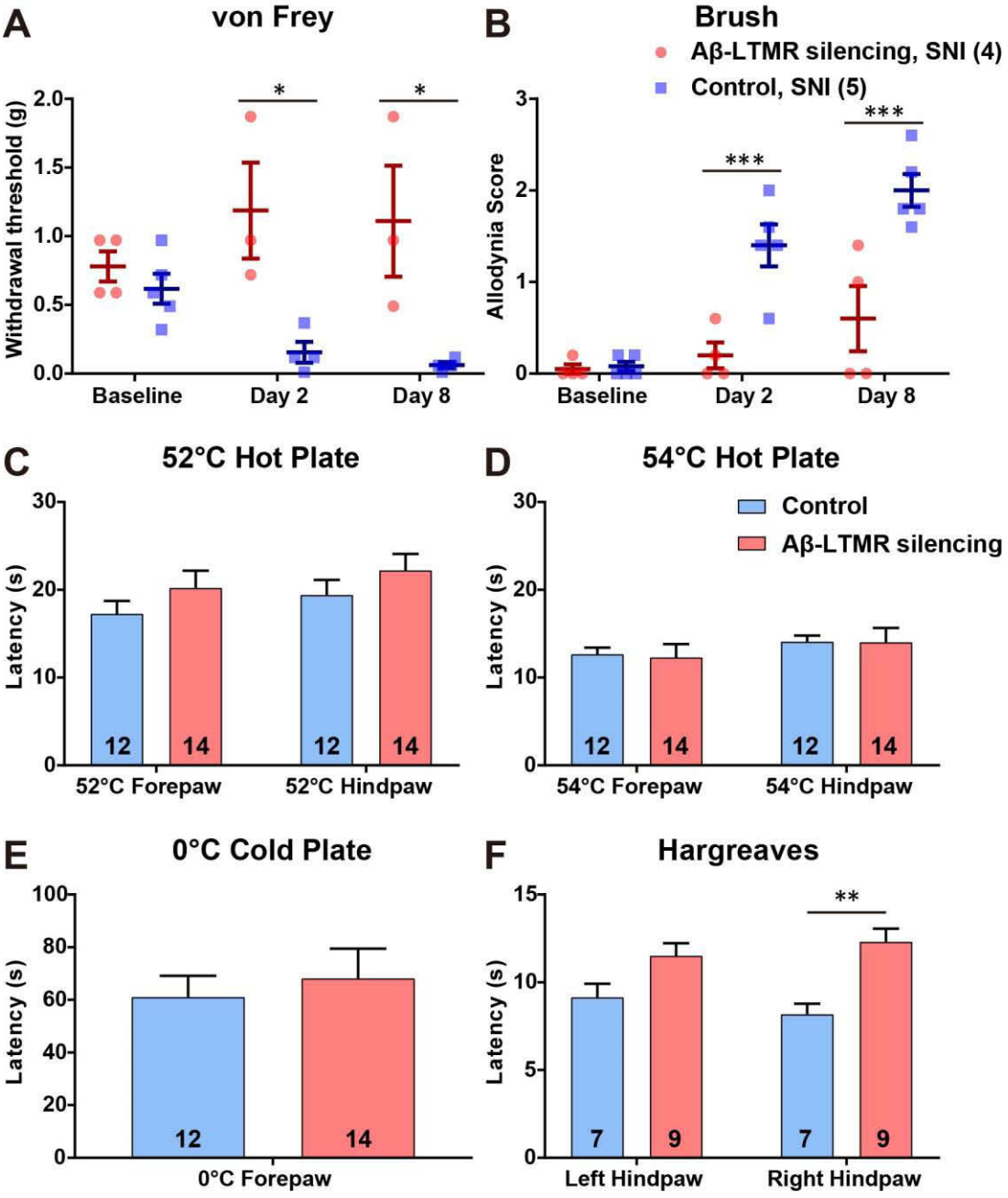
A
von Frey
Withdrawal threshold (g)
2.0
1.5
1.0
0.5
0.0
*
*
Baseline
Day 2
Day 8
B
Brush
Aβ-LTMR silencing, SNI (4)
Control, SNI (5)
Allodynia Score
3
2
1
0
***
***
Baseline
Day 2
Day 8
C
52°C Hot Plate
Latency (s)
30
20
10
0
12
14
12
14
52°C Forepaw
52°C Hindpaw
D
54°C Hot Plate
Control
Aβ-LTMR silencing
Latency (s)
30
20
10
0
12
14
12
14
54°C Forepaw
54°C Hindpaw
E
0°C Cold Plate
Latency (s)
100
80
60
40
20
0
12
14
0°C Forepaw
F
Hargreaves
Latency (s)
15
10
5
0
**
7
9
7
9
Left Hindpaw
Right Hindpaw

Figure 6.11 Assessing the expression pattern of the Aβ-LTMR ReaChR mice in DRG and spinal cord.

(A) Spinal cord transverse section of *Advillin*^{Flpo}*; R26*$^{LSL\text{-}FSF\text{-}ReaChR\text{-}mCitrine}$ mouse with AAV2/1-Cre C1 DC injection at P14. Axonal terminals from mCitrine^{+} DRG neurons innervate deep lamina of spinal cord dorsal horn that do not overlap with CGRP^{+} laminae I, but do overlap with the CTB-555^{+} PSDC neurons labeled laminae IV.

(B) Immunostaining of mCitrine, NFH, and CGRP on a DRG section of *Advillin*^{Flpo}*; R26*$^{LSL\text{-}FSF\text{-}ReaChR\text{-}mCitrine}$ mouse with AAV2/1-Cre C1 DC injection at P14. The majority of mCitrine^{+} neurons are NFH^{+} and CGRP-. Most of mCitrine^{+} neurons are also retrogradely labeled by CTB-555 which is injected to the C3 DC.

Scale bar: 200 μm (A-B).

Figure 6.11

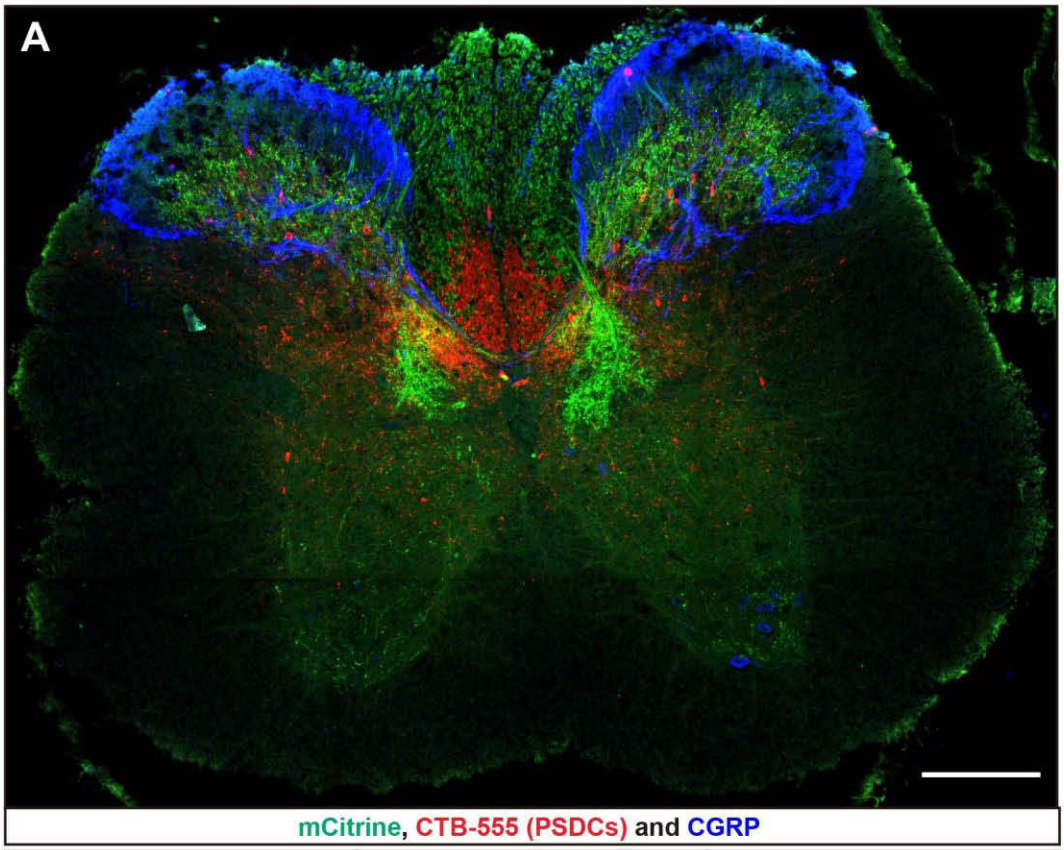
A
mCitrine, CTB-555 (PSDCs) and CGRP
B
mCitrine, NFH, CTB-555 and CGRP

Figure 6.12 Peripheral axonal terminal labelling in the Aβ-LTMR ReaChR mice.

(A-D) Cross sections of hindpaw glabrous skin (A-C) and hindpaw muscles (D) from *Advillin*^{Flpo}; *R26*$^{LSL\text{-}FSF\text{-}ReaChR\text{-}mCitrine}$ mice with AAV2/1-Cre C1 DC injection at P14 show that the peripheral axonal terminals from mCitrine^{+} DRG neurons form Merkel endings (A), Meissner's corpuscles (B), free nerve endings (C), and muscle spindles (D).

Scale bar: 100 μm (A-D).

Figure 6.12

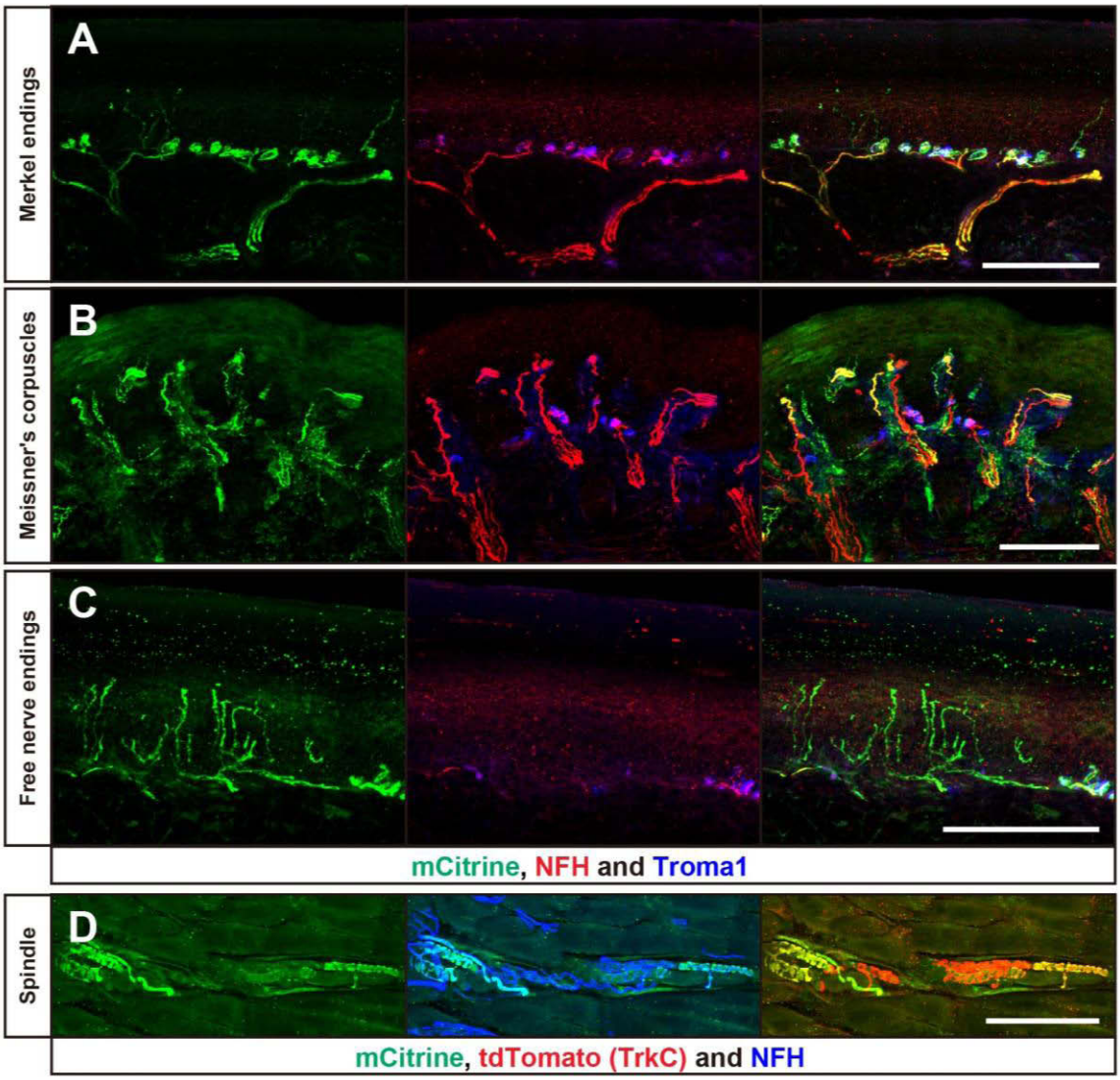
A
Merkel endings
B
Meissner's corpuscles
C
Free nerve endings
mCitrine, NFH and Troma1
D
Spindle
mCitrine, tdTomato (TrkC) and NFH

Figure 6.13 The DCN-projecting DRG neurons with free nerve endings are TrkC^{+}, CGRP^{-}, and IB4^{-}.

(A) Immunostaining of YFP, tdTomato, and NFH on hindpaw glabrous skin sections from *TrkC^{tdTomato}; R26$^{LSL\text{-}ChR2\text{-}YFP}$ (Ai32)* mice with AAV2/1-Cre C1 DC injection at P12. The majorities of YFP^{+} free nerve endings are also labeled by the *TrkC^{tdTomato}* and are weakly NFH^{+}.

(B) Cross section of hindpaw glabrous skin from CGRP-GFP; *TrkC^{tdTomato}* mouse shows that the TrkC^{+} free nerve endings are CGRP^{-}.

(C) DRG section from *TrkC^{tdTomato}* mouse shows that all of the TrkC^{+} DRG neurons are IB4^{-}.

Scale bar: 100 μm (A-C).

Figure 6.13

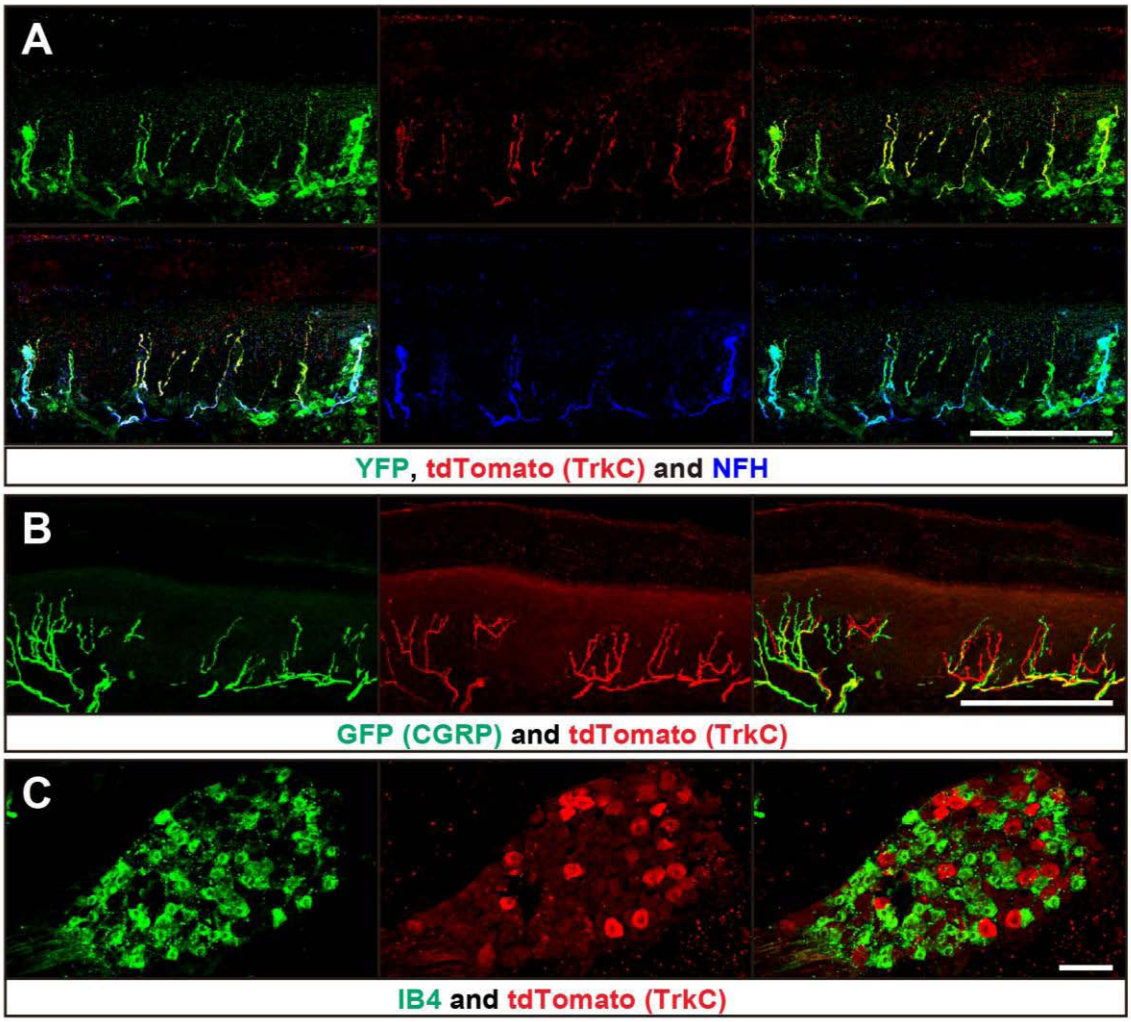
A
YFP, tdTomato (TrkC) and NFH
B
GFP (CGRP) and tdTomato (TrkC)
C
IB4 and tdTomato (TrkC)

Figure 6.14 Optogenetic activation of Aβ-LTMRs induces nocifensive behavior after SNI.

(A) Schematic for the optogenetic-stimulation on the hindpaw (473nm, 200mW at the tip, 200 Hz with 3 ms pulse width for 2 s).

(B) Allodynia score measured 8 days after SNI shows that optogenetic-stimulation induces an allodynia-like response in the experimental mice that express ReaChR in Aβ-LTMRs. The same stimulation does not induce allodynia-like responses in the control mice, which do not express ReaChR. Both experimental and control mice show mechanical allodynia in response to mechanical stimulation induced by gentle brushing. Two-way ANOVA: $p = 0.0170$, $F[1,8] = 9.012$. Post hoc Sidak's test: $^{**}p < 0.001$.

Figure 6.14

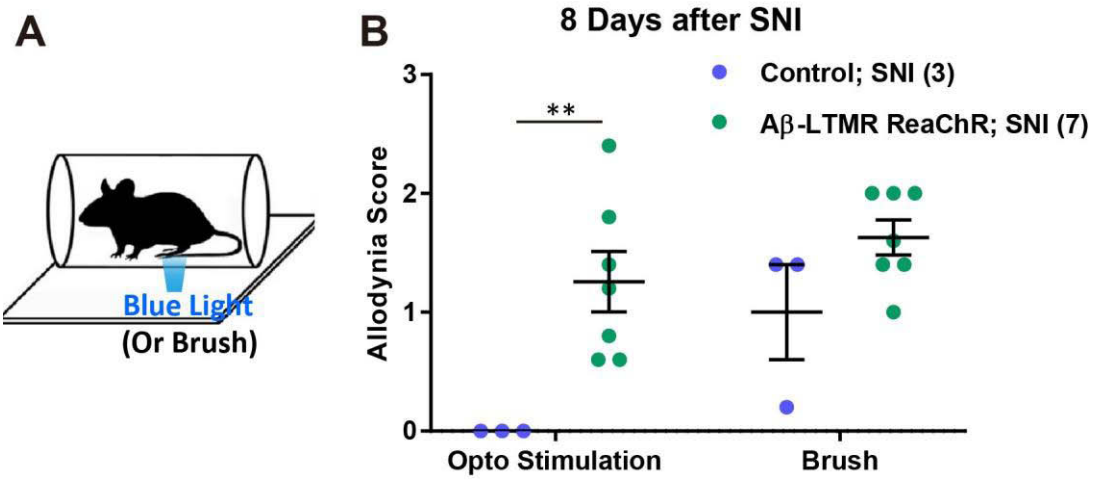
A
Blue Light
(Or Brush)
B
8 Days after SNI
Control; SNI (3)
Aβ-LTMR ReaChR; SNI (7)
**
Allodynia Score
3
2
1
0
Opto Stimulation
Brush

Figure 6.15 Aβ-LTMRs form synaptic bouton onto PSDC neurons.

(A-E) DCN injection of ΔG-GFP retrogradely labels PSDC neurons. The rabies retrograde labeling is carried out in mice with sensory neuron type-specific Cre and *R26*$^{LSL\text{-}Syn\text{-}tdTomato}$ *(Ai34)* to reveal the connectivity between sensory neuron subtypes and PSDC neurons.

(A) Schematic for rabies injection to retrogradely label PSDC neurons.

(B-E) Immunostaining of GFP, tdTomato, and Homer 1 on 10 μm thick spinal cord sagittal slices reveals the location of PSDC dendrites and sensory terminals from Aβ RA1-LTMRs (B-D) and Aδ-LTMRs (E). (C) Magnified and masked view of the region in the white box of (B). Signal from Homer 1 staining is selected if it is inside of the GFP^+ dendrites, while signal from syn-tdTomato is selected if it is less than 1 μm away from GFP^+ dendrites.

Scale bar: 20 μm (B-C), 200 μm (D-E).

Figure 6.15

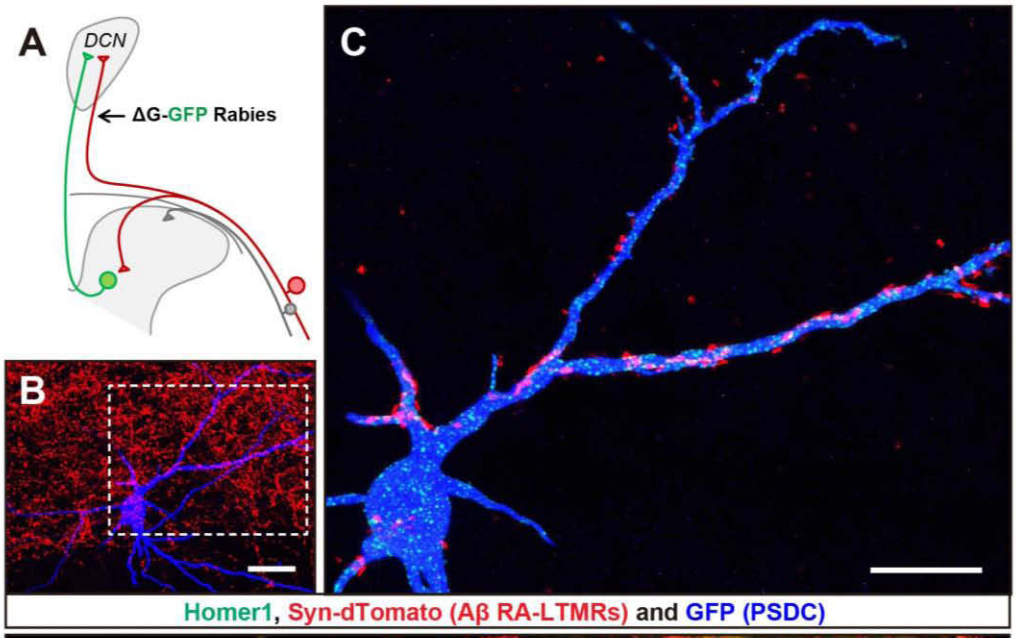
A
DCN
ΔG-GFP Rabies
B
C
Homer1, Syn-dTomato (Aβ RA-LTMRs) and GFP (PSDC)

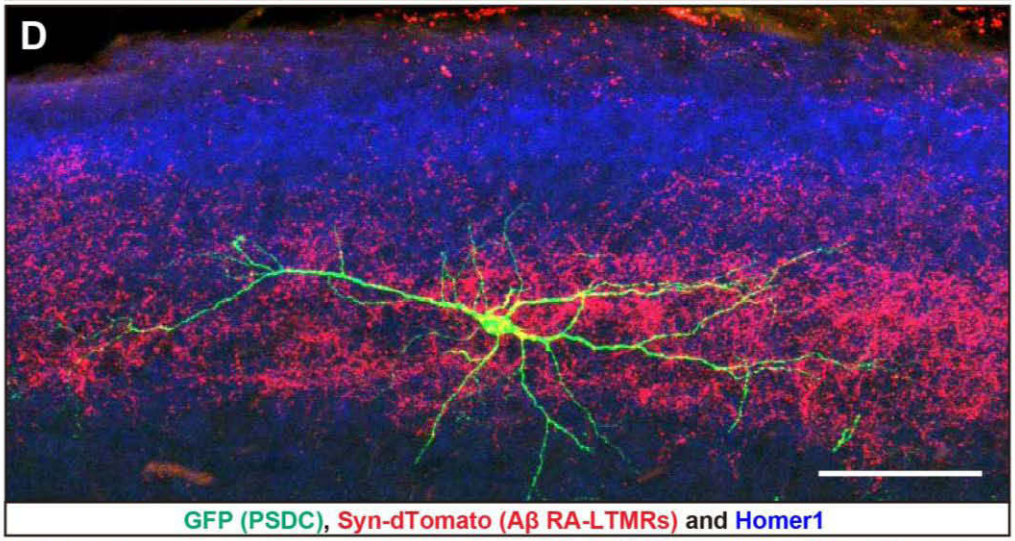
D
GFP (PSDC), Syn-dTomato (Aβ RA-LTMRs) and Homer1

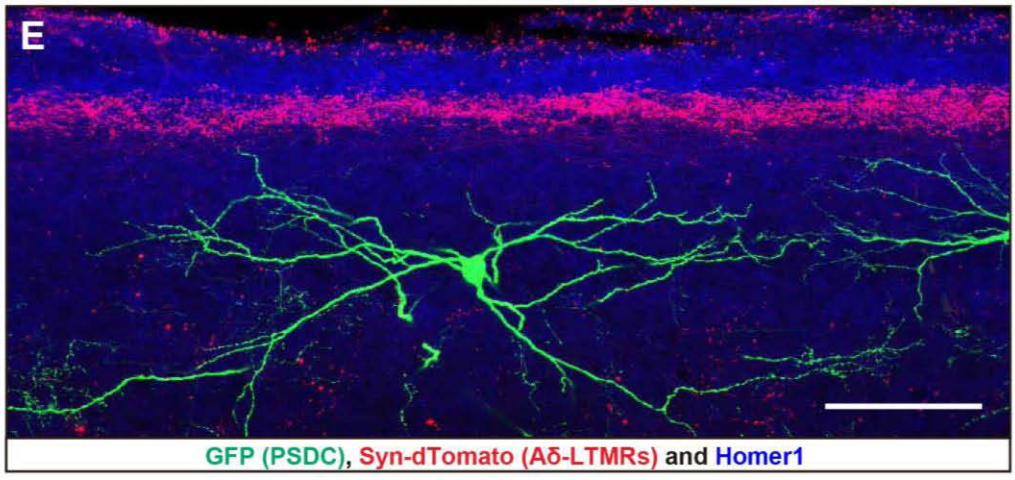
E
GFP (PSDC), Syn-dTomato (Aδ-LTMRs) and Homer1

Figure 6.16 Physiological recordings reveal that Aβ-LTMRs provide excitatory input to the PSDC neurons.

(A) Diagram depicting whole-cell patch clamp configuration for recording from PSDC neurons that are retrogradely labeled by CTB-555.

(B) Representative traces of CTB-555^{+} PSDC neurons recorded from sagittal spinal cord slices of *Ret^{CreER}; Ai32* mice with 3mg Tamoxifen at E11.5. Light activation of ChR2-labeled Aβ RA-LTMRs induces an inward current (excitatory) when the PSDC neuron is held at -60mV. This inward current is blocked by NBQX (grey trace).

Figure 6.16

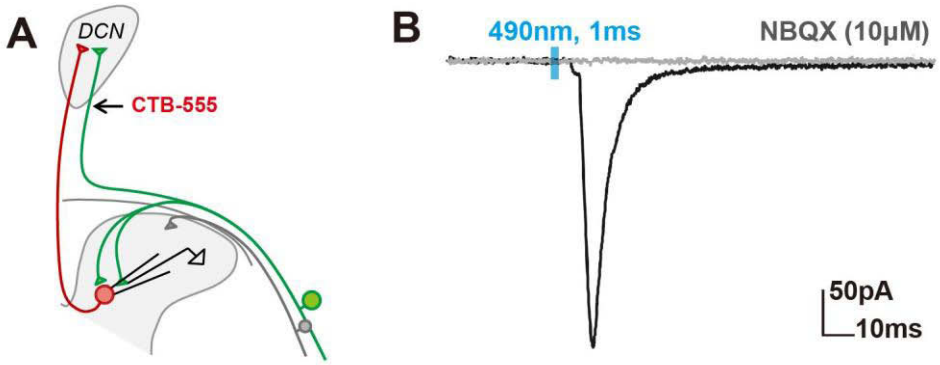

Chapter 7. Discussion

Sensory neurons that innervate the skin exhibit tremendous anatomical diversity. For the LTMRs, which mediate our sense of touch, the specialized anatomy of their endings is intimately related to their functions as mechanotransducers. Here we report the generation of novel murine genetic tools that label a major population of DRG sensory neurons that form NFH^+ circumferential endings around body hair follicles of mammals and show that these neurons are the elusive Aβ Field-LTMRs (formerly called field receptors). Remarkably, Aβ Field-LTMRs are highly sensitive to gentle stroking of the skin, but they also encode the intensity of skin indentation into the noxious range and they are completely unresponsive to hair deflection. Our findings indicate that the unique sensitivity of Aβ Field-LTMRs to gentle skin stroking reflects a combination of the shape and localization of their circumferential endings, expansive receptive fields that contain dozens of weakly mechanosensitive endings, and variably and often distantly localized SISs. These findings support a model in which gentle stroking across a large area (or field) of hairy skin leads to spiking in Aβ Field-LTMRs through convergence or integration of receptor potentials across many weakly mechanosensitive circumferential endings.

7.1. Neurons with NFH^+ circumferential endings display hallmarks of Aβ Field-LTMRs

Although originally described in cats in the 1960s by Burgess and colleagues as a hairy skin LTMR subtype, few modern studies of LTMRs mention Aβ Field-LTMRs. The paucity of information regarding Aβ Field-LTMRs is likely due to a combination of the heavy emphasis placed on glabrous skin sensory neurons in most physiological analyses, the relative ambiguity of their physiological properties, and a lack of tools to study this particular neuronal population. Our novel intersectional genetic labeling strategy to visualize sensory neuron subtypes in conjunction with targeted physiological recordings allowed us to establish that a major population of DRG neurons in mouse hairy skin exhibits the key hallmarks of Aβ Field-LTMRs. We found that Aβ

Field-LTMRs are numerous, comprising more than 4% of DRG neurons of the mouse. Each Aβ Field-LTMR innervates up to 180 hair follicles with NFH^+ circumferential endings, which are prevalent across mammalian species. They are highly sensitive to gentle stroking of the skin but do not respond to hair deflection. Moreover, Aβ Field-LTMRs are increasingly responsive to skin indentation in the noxious range and have large, spotty indentation receptive fields; these properties are highly unique amongst the Aβ-LTMR subtypes.

The genetic labeling of Aβ Field-LTMRs enabled us to quantitatively interrogate their physiological properties using different modes of cutaneous stimulation. In previous studies employing few modes of stimulation, these neurons may have been misclassified. Indeed, we found using *in vivo* recordings that Aβ Field-LTMRs exhibit properties often associated with Aβ RA-LTMRs; they respond to gentle stroking of skin and are rapidly adapt to skin indentation. Thus, without testing sensitivity to hair deflection or indentation thresholds, these neurons may have been misclassified as Aβ RA-LTMRs. On the other hand, Aβ Field-LTMRs have properties consistent with Aβ nociceptors (Djouhri and Lawson, 2004) and thus may have been classified as such. Indeed, both *in vivo* and *ex vivo* recordings showed that they are far less sensitive to skin indentation compared to other Aβ-LTMRs and encode stimulus intensity (Figure 2.7E and 2.8C), and *ex vivo* recordings showed that they have relatively broad inflected somal action potentials (Figure 2.8A). It is therefore tempting to speculate that Aβ Field-LTMRs have a nociceptor function, under certain conditions, and a test of this possibility will require activation, silencing or ablation approaches and behavioral measures.

While Aβ Field-LTMRs form NFH^+ circumferential endings associated with most, if not all, body hairs, there is a second, anatomically and molecularly distinct population of neurons exhibiting circumferential endings whose physiological properties are unknown. The circumferential endings of this second population are entwined with those of Aβ Field-LTMRs,

and they differ from Aβ Field-LTMRs in that their peripheral endings express CGRP, but not NFH, and their central projections do not extend to the DCN, suggesting they are a lightly myelinated or unmyelinated sensory neuron subtype. Consistent with this, preliminary findings indicate that DRG neurons that form $CGRP^{+}/NFH^{-}$ circumferential endings have an intermediate diameter, NFH^{+} soma (data not shown) and thus may be an Aβ neuronal subtype. Defining the physiological properties and functions of neurons that form $CGRP^{+}$ circumferential endings must await the availability of molecular-genetic tools that enable directed physiological recordings and functional manipulation of this population.

7.2. Structural and molecular features define the unique tuning properties of Aβ Field-LTMRs

The Aβ Field-LTMR is unique amongst Aβ-LTMR subtypes; it is highly sensitive to gentle skin stroking while, on the other hand it is remarkably insensitive to innocuous skin indentation and completely unresponsive to hair deflection. In contrast, the other major Aβ-LTMR subtype whose endings wrap around hair follicles, the Aβ RA-LTMR, is highly sensitive to stroking as well as indentation and hair deflection. Why do these two hair follicle-associated Aβ-LTMRs differ in their sensitivity to hair deflection and skin indentation? To address this question, we compared the physiological, morphological, and ultrastructural properties of Aβ Field-LTMRs and Aβ RA-LTMRs.

Our *in vivo* recordings indicate that Aβ Field-LTMRs have a large number of weakly mechanosensitive hotspots distributed across a large area of skin. Although the precise number of hotspots is difficult to ascertain, their approximate number and distribution bears striking resemblance to the number and distribution of circumferential endings of individual Aβ Field-LTMRs, visualized by sparse genetic labeling. The simplest interpretation of this observation is that each Aβ Field-LTMR circumferential ending is a weakly mechanosensitive unit. Why are

individual circumferential endings of Aβ Field-LTMRs weakly mechanosensitive compared to Aβ RA-LTMR lanceolate endings? One important clue stems from the observation that Aβ RA-LTMR longitudinal lanceolate endings are closely associated with hair follicle epithelial cells, whereas Aβ Field-LTMR circumferential endings are not. In fact, the naked axonal membrane of individual lanceolate projections resides within 100 nm of the hair follicle epithelial cell membrane (Li and Ginty, 2014) (Figure 3.2A and 3.2C). This intimate physical apposition strongly implicates the lanceolate membrane immediately adjacent to the hair follicle epithelial cell as the site where hair deflection-induced mechanical forces are transduced into Aβ RA-LTMR axonal membrane depolarization and excitation. In contrast, Aβ Field-LTMR circumferential endings are located about 4 μm from hair follicle epithelial cells where they are enveloped by terminal Schwann cell processes. A second distinguishing feature is that Aβ RA-LTMR longitudinal lanceolate endings are arranged within an inner follicle region containing longitudinally oriented collagen fibrils, whereas Aβ Field-LTMR circumferential endings are located within an outer follicle region comprised of circumferentially oriented collagen fibrils. We propose that the highly distinct physical relationships between the Aβ RA-LTMR (longitudinal lanceolate) and Aβ Field-LTMR (circumferential) endings and hair follicle epithelial cells and their positions within distinct collagen layers underlie the differential sensitivity of these two LTMR subtypes to hair deflection. In support of this view, our FEM simulations suggest that the longitudinal orientation of lanceolate endings within the inner longitudinal collagen layer renders Aβ RA-LTMR lanceolate endings susceptible to much greater strain following both hair deflection and skin indentation, compared with Aβ Field-LTMR circumferential endings.

How do Aβ Field-LTMRs, each with a large number of weakly mechanosensitive circumferential endings, respond to gentle stroking of the skin? Our analysis of MBP and βIV-Spectrin localization patterns suggests that Aβ Field-LTMR SISs are often located far away from

their hair follicle circumferential endings, whereas, in all cases analyzed, Aβ RA-LTMR SISs are located immediately adjacent to their hair follicle longitudinal lanceolate endings. These findings, taken together, support a model in which three unique features of Aβ Field-LTMRs combine to render these neurons highly sensitive to wide-field indentations that sweep across large fields of hairy skin but relatively insensitive to deflection of individual hairs and skin indentation. These features are: 1) Aβ Field-LTMR circumferential endings are distantly located from hair follicle epithelial cells in an outer layer of circumferentially oriented collagen fibers and thus, compared to Aβ RA-LTMR longitudinal lanceolate endings, circumferential endings are relatively insensitive to hair deflection or innocuous skin indentation; 2) The morphological receptive fields of Aβ Field LTMRs are extremely large with individual neurons innervating up to 180 hair follicles in areas that encompass ~3 mm^2, enabling convergence and summation of receptor potentials emanating from multiple circumferential endings; and 3) Aβ Field-LTMR SISs are typically located more than 100 μm away from the circumferential endings, suggesting a lower transformation efficiency of receptor potentials to action potentials compared to Aβ RA-LTMRs, which may lead to a relative insensitivity to focal mechanical stimuli and convergence and summation of receptor potentials from multiple circumferential endings of a single neuron. Thus, we propose that when a "field" of weakly mechanosensitive circumferential endings associated with outer layers of hair follicle circumferential collagen are activated, receptor potentials emanating from individual circumferential endings converge or summate at distally located SISs to initiate Aβ Field-LTMR spiking. In contrast, the extremely close apposition of hair follicle epithelial cells and Aβ RA-LTMR lanceolate endings and thus the high sensitivity to shear on these endings during follicle movement, as well as the immediate adjacency of these lanceolate endings to SISs enable Aβ RA-LTMRs to spike following deflection of a single hair. Moreover, the slightest skin indentation causes hair follicle movement, leading to Aβ RA-LTMR excitation. In this model, the unique physiological response properties of Aβ Field-LTMRs and Aβ RA-

LTMRs are a consequence of their terminal morphology, mechanical linkage to the follicle and surrounding skin, and the differential locations of their respective SISs. It is also possible that Aβ Field-LTMRs and Aβ RA-LTMRs differ in expression of mechanically-gated ion channels and transduction machinery, and such molecular differences may also contribute to their unique physiological response properties.

7.3. Why do mammals have Aβ Field-LTMRs?

Aβ Field-LTMRs directly project to the brainstem through the DC, suggesting they function in discriminative touch sensation. Why do mammals have an LTMR that is highly sensitive to gentle skin stroking, but not to innocuous indentation or hair deflection, when all other cutaneous LTMRs are also sensitive to skin stroking? We favor an integrative LTMR coding model to explain hairy skin discriminative touch. In this model, unique combinations or ensembles of the cutaneous LTMR subtypes, each with its unique sensitivity, conduction velocity and rate of adaption, enables a wide range of touch percepts. Thus, activity ensembles comprised of five LTMR subtypes represent stroking of hairy skin: these are the Aβ Field-LTMR, Aβ SA1-LTMR, Aβ RA-LTMR, Aδ-LTMR and C-LTMR. Air puffs, on the other hand, are represented by ensembles of LTMRs harboring longitudinal lanceolate endings: Aβ RA-LTMRs, Aδ-LTMRs and C-LTMRs. Innocuous indentation of the skin is represented by ensembles of all LTMR subtypes, except for Aβ Field-LTMRs which are insensitive to innocuous indentation. In this model, the overlapping but distinct tuning properties of the LTMR subtypes, which is a function of their unique terminal morphologies, receptive field properties, and SIS positions, underlies a wide range of touch percepts. We propose that Aβ Field-LTMRs, with their characteristic expansive receptive fields comprised of large numbers of weakly mechanosensitive circumferential endings, contribute to ensembles that underlie percepts associated with gentle stroking across large fields of hairy skin. Future work will define the contributions of Aβ Field-

LTMRs to tactile perception and sensory-motor reflexes, and the postsynaptic partners and circuits in the dorsal horn and brainstem that receive, integrate, and process Aβ Field-LTMR and other LTMR subtype activities.

7.4. A novel ascending pathway for the peripheral neuropathic pain

For a long time it has been assumed that the ALT conveys nociceptive information out of the spinal cord, including under pathological conditions such as peripheral neuropathic pain. However, the dogma of the ALT underlying pathological pain sensation may lack evidence. Most lesion studies in cat, non-human primates, and human patients have focused on the detection of pain under non-pathological conditions, and the ascending mechanisms under peripheral neuropathic pain conditions are largely unknown.

The only evidence supporting a role of the ALT in peripheral neuropathic pain comes from a study in Rat, in which the $NK1R^+$ neurons are ablated by intrathecal injection of Substance P-Saporin (Mantyh, 1997; Nichols, 1999). There researchers have found that mechanical hypersensitivity is reduced after $NK1R^+$ neurons ablation. Since NK1R is expressed in subsets of ALT projection neurons in the spinal cord dorsal horn, the phenotype following $NK1R^+$ neuron ablation is thought at least partially due to the lack of ALT projection neurons. However, it has also been shown that $NK1R^+$ neurons not only exist on the lamina I of the spinal cord dorsal horn, but are also located through the deep laminae. Thus, it is possible that $NK1R^+$ neurons which do not belong to the ALT projection population are involved in the mechanical hypersensitivity after SNL. Indeed, the signal of NK1R staining did reduce in the deep spinal cord dorsal horn after Substance P-Saporin intrathecal injection. Moreover, by crossing $NK1R^{CreER}$ to a Cre dependent lacZ report $Tau^{LSL\text{-}lacZ}$, we found that about half of all PSDC neurons are labeled by βgal antibody staining, suggesting that NK1R is expressed in at least subsets of PSDC neurons. These results suggest that the reduction of SNI induced mechanical hypersensitivity after $NK1R^+$ neurons

ablation could be explained by a loss of PSDC neurons, which is consistent with our finding that PSDC neurons are required for development of peripheral neuropathic pain. Further experiments are required to examine the extent of PSDC neuron loss following Substance P-Saporin intrathecal injection.

Several lesion studies in rat and human patients have suggested a role of the DC pathway in the peripheral neuropathic pain, though those studies have been largely ignored, while the ALT is still considered as the main ascending pathway for neuropathic pain. Recently, two papers have shown that in rat, the mechanical hypersensitivity after peripheral nerve injury could be abolished by a DC lesion, or local DCN anesthesia (Ossipov et al., 2002; Sun et al., 2001). Deliberate lesions of the DC in human patients have been made surgically in an attempt to relieve phantom limb pain, which may share some similarity to the peripheral neuropathic pain. In addition, lesion studies have also suggested that the DC are involved in visceral nociception (Willis et al., 1999) as well as hyperalgesia and allodynia due to the bone pain produced by an osteotomy (Houghton et al., 1999). Together, these results have suggested that the dorsal column could be involved in nociceptive sensation under certain pathological conditions.

However, one major issue of previous lesion studies is the lack of a proper assessment of the lesion. Most of the studies on human patients lack postmortem confirmation of the extent of the lesions. Even in animal studies in which the extent of lesions is confirmed by histology of the lesion site, it is difficult to assess which ascending pathways that are disrupted by the lesion. In order to address this issue, I've designed a virus tracing strategy to visualize the ascending pathways through the DC and the ALT, which has helped us to interpret our behavior results. We found that lesion of the dorsal column, but not the contralateral side of ALT, disrupted mechanical hypersensitivity/allodynia induced by SNI, which is consistent with the dorsal column lesion study in the rat. However, it is difficult to conclude whether ALTs are involved in the

development of peripheral neuropathic pain, since some ALT projections ascend to the ipsilateral side of the brainstem, which is spared by the lesion of the contralateral side. A specific genetic manipulation of neurons in the ALT is required to further address their involvement in the development of peripheral neuropathy.

7.5. Are PSDC neurons required for spinal cord mechanisms of peripheral neuropathic pain development?

Our results have challenged the current view that ALT projections convey mechanical allodynia. Decades of pharmacological studies, molecular genetics, and circuits mapping have established dozens of spinal cord mechanisms underlying peripheral neuropathic pain, including changes of the presynaptic release, postsynaptic receptors, spinal cord local circuits, and glia cells. It has been assumed that those spinal cord mechanisms all converge onto ALT ascending pathways to convey mechanical pain information to higher levels of the central nervous system. Though it has been shown in rat that DC lesions may abolish peripheral neuropathic pain, the DC hypothesis was thought to be in conflict with the aforementioned spinal cord mechanisms and may have been ignored due to this confliction.

However, our results have shown that spinal cord PSDC neurons ascend through the DC and are required for the development of peripheral neuropathy. Thus, signals in the spinal cord dorsal horn could converge onto the PSDC neurons where they are further conveyed to the higher level of the brain. Indeed, we found that PSDC neurons receive direct input from Aβ-LTMRs, which are also involved in peripheral neuropathic pain. The unique locations of PSDC neurons and their projects to the DCN lead to a model in which previously identified spinal cord mechanisms converge onto PSDC neurons for the development of peripheral neuropathy. If that's the case, our findings may define a key component of the peripheral neuropathic pain and solve a conflict in the field.

In the future, we are interested in examining this hypothesis by asking whether spinal cord mechanisms underlying mechanical allodynia in neuropathic pain states change the activity of PSDC neurons. Firstly, we would like to examine whether the strength of sensory input to PSDC neurons is increased after SNI, either through a direct regulation of primary sensory terminals, or through one or more spinal cord interneuron mechanisms. On the other hand, interneuron subtypes in the spinal cord dorsal horn are implicated in peripheral neuropathy (Peirs et al., 2015; Petitjean et al., 2015). For example, spinal cord vGlut3^{+} interneurons are required for the development of the peripheral neuropathy. Activation of vGlut3^{+} neurons leads to mechanical hypersensitivity/allodynia, while inhibition of vGlut3^{+} neurons abolishes mechanical hypersensitivity/allodynia after SNI. Thus we would like to further examine whether vGlut3^{+} spinal cord neurons interact with PSDC neurons and whether activation/silencing vGlut3^{+} neurons alters the activity of PSDC neurons. Exciting preliminary results suggest that vGlut3^{+} interneurons indeed form direct inputs to the PSDC neurons, and future experiments will examine the state of this interaction after peripheral neuropathy.

Materials and methods

Mouse lines

TrkC^{tdTomato} and *TrkC*^{CreER} mice were generated using targeting vectors that were made utilizing a 2-step recombineering protocol that has been described previously (Li et al., 2011; Rutlin et al., 2014). To generate targeting vectors, a 112 kb 129/SvJ BAC clone (bMQ386a05) containing exon 1 of the *TrkC* gene was obtained from Geneservice. 245 bp of exon 1 following the first coding ATG of the *TrkC* gene was replaced by either a tdTomato or Cre recombinase-estrogen receptor T2 (CreERT2) fusion-Frt-Neomycin-Frt-loxP cassette, with 2 kb upstream and 8 kb downstream regions of the insertion. Targeting vectors were linearized with XhoI (for *TrkC*^{tdTomato}) or AscI (for *TrkC*^{CreER}) digestion and homologous recombination was performed in mouse 129S6SvEvTac embryonic stem (ES) cells using standard procedures. Correctly targeted ES cell clones were identified by Southern blot analysis with using probes downstream of the insertion following AseI digestion (wild-type fragment 13.6 kb, *TrkC*^{tdTomato} fragment 8.8 kb, *TrkC*^{CreER} fragment 9.2 kb). ES cell clones with non-specific insertions were excluded by Southern blot analysis using probes of the neomycin cassette following NdeI digestion (wild-type with no band, *TrkC*^{tdTomato} fragment 10.9 kb, and *TrkC*^{CreER} fragment 11.3 kb). Chimeric mice were produced by blastocyst injection of karyotypically normal ES cells. *TrkC*^{tdTomato} and *TrkC*^{CreER} heterozygous mice were generated by mating chimeras to *Actb-FlpE* mice to remove the neomycin selection cassette. *TrkC*^{tdTomato} and *TrkC*^{CreER} mice negative for the neomycin selection cassette were then backcrossed and maintained on a C57/BL6 background. Genotyping of *TrkC*^{CreER} mice followed the Jackson Cre genotyping protocol, whereas genotyping of *TrkC*^{tdTomato} mice was done using two primers in the targeting construct: CTGTTCCTGTACGGCATGG and GGAAAGGACAGTGGGA GTG. The length of the PCR product for the *TrkC*^{tdTomato} allele is 249 bp. *Avil*^{Flpo} is a knock in mouse line generated by homologous recombineering which will be described elsewhere. *Ret*^{CreER} (Luo et al., 2009), *TrkB*^{CreER} (Rutlin et al., 2014); *TH*^{iCreER} (Rotolo

et al., 2008); *Lbx1*^{Cre}; Tau$^{ds\text{-}DTR}$ (Bourane et al., 2015); *RC::FrePe* (Bang et al., 2012); *RC::PF-Tox* (Ray et al., 2011); *R26*$^{LSL\text{-}tdTomato}$ (*Ai9*), *R26*$^{FSF\text{-}LSL\text{-}tdTomato}$ (*Ai65*), Actb-Flpe (The Jackson Laboratory), *Brn3a*$^{f(AP)}$ (Badea et al., 2009), *Ret*^{CFP}, *Ret*$^{f(CFP)}$ (Uesaka et al., 2008), and CGRP-GFP (GENSAT) mouse lines have been previously described. Mice were handled and housed in accordance with the Harvard Medical School and Johns Hopkins University IACUC guidelines.

Tamoxifen treatment

Tamoxifen was dissolved in ethanol (20 mg/ml), mixed with equal volume of sun flower seed oil (Sigma), vortexed for 5-10 mins and centrifuged under vacuum for 20-30 mins to remove the ethanol. The solution was kept at -20^{o}C and delivered via oral gavage to pregnant females for embryonic treatment, or via intraperitoneal injection for postnatal treatment. For all analyses, the morning after coitus was designated as E0.5 and the day of birth as P0.

Diphtheria Toxin Ablation

To ablate DTR-expressing DRG neurons, 6-10 week old mice were injected intraperitoneally with diphtheria toxin (DTX, 100 μg/kg; Sigma-Aldrich, USA) at day 1 and then again at day 4. Behavioral analyses were performed 7 days post DTX injection, prior to the development of spontaneous scratch. Littermates lacking the expression of DTR were used as controls and all animals received DTX injection.

Dorsal column virus injections

Mice (P10-P21) were anesthetized via continuous inhalation of isoflurane (1-3%) from a precision vaporizer for the 30-60 minutes duration of the surgery. The animal's breathing rate was monitored throughout the procedure and the anesthetic dose was adjusted as necessary. Puralube eye ointment was applied to the eyes. The back of the neck was shaved, treated with commercial depilatory cream (NAIR, Church and Dwight Co.; Princeton, NJ) for 0.5-1 min, and swabbed with water and Betadine. A 5 mm incision was made in the midline of the back skin at

the cervical level and local anesthetic (0.5% lidocaine) was applied to the incision site. Muscles were cut or separated from the midline until the spinal cord cervical vertebrae were exposed. A small incision was made on the dura and arachnoid membranes between the C1 and C2 cervical spinal vertebrae to expose the DC. 100-200 nl of Adeno-Associated Virus (AAV2/1-CMV-Cre, titer $9.78e^{12}$ in 0.9% saline, Penn Vector Core) was injected into the DC at the C1-C2 level using a glass pipette under visual guidance. Afterwards, muscles and skin were stitched together with sutures, and Carprofen (4 mg/kg) was applied subcutaneous for analgesia. Mice recovered from anesthesia on a warm pad for 1 hr and were returned to their home cage (housed in groups of 5). Additional doses of Carprofen were injected intraperitoneally at 24 and 48 hrs post-operation. The condition of the mice including the healing of wounds, body weight and grooming, were monitored daily. At the appropriate time point (typically 4 weeks) mice were sacrificed by CO_2 asphyxiation followed by perfusion.

Spared nerve injury (SNI)

The spared nerve injury (SNI) model for neuropathic pain was performed on adult control and ablated mice (10-14 weeks) as described previously (Decosterd and Woolf, 2000). Briefly, unilateral spared nerve injury was done by exposing the sciatic nerve in the thigh region of the adult mouse, cutting and ligating the tibial and common peroneal nerves, and leaving the remaining sural nerve intact. Animals were subjected to von Frey and dynamic brushing test at 2 days, 8 days, and 21 days after lesion, on the lateral plantar region of the hindpaw that was innervated by the sural nerve.

Immunohistochemistry of tissue sections

Mice (P10-P50) were anesthetized with CO_2 and perfused with 5ml PBS followed by 10-20ml of 4% paraformaldehyde (PFA) in PBS at room temperature (RT). For tissue sourced from other species, Zamboni-fixed skin samples were obtained from *Canis familiaris*, *Felis catus*, *Callithrix jacchus* (common names dog, cat, marmoset). Sources included veterinary surgical discards,

tissue harvested following predation or accident, and tissue sourced from animal control specialists. Spinal cords, dorsal root ganglia (DRG) and skin were dissected from perfused mice. Neural tissues were post-fixed in 4% PFA at 4°C for 4-8 hours, while skin was post-fixed in Zamboni's fixation buffer at 4° C for 24 hours. Tissues were cryoprotected in 30% sucrose in PBS at 4°C overnight, embedded in OCT and frozen at -20°C. Tissues were sectioned at 20 μm (for DRG) or 30 μm (for spinal cord or skin) with a cryostat. The sections on slides were dried at RT for 1 hour, washed 3×10 minutes with PBS containing 0.1% Triton X-100 (0.1% PBST) and then blocked with PBS containing 0.3% Triton X-100 and 5% normal goat serum (Vector Labs, S-1000) or normal donkey serum (Jackson Immuno, 005-000-121) for 30 min at room temperature. Tissue sections were incubated with primary antibodies diluted in blocking solution at 4°C overnight. The next day, sections were washed with 0.1% PBST, and incubated with secondary antibodies 1:500 diluted in blocking solution at room temperature for 2 hours, washed again 3×10 minutes with 0.1% PBST, and mounted with fluoromount-G (Southern Biotech). IB4 was diluted at 1:500 and incubated together with secondary antibodies. Primary antibodies include: chicken anti-GFP (GFP-1020, Aves Labs; 1:1000), rabbit anti-GFP (A-11122, Life Technologies; 1:1000), rabbit anti-DsRed (632496; Clontech; 1:1000), goat anti mCherry (AB0040-200, Acris, 1:1000), rabbit anti-parvalbumin (Swant, PV25, 1:1000), rabbit anti-CGRP (Immunostar, 24112, 1:1000), rabbit anti-NF200 (Millipore, AB1982, 1:1000; Sigma, N4142, 1:1000), chicken anti-NF200 (Aves Labs, NFH, 1:1000), rat anti-Troma1 (Univ of Iowa/DSHB, 1:100), guinea pig anti-VGLUT1 (ab5905, Millipore; 1:1000), rat anti-MBP (Abcam, ab73349, 1:1000), rabbit anti βIV-Spectrin (from Dr. Matthew N. Rasband, 1:200), rabbit anti-PKCγ (SC-211, Santa Cruz Biotechnology; 1:1000), Alexa 647-conjugated IB4 (Life Technologies, 1:1000). Secondary antibodies included: Alexa 488, 546 or 647 conjugated goat anti-chicken antibodies, Alexa 488, 546 or 647 conjugated goat anti-guinea pig antibodies, Alexa 488, 546 or 647 conjugated goat anti-rabbit antibodies, Alexa 488, 546 or 647 conjugated goat anti-rat antibodies, Alexa 488, 546

or 647 conjugated donkey anti-goat antibodies, Alexa 488, 546 or 647 conjugated donkey anti-rabbit antibodies, Alexa 647 conjugated donkey anti-rat antibodies. All secondary antibodies above were purchased from Life Technologies. Alexa 488/647 conjugated donkey anti-chicken antibodies and Alexa 647 conjugated donkey anti-guinea pig antibodies were purchased from Jackson ImmunoResearch.

Whole-mount immunohistochemistry of the skin

The protocol for skin whole-mount immunohistochemistry was performed as previously described (Rutlin et al, 2014). Mice (P21 or P40) were euthanized with CO_2 and treated with commercial depilatory cream (NAIR, Church and Dwight Co.; Princeton, NJ) for 0.5-1 min, and washed with hand soap. Skin was dissected and fixed in Zamboni's fixation buffer at 4^{o}C overnight, washed with PBS for 5×20 min followed by 1% PBST for 3×1 hour, then incubated with primary antibodies diluted in blocking solution (75% 1% PBST, 20% DMSO, 5% Normal Goat Serum, 0.02% NaN3) on a rocking platform for 2 days at RT. The skin was washed in PBST with 1% Triton X-100 for 5 times for 5 hours at RT, then incubated with secondary antibodies in blocking solution on rocking platform for 2 days at RT. The skin was washed again in PBST with 1% Triton X-100 for 5 times for 5 hours at RT and then dehydrated in 100% MeOH (3× wash) overnight on a rocking platform at room temperature. The next day, skin was pinned to a glass dish coated with Polydimethylsiloxane (PDMS), cleared in BABB (BABB: 1 part Benzyl Alcohol: 2 parts Benzyl Benzoate) for 5 min, and mounted on slides using BABB as mounting medium.

Whole-mount immunohistochemistry of the spinal cord

The protocol for whole-mount immunohistochemistry was performed as previously described (Luo et al., 2009). Mice (P10-P50) were anesthetized with CO_2 and perfused with 5ml PBS followed by 10-20ml of 4% paraformaldehyde (PFA) in PBS at room temperature (RT). Vertebral column were dissected from perfused mice and post-fixed in 4% PFA/PBS at 4^{o}C overnight.

Tissues were then washed with PBS three times for 20 minutes at room temperature and spinal cords were further dissected out from fixed tissue. Spinal cords were embedded into 3-4% agarose (in PBS) and 100μm sagittal sections were made by vibratome section. Spinal cord sections were further washed with PBS with 0.5mM Glycine for 5×20 min followed by PBST with 1% Tween-20 and 1% Triton X-100 for 3×1 hour, then incubated with primary antibodies diluted in blocking solution (95% PBST with 1% Tween-20 and 1% Triton X-100, 5% Serum, 0.02% NaN_3) on a rocking platform for 2 days at 4°C. The sections were washed in PBST with 1% Tween-20 for 5 times for 5 hour at RT, then incubated with secondary antibodies in blocking solution on rocking platform for 2 days at 4°C. The sections were washed again in PBST with 1% Tween-20 for 5 times for 5 hours at RT and then dehydrated in 100% MeOH (3× wash) overnight on a rocking platform at RT. The next day, sections were cleared in BABB (BABB: 1 part Benzyl Alcohol: 2 parts Benzyl Benzoate) for 5 min, and mounted on slides using BABB as mounting medium.

Whole-mount PLAP staining of the skin and spinal cord

Whole-mount placental alkaline phosphatase staining was performed as previously described (Liu et al., 2007). Mice (P21 or P40) were euthanized and hair was removed as above. Spinal cords, DRGs and skins were dissected from perfused mice and post-fixed in 4% PFA/PBS at 4°C overnight. Tissues were then washed with PBS three times for 20 minutes at room temperature, subjected to heat shock for 2 hr at 65-68° C, wash with B3 buffer (0.1 M Tris pH 9.5, 0.1 M NaCl, 50 mM $MgCl_2$) for 10 minutes at room temperature. The AP signal was detected by incubating the tissues with BCIP/NBT (Roche) diluted at 3.4 μg/ml in B3 buffer (0.1 M Tris pH 9.5, 0.1 M NaCl, 50 mM $MgCl_2$) with 0.1% Tween-20 overnight at RT. The next day, tissues were washed with PBS, fixed with 4% PFA/ PBS for 4 hr at 4° C, rinsed with PBS, and dehydrated and cleared the same as the whole-mount immunohistochemistry protocol.

Single neuron morphological analysis

For single cell central projection analysis, *TrkC*^{CreER}*; Brn3a*$^{f(AP)}$ mice were treated with 0.001mg tamoxifen at P8 to label fewer than five neurons per animal. The entire skin was harvested to visualize the peripheral terminal morphology of labeled neurons. The spinal cord and brainstem were dissected out with DRGs attached. After AP whole-mount staining and imaging, the AP$^+$ sensory endings labeled in the skin were carefully matched with the AP$^+$ neurons in the DRG based on their somatotopic alignment. Only neurons forming circumferential or Merkel endings in the skin were further used for central projection analysis. The central projections in the spinal cord and DCN were analyzed only if they could be unambiguously traced from the labeled DRG neurons.

For AP receptive field analysis, *Brn3a*$^{f(AP)}$ mice were used as a sensory specific reporter. Aβ Field-LTMRs or Aβ SA1-LTMRs were labeled using *TrkC*^{CreER} treated with 0.01mg tamoxifen at P8. Aβ RA-LTMRs were labeled using *Ret*^{CreER} treated with 0.03mg tamoxifen at E11.5. Aδ-LTMRs were labeled using *TrkB*^{CreER} treated with 0.001mg tamoxifen at P10. C-LTMRs were labeled using *TH*$^{ires\text{-}CreER}$ treated with 2mg tamoxifen at P12-P14.

For spike initiation segments (SISs) analysis, Aβ Field-LTMRs or Aβ RA-LTMRs were sparsely labeled by *TrkC*^{CreER}*; R26*$^{LSL\text{-}YFP}$ with 0.5mg tamoxifen at E15.5 or *Ret*^{CreER}*; R26*$^{LSL\text{-}YFP}$ with 0.3mg tamoxifen at E11.5, respectively. Aβ SA1-LTMRs were labeled by immunostaining using anti-NFH and the Merkel cell marker, Troma1.

Laser Doppler Vibrometry

A 30 mm by 30 mm patch of freshly excised skin from the dorsal hindlimb was mounted upright on a 3-axis manipulator. To facilitate measurement of skin, a commercial depilatory cream (NAIR, Church and Dwight Co., Princeton, NJ) was used to remove the hair on the proximal third of the sample. Pilot experiments revealed that the back-scattered signal from skin is modest, so reflective cosmetics (Eyeshine, Milani) were applied to skin prior to measurement to increase backscattering of incident laser light. Measurements of stimulus-induced changes in skin and hair

velocity were taken with a laser Doppler vibrometer (Polytec OFV-5000 equipped with OFV-500, VD-06, and DD-500 decoder boards). The air puff velocity at the source was 15 m/sec (positioned 10-14 mm away), and the indentation was delivered with a 2 g von Frey filament attached to a solenoid actuator. Data acquisition and stimulus delivery was controlled by custom software written in Matlab (Mathworks, Natick, MA). Prior to air puff or von Frey indentation, the skin was translated using the micromanipulator until the laser measurement spot coincided with hair (300-500 μm from base) or skin adjacent to the base of hairs. Data was excluded if the quality of the backscattered signal dropped below 20% full scale (as indicated by the LDV) during the course of the mechanical stimulus.

***In vivo* electrophysiological recordings**

Recordings were made from genetically identified dorsal root ganglia neurons of anesthetized P20-P40 mice using a preparation modified from (Ma and LaMotte, 2007). This preparation allows measurement of action potentials evoked by cutaneous stimulation for up to four hours *in vivo*. Anesthesia was induced with a mixture of ketamine (200 mg/kg, i.p.) and xylazine (30 mg/kg, i.p.), and atropine (0.2 mg/kg, i.p.) was co-administered at surgery onset to alleviate bradycardia. Mice were then fitted with an endotracheal tube and transitioned to artificial ventilation with isoflurane (1.2–2% in 100% O_2) for the duration of the procedure. Hemostasis throughout the DRG exposure surgery was achieved through the use of thrombin (100 units/mL in PBS and 0.1% BSA) and injection of isotonic saline. Temperature was monitored and maintained at 35.5-37.5^{o}C with a temperature controller (TC-344B, Warner Instruments) and thermoelectric heater (C3200-6145, Honeywell) embedded in castable cement (Aremco). At the beginning of the DRG exposure, an incision was made over the spine (T10 - L6) and the overlaying tissue retracted to expose the vertebral column. The spine was secured with custom spinal clamps (Mike's Machine, Attleboro MA) and bone dorsal to the target DRG removed with rongeurs. After exposure of the DRG, the ensheathing membrane was removed with fine forceps.

In the majority of cases, the vasculature of the DRG was intact, such that blood flow could be visualized during the recording, while the cell bodies on the surface of the ganglion were accessible to the patch pipette. This method and the location of the labeled neurons obviated the need to sever the dorsal root or apply collagenase. Cell-attached recordings were performed under visual control using custom reflective optics on an upright compound microscope (Olympus, Scientifica). Pipettes (20 - 30 microns) were filled with an external solution comprising: 128 NaCl, 1.9 KCl, 1.2 KH_2PO_4, 26 $NaHCO_3$, 2.4 $CaCl_2$, 1.3 $MgSO_4$, and 10 glucose (mM). Cell-attached action potentials were recorded using a Multiclamp 700A amplifier (Axon Instruments) operating in the voltage-clamp configuration. Throughout each recording, the command potential was adjusted such that the amplifier did not pass current. Data was digitized at 40 kHz by a 16-bit A/D converter (USB-6259, National Instruments), low pass filtered at 10 kHz using the amplifier's internal four-pole Bessel filter, and acquired using Ephus (Suter et. al., 2010).

Tactile and electrical stimulation

Tactile stimuli were delivered to the receptive fields of neurons innervating the dorsal left hindlimb of the mouse. Reported von Frey thresholds are the lightest forces (in grams) within the set [0.008, 0.02, 0.04, 0.07, 0.16, 0.4, 0.6, 1, 1.4, 2, 4] that could elicit two or more responses out of 10-20 presentations to the receptive field. For hand-held stroke stimulation, a brush head (5/0 Round Princeton Art & Brush Co., Blick) was mounted to a strain gauge force sensor (MBL (BL341AH) 25 gram Model MBL load cell, Sensotec-Honeywell) connected to an amplifier (DMD-465WB, Omega) calibrated with known weights. The amplifier and load cell specifications state a flat frequency response over the acquisition bandwidth. Hand-held stroke stimuli were delivered during initial characterization of the receptive field, as well as instances where the receptive field location made mechanized stroke delivery infeasible. Force and velocity controlled mechanized stroke stimulation was delivered with a custom-built stimulator. Briefly, a brush head (5/0 Round Princeton Art & Brush Co., Blick) was mounted on a force-controlled

actuator (Model 300C-I, Aurora Scientific), which was translated across the skin with constant holding force by an ultrasonic piezoelectric translation stage (PI M-663 and PI C-867). Software for commanding and tracking stage motion are available at www.github.com/peltonen/touche. The reported electrophysiological responses to stroke (Figure 4C) are pooled across recordings employing manual and mechanized stimulus presentations.

Air puff was delivered through a blunted 16 gauge needle placed 3-5 mm above the skin. Air puff intensities are reported as velocities of 6, 9, 14, 18, 24, and 31 mm/sec (estimated from the volumetric flow rate divided by the cross-sectional area of the needle) delivered using a pressure controller (Picospritzer, Parker Hannifin). The X-Y position of the nozzle in relation to the receptive field was determined by first identifying the approximate region of sensitivity with an 18 mm/sec air puff stimulus. Next, the needle was translated in a serpentine pattern (250 micron steps) while delivering a 6 mm/sec air puff stimulus to identify the subregion of highest sensitivity. The nozzle was then maintained over this position, and responsiveness to air puff assessed in blocks of nine trials at the above listed velocities.

Force-controlled indentation of skin *in vivo* was achieved through a two-step process. First, the indenter was brought into contact with the skin under length control with a 0.4 mN holding force. Low-pass filtered force steps were synthesized in Matlab (Mathworks, Natick, MA) and output to a force-controlled indenter (Model 300 C-I, Aurora Scientific) in combination with a permissive length command. For machine-generated indentation receptive field mapping, the force-controlled indentations of the specified magnitudes were presented every three seconds, while the indenter was translated in a serpentine pattern in the intervening time to scan a rectangular grid.

Conduction velocity (CV) estimates were obtained by electrically stimulating the skin within the receptive field using a bipolar electrode. CVs were estimated by dividing the conduction latency by the distance between the DRG and the RF without accounting for the tortuosity of the sensory axon; thus, the reported CVs are a lower-bound on the true value.

***Ex vivo* electrophysiological recordings**

Generation of the *ex vivo* cutaneous somatosensory system preparation used in the present study has been described in detail (Li et al., 2011; Woodbury et al., 2001). Briefly, mice were deeply anesthetized (ketamine/xylazine, 90 and 10 mg/kg, respectively) and their hair clipped to ~2 mm before transcardial perfusion with oxygenated artificial cerebrospinal fluid (aCSF; in mM: 127.0 NaCl, 1.9 KCl, 1.2 KH_2PO4, 1.3 $MgSO_4$, 2.4 $CaCl_2$, 26.0 $NaHCO_3$, 10.0 D-glucose, containing 1 ml/L pen/strep) at RT. The spinal cord, thoracic DRGs, dorsal cutaneous nerves, and trunk skin on one side were dissected out in continuity in circulating aCSF (RT). Once isolated, this largely intact cutaneous somatosensory system was pinned out in the recording chamber with the hairy epidermal surface of the skin facing upward, the chamber transferred to the stage of a fluorescence microscope (Olympus BX51), and the bath then warmed to 30-31°C for electrophysiological recording. DRG cells were imaged under oblique fiber-optic illumination and intermittent fluorescence (Rolera EM-C2; QImaging, Surrey, BC, Canada). Fluorescently labeled somata were impaled with quartz micropipettes (150-300 MΩ) containing 20% Neurobiotin (Vector Laboratories, Burlingame, CA) and ~1% Alexa fluor 555 hydrazide (Molecular Probes, Eugene, OR) in 1 M potassium acetate to allow visualization of the electrode tip and verification that the intended cell was impaled. Electrical search stimuli were delivered en passant to the intact dorsal cutaneous nerve using a suction electrode to locate cells with axons in it. Evoked activity was amplified (Axoclamp 2B, Axon Instruments, CA) and digitized to disk for subsequent off-line analyses using Spike2 (CED, Cambridge, UK). Somal action potential duration in fluorescent cells of $TrkC^{CreER}$; $Ret^{f(CFP)}$ mice was measured at baseline and half-amplitude (D50) and compared with those of Npy2r-GFP^+ Aβ RA-LTMRs (Li et al., 2011) using t-tests (n = 13 cells for each sample); minimum cut-offs for inclusion in these analyses were a resting potential of -50 mV or less and clear presence of an after-hyperpolarization. Peripheral

conduction velocity was calculated from spike latency and the distance between electrodes along the nerve.

***Ex vivo* receptive field analyses**

To evaluate peripheral response properties, receptive fields were initially located with a fine sable hair paint brush or blunt glass stylus and investigated with calibrated von Frey filaments and fine watchmakers forceps with the aid of a zoom stereomicroscope at high power. Regions showing the greatest sensitivity "hotspots" were studied in greater detail using a feedback-controlled force/length stimulator (300C dual mode lever, Aurora Scientific, Aurora, ON, Canada) mounted on a micromanipulator to allow a range of forces to be consistently applied to the hotspot. For indenting forces, two different indenting arms were used, including a cylindrical probe ("blunt"; 1 mm diameter) and an insect pin ("sharp"), the distal pointed tip of which had been ground flat to a ~0.2 mm diameter facet to minimize skin penetration. Controlled pulling forces were applied to hairs using a customized microvascular clip that was suspended off the lever arm with non-compliant suture material after the indenting arm was removed and lowered to the hotspot. The normally smooth gripping jaws of this clip were modified to produce sharpened opposable edges that would pinch and securely clamp onto individual hair shafts without slip. This clamp was manually attached to individual hairs in the hotspot under magnification with the aid of applicator forceps. Hairs were successively sampled in a hair-by-hair fashion until one was located that elicited a response in the neuron upon gentle retraction; many individual hairs sampled in hotspots gave no response. The lever arm was then carefully raised to remove slack from the linkage before delivering protocols to retract the hair over a predetermined force-limited distance of 2 mm at a rate of 4 mm/sec, respectively, distances and rates that were identical to those used when applying indenting forces to the hotspot earlier. The effective lower limit of force that could be reliably applied with this system was 1 mN. Although close to threshold when indenting hotspots with the sharp probe, this force was typically well above threshold when traction was

applied to certain hairs in the hotspot, thus the threshold for this mode of stimulation could not be resolved. Following mechanical stimulation protocols, thermal sensitivity was tested in some cells by applying cold (4ºC) or heated (52-55ºC) saline directly to the RF using a syringe and 18 gauge needle; solutions delivered at bath temperatures controlled for mechanically-induced activation.

Transmission Electron Microscopy

P21 mice were fixed by cardiac perfusion using a solution containing 2% paraformaldehyde and 2.5% glutaraldehyde and a 0.1 M cacodylate buffer (pH 7.2). Hairs on the back were clipped after perfusion. A piece of back hairy skin (1 cm^2) was dissected on ice and post-fixed in the same perfusion solution overnight at 4ºC. The following day, the tissue was washed in 0.1 M cacodylate buffer for 3×10 min and then further cut into smaller pieces (1 mm^2). The small pieces of hairy skin were then treated with 1% Osmiumtetroxide (OsO_4)/1.5% Potassium ferrocyanide ($KFeCN_6$) for 1 hour at RT, washed by H_2O for 3×10 min, incubated in 1% aqueous uranyl acetate for 1hr at RT, washed again by H_2O again for 2×10 min, followed by dehydration in grades of alcohol (10min each: 50%, 70%, 90%; 2x10 min 100%). Tissue was then incubated in propyleneoxide for 1 hour at RT and then infiltrated in a 1:1 mixture of propyleneoxide and TAAB Epon (Marivac Canada Inc. St. Laurent, Canada) over night. The following day the samples were embedded in TAAB Epon and polymerized at 60ºC for 48 hrs. Toluidine blue-stained transverse sections of the hair follicles were made to determine the location of circumferential and lanceolate ending complex using sebaceous gland as a landmark. After that, Ultrathin sections (70-90 nm) were cut on a Reichert Ultracut-S microtome, picked up on to copper grids stained with lead citrate and examined in a JEOL 1200EX Transmission electron microscope at 80 kV and images were recorded with an AMT 2k CCD camera.

Behavioral test

All animals were acclimatized to the behavioral testing apparatus on 2-3 'habituation' sessions (0.5-1 hour per session, 1 session per day).

a) Rotarod test

To investigate sensorimotor coordination, mice were trained on the accelerating rotarod (IITC, USA). Training consisted of mice being placed on a rotarod moving at 5 rpm for 5 min. Mice were trained to stay on the rotarod for the entire 5 min. If a mouse fell, it was placed back on the rotarod and the 5 min trial was started again. Training took place on two consecutive days. Two days later, mice ran their full rotarod test. The rotarod began at 4 rpm and accelerated to 40 rpm over 5 min. The time to fall was automatically recorded. Experiment was repeated twice at 20 min intervals and the average was calculated as rotarod latency.

b) Dynamic brush test

To measure light touch sensitivity, mice were placed on an elevated wire grid and habituated for 15 min on the day of the experiment. The lateral plantar region of the left hindpaw (sural nerve territory) was stimulated by light stroking with a paintbrush (model 0, Cotman 222, Windsor & Newman), in the direction from heel to toe. The test was repeated five times, with intervals of 2-3 minutes.

To access the baseline response, the percentage of response (walking way, brief paw lifting, etc) was quantified (versus no evoked movement). To assess the dynamic allodynia after SNI, an allodynia score system (Duan et al., 2014) was used to quantify individual response and the average scores of the five tests were used to indicate their allodynia score. In detail, the typical response of naïve mice to the dynamic mechanical stimulation is a very fast movement of the stimulated paw aside (score 0). After the development of the neuropathy, several pain-like responses can be observed, including: sustained lifting (longer than 2 seconds) of the stimulated paw towards the body (score 1), strong lateral lifting above the level of the body and kicking to the lateral side (score 2), and flinching or licking of the affected paw (score 3).

c) Von Frey test

The von Frey test was carried out on the elevated wire grid after the dynamic brush test. The lateral plantar surface of the hindpaw was stimulated with calibrated von Frey monofilaments (0.008–6 g). The paw withdrawal threshold for the von Frey assay was determined by Dixon's up-down method (Chaplan et al., 1994).

d) Hargreaves test

To measure radiant heat pain by Hargreaves test, animals were put in plastic boxes and the plantar paw surface was exposed to a beam of radiant heat (IITC) according to the Hargreaves method. Paw withdrawal latency was then recorded (beam intensity was adjusted to result in a latency of 8–12 s for control animals). The heat stimulation was repeated 5 times at an interval of 10 min for each animal and the mean was calculated. A cutoff time of 30 s was set to prevent tissue damage.

e) Hot plate test

To further measure heat pain, we placed mice on a hot plate (IITC) and the latencies to hindpaw flinching and licking were measured. The hot plate was set at 50℃ or 54℃ and all animals were tested sequentially with a minimum of 5 min between tests. To avoid tissue injury, a cutoff time was set at 60 s and 30 s for assays at 50℃ and 54℃, respectively.

f) Cold plate test

To measure cold pain, we placed mice on a 0ºC cold plate (IITC) and the latencies to forepaw flinching and hindpaw licking were measured, as previously described (Knowlton et al., 2013). All animals were tested sequentially with a minimum of 5 min between tests. To avoid tissue injury, a cutoff time was set at 60 s.

Data Analysis

Statistical tests were performed using either Excel (Microsoft, Redmond, WA) or Python (Anaconda distribution, v. 2.7.10) with the *numpy*, *scipy.stats*, and *pandas* packages. Spike

detection was performed using the d_code package (Andrew Giessel, Cambridge, MA). Representative traces are high-pass filtered with an eight-pole Butterworth filter for display.

Error bars in all figures represent SEM and quantifications are presented as mean ± SEM.

Computational Modeling

A three-dimensional Finite Element Model (FEM) of the hair follicle ultrastructure was created and solved in Abaqus Standard (ver. 6.13). The physical model was built by referencing the structures observed through EM and light microscopy, and consists of four parts: the hair core (20 μm diameter), which is tilted 45 degrees with respect to the surface of the skin; the surrounding hair follicle (10 μm thick), and two layers containing collagen fibers with co-axial and circumferential orientations (3 μm and 2 μm thick, respectively, as observed using electron microscopy).

The simulated skin in this model is a 500 μm thick slab with the degree of freedoms fixed in the bottom. This thickness is over five times the depth of the endings relative to the skin surface and thus sufficient to account for mechanical responses at the endings, and the materials beyond 500 μm are not taken into account. Skin properties are simulated using the incompressible Mooney-Rivlin hyperelastic model:

$$W = C_{10}(I_1 - 3) + C_{01}(I_2 - 3),$$

where W is the strain energy, I_1 and I_2 are the first and second invariant:

$$I_1 = \lambda_1^2 + \lambda_2^2 + \lambda_3^2,$$

$$I_2 = \frac{1}{\lambda_1^2} + \frac{1}{\lambda_2^2} + \frac{1}{\lambda_3^2}.$$

and λ_i are the stretch ratios. The principal Cauchy stress is obtained by differentiating the strain energy with respect to the corresponding stretch ratio λ_i

$$\sigma_i = \lambda_i \frac{\partial W}{\partial \lambda_i}, i = 1, 2, 3.$$

The values of the parameters C_{10} and C_{01} may vary across a wide range depending on several factors, including humidity, temperature, and sampler's age. (Shergold et al., 2005; Wang et al., 2013; Xu and Lu, 2011). In this model C_{10} = 100 KPa and C_{01} = 0 were chosen to match the experimentally determined force vs. displacement relationship observed in laser Doppler vibrometric measurements of skin samples. The whole FE model is discretized by 73756 elements, which are mostly brick elements of type C3D20RH; minor wedge C3D15H and tetrahedron C3D10H elements are also applied to adapt to the irregular geometries. The material properties (Young's modulus, Poisson's ratio) of the hair, surrounding hair follicle, and collagen fibers has not been measured directly, so these parameters were assigned based on the properties of their primary constituents or estimated based on related materials. The hair core is assigned a linear elastic material property with modulus E = 500 MPa and Poisson's ratio ν = 0.3, based on experimental measurements of α-keratin. The Young's Modulus adopted for hair is lower than that of α-keratin (Feughelman, 1997), because the hair is undergoing bending rather than stretching, and because the dramatic difference between the Young's Modulus of α-keratin and the surroundings materials (for instance, 2000 MPa in α-keratin and 0.1 MPa in skin) frustrated attempts to achieve convergence. There is no literature defining the material properties of the hair follicle; thus, we assigned the same Poisson's ratio, but with a weaker modulus of E = 100 MPa. Material properties for the two collagen layers are defined to be transversely isotropic with the symmetric axis aligned with the collagen fibers. Based on the density of collagen fibers observed in the two layers, E = 100 MPa and E = 250 MPa were assigned for the modulus along the collagen fiber direction for inner and outer layers, respectively, while within the transverse plane E = 10 MPa, ν = 0.3 for both layers (Fung, 1981).

The mesh representation of circumferential and lanceolate ending ultrastructures was iteratively refined to achieve model convergence. The mechanical responses at the circumferential and lanceolate endings are measured by the strain in the collagen layers that surrounds these two types of endings. Two types of loadings are applied in the model: hair deflection and skin indentation, respectively. The hair deflection load is realized by applying the stated traction on the external surface of the hair. The skin indentation is realized by modeling the needle tip with a discrete rigid model, and pushing the skin through surface contact with the stated levels of force.

References

Abrahamsen, B., Zhao, J., Asante, C.O., Cendan, C.M., Marsh, S., Martinez-Barbera, J.P., Nassar, M. a, Dickenson, A.H., and Wood, J.N. (2008). The cell and molecular basis of mechanical, cold, and inflammatory pain. Science *321*, 702–705.

Abraira, V.E., and Ginty, D.D. (2013). The sensory neurons of touch. Neuron *79*, 618–639.

Albers, K.M., Perrone, T.N., Goodness, T.P., Jones, M.E., and Green, M.A. (1996). Cutaneous Overexpression of NT-3 Increases Sensory and Sympathetic Neuron Number and Enhances Touch Dome and Hair Follicle Innervation. J. Cell Biol. *134*, 487–497.

Badea, T.C., Cahill, H., Ecker, J., Hattar, S., and Nathans, J. (2009). Distinct roles of transcription factors brn3a and brn3b in controlling the development, morphology, and function of retinal ganglion cells. Neuron *61*, 852–864.

Badea, T.C., Williams, J., Smallwood, P., Shi, M., Motajo, O., and Nathans, J. (2012). Combinatorial expression of Brn3 transcription factors in somatosensory neurons: genetic and morphologic analysis. J. Neurosci. *32*, 995–1007.

Ballermann, M., McKenna, J., and Whishaw, I.Q. (2001). A grasp-related deficit in tactile discrimination following dorsal column lesion in the rat. Brain Res. Bull. *54*, 237–242.

Bang, S.J., Jensen, P., Dymecki, S.M., and Commons, K.G. (2012). Projections and interconnections of genetically defined serotonin neurons in mice. Eur. J. Neurosci. *35*, 85–96.

Bardoni, R., Tawfik, V.L., Wang, D., François, A., Solorzano, C., Shuster, S. a, Choudhury, P., Betelli, C., Cassidy, C., Smith, K., et al. (2014). Delta opioid receptors presynaptically regulate cutaneous mechanosensory neuron input to the spinal cord dorsal horn. Neuron *81*, 1312–1327.

Basbaum, A.I., Bautista, D.M., Scherrer, G., and Julius, D. (2009). Cellular and molecular mechanisms of pain. Cell *139*, 267–284.

Bentivoglio, M., and Pacini, P. (1995). Filippo Pacini: A determined observer. Brain Res. Bull. *38*, 161–165.

Biemesderfer, D., Munger, B.L., Binck, J., and Dubner, R. (1978). The pilo-ruffini complex: a non-sinus hair and associated slowly-adapting mechanorecepro in primate facial skin. Brain Res. *142*, 197–222.

Blake, D.T., Hsiao, S.S., and Johnson, K.O. (1997). Neural Coding Mechanisms in Tactile Pattern Recognition: The Relative Contributions of Slowly and Rapidly Adapting Mechanoreceptors to Perceived Roughness. J. Neurosci. *17*, 7480–7489.

Boada, M.D., and Woodbury, C.J. (2008). Myelinated skin sensory neurons project extensively throughout adult mouse substantia gelatinosa. J. Neurosci. *28*, 2006–2014.

Bourane, S., Grossmann, K.S., Britz, O., Dalet, A., Del Barrio, M.G., Stam, F.J., Garcia-Campmany, L., Koch, S., and Goulding, M. (2015). Identification of a Spinal Circuit for Light Touch and Fine Motor Control. Cell *160*, 503–515.

Brisben, A.J., Hsiao, S.S., and Johnson, K.O. (1999). Detection of Vibration Transmitted Through an Object Grasped in the Hand. J. Neurophysiol. *81*, 1548–1558.

Britain, G. (1988). CUTANEOUS EXCITATORY ANDaINHIBITORY INPUT TO NEURONES OF. Physiology 497–513.

Brown, A.G., and Iggo, A. (1967). A quantitative study of cutaneous receptors and afferent fibres in the cat and rabbit. J. Physiol. *193*, 707–733.

Burgess, B.Y.P.R., and Perl, E.R. (1967). Myelinated afferent fibers responding specifically to noxious stimulation of the skin. J. Physiol. *190*, 541–562.

Burgess, P.R., Petit, D., and Warren, R.M. (1968). Receptor Types in Cat Hairy Supplied Skin by Myelinated Fibers. J. Neurophysiol. *31*, 833–848.

Campbell, J.N., and Meyer, R. a (2006). Mechanisms of neuropathic pain. Neuron *52*, 77–92.

Campbell, J.N., Raja, S.N., Meyer, R. a., and Mackinnon, S.E. (1988). Myelinated afferents signal the hyperalgesia associated with nerve injury. Pain *32*, 89–94.

Cauna, N. (1956). Nerve supply and nerve endings in Meissner's corpuscles. Am. J. Anat. *99*, 315–350.

Cauna, N., and Mannan, G. (1958). The structure of human digital pacinian corpuscles (corpus cula lamellosa) and its functional significance. J. Anat. *92*, 1–20.

Cauna, N., and Ross, L.L. (1960). The fine structure of Meissner's touch corpuscles of human fingers. J. Biophys. Biochem. Cytol. *8*, 467–482.

Chambers, M.R., Andres, K.H., Duering, M. V, and Iggo, A. (1972). The structure and function of the slowly adapting type II mechanoreceptor in hairy skin. Quarlerly J. Exp. Physiol. *57*, 417–445.

Chaplan, S.R., Bach, F.W., Pogrel, J.W., Chung, J.M., and Yaksh, T.L. (1994). Quantitative assessment of tactile allodynia in the rat paw. J. Neurosci. Methods *53*, 55–63.

Cliffer, G., and Cliffer, K. (1985). Postsynaptic Dorsal Column Pathway of the Rat . II . Evidence Against an Important Role in Nociception. Brain Res. *326*, 347–356.

Costigan, M., Scholz, J., and Woolf, C.J. (2009). Neuropathic pain: a maladaptive response of the

nervous system to damage. Annu. Rev. Neurosci. *32*, 1–32.

Decosterd, I., and Woolf, C.J. (2000). Spared nerve injury: An animal model of persistent peripheral neuropathic pain. Pain *87*, 149–158.

Djouhri, L., and Lawson, S.N. (2004). Abeta-fiber nociceptive primary afferent neurons: a review of incidence and properties in relation to other afferent A-fiber neurons in mammals. Brain Res. Brain Res. Rev. *46*, 131–145.

Dobry, P.J.K., and Casey, K.L. (1972). Roughness discrimination in cats with dorsal column lesions. Brain Res. *44*, 385–397.

Duan, B., Cheng, L., Bourane, S., Britz, O., Padilla, C., Garcia-Campmany, L., Krashes, M., Knowlton, W., Velasquez, T., Ren, X., et al. (2014). Identification of Spinal Circuits Transmitting and Gating Mechanical Pain. Cell *159*, 1417–1432.

Durbec, P., Marcos-Gutierrez, C. V, Kilkenny, C., Grigoriou, M., Wartiowaara, K., Suvanto, P., Smith, D., Ponder, B., Costantini, F., and Saarma, M. (1996). GDNF signaling through the Ret receptor tyrosine kinase. Nature *381*, 789–793.

Fagan, B., and Cahusac, P.M.B. (2001). Evidence for glutamate receptor mediated transmission at mechanoreceptors in the skin. [Miscellaneous Article]. Neuroreport Febr. 12, 2001 *12*, 341–347.

Feughelman, M. (1997). Mechanical properties and structure of alpha-keratin fibres: wool, human hair and related fibres. (University of New South Wales Press).

Finger, T.E., Danilova, V., Barrows, J., Bartel, D.L., Vigers, A.J., Stone, L., Hellekant, G., and Kinnamon, S.C. (2005). ATP Signaling Is Crucial for Communication from Taste Buds to Gustatory Nerves. Science (80-.). *310*, 1495–1499.

Flavell, C.R., Cerminara, N.L., Apps, R., and Lumb, B.M. (2014). Spino-Olivary Projections in the Rat Are Anatomically Separate From Postsynaptic Dorsal Column Projections. *2190*, 2179–2190.

Fuchs, L. Somatotopic Representation of Hindlimb Skin in Cat Dorsal Horn.

Fünfschilling, U., Ng, Y.-G., Zang, K., Miyazaki, J.-I., Reichardt, L.F., and Rice, F.L. (2004). TrkC kinase expression in distinct subsets of cutaneous trigeminal innervation and nonneuronal cells. J. Comp. Neurol. *480*, 392–414.

Fung, Y.C. (1981). Biomechanics: Mechanical Properties of Living Tissue (New York: Springer Science and Business Media New York).

Gross, M.K., Dottori, M., Goulding, M., and Jolla, L. (2002). Lbx1 Specifies Somatosensory Association Interneurons in the Dorsal Spinal Cord. *34*, 535–549.

Halata, Z., Grim, M., and Bauman, K.I. (2003). Friedrich Sigmund Merkel and his "Merkel cell", morphology, development, and physiology: Review and new results. Anat. Rec. Part A Discov. Mol. Cell. Evol. Biol. *271A*, 225–239.

Hartschuh, W., and Weihe, E. (1980). Fine Structural Analysis of the Synaptic Junction of Merkel Cell-Axon-Complexes. J. Invest. Dermatol. *75*, 159–165.

Horch, K.W., Burgess, P.R., and Whitehorn, D. (1976). Ascending collaterals of cutaneous neurons in the fasciculus gracilis of the cat. Brain Res. *117*, 1–17.

Horch, K.W., Tuckett, R.P., and Burgess, P.R. (1977). A key to the classification of cutaneous mechanoreceptors. J. Invest. Dermatol. *69*, 75–82.

Houghton, A.K., Hewitt, E., and Westlund, K.N. (1999). Dorsal column lesion prevents

mechanical hyperalgesia and allodynia in osteotomy model. Pain *82*, 73–80.

Hu, J., Chiang, L.-Y., Koch, M., and Lewin, G.R. (2010). Evidence for a protein tether involved in somatic touch. EMBO J. *29*, 855–867.

Idé, C. (1976). The fine structure of the digital corpuscle of the mouse toe pad, with special reference to nerve fibers. Am. J. Anat. *147*, 329–355.

Iggo, a (1960). Cutaneous mechanoreceptors with afferent C fibres. J. Physiol. *152*, 337–353.

Iggo, A., and Muir, A.R. (1969). The structure and function of a slowly adapting touch corpuscle in hairy skin. J. Physiol. *200*, 763–796.

Iggo, A., and Ogawa, H. (1977). Correlative physiological and morphological studies of rapidly adapting mechanoreceptors in cat's glabrous skin. J. Physiol. *266*, 275–296.

Ikeda, R., Cha, M., Ling, J., Jia, Z., Coyle, D., and Gu, J.G. (2014). Merkel cells transduce and encode tactile stimuli to drive Aβ-afferent impulses. Cell *157*, 664–675.

Johansson, R.S. (1978). Tactile sensibility in the human hand: receptive field characteristics of mechanoreceptive units in the glabrous skin area. J. Physiol. *281*, 101–125.

Knibestöl, M. (1973). Stimulus—response functions of rapidly adapting mechanoreceptors in the human glabrous skin area. J. Physiol. *232*, 427–452.

Koerber, H.R., Druzinsky, R.E., and Mendell, L.M. (1988). Properties of somata of spinal dorsal root ganglion cells differ according to peripheral receptor innervated. J. Neurophysiol. *60*, 1584–1596.

Koltzenburg, M., Stucky, C.L., and Lewin, G.R. (1997). Receptive properties of mouse sensory neurons innervating hairy skin. J. Neurophysiol. *78*, 1841–1850.

Krimm, R.F., Davis, B.M., and Albers, K.M. (1999). Cutaneous Overexpression of Neurotrophin-3 (NT3) Selectively Restores Sensory Innervation In NT3 Gene Knockout Mice. John Wiley Sons, Inc *3*, 40–49.

Lamballe, F., Klein, R., and Barbacid, M. (1991). trkC, a new member of the trk family of tyrosine protein kinases, is a receptor for neurotrophin-3. Cell *66*, 967–979.

Lechner, S.G., and Lewin, G.R. (2013). Hairy sensation. Physiology (Bethesda). *28*, 142–150.

LeMasurier, M., and Gillespie, P.G. (2005). Hair-Cell Mechanotransduction and Cochlear Amplification. Neuron *48*, 403–415.

Lesniak, D.R., Marshall, K.L., Wellnitz, S. a, Jenkins, B. a, Baba, Y., Rasband, M.N., Gerling, G.J., and Lumpkin, E. a (2014). Computation identifies structural features that govern neuronal firing properties in slowly adapting touch receptors. Elife *3*, e01488.

Li, L., and Ginty, D.D. (2014). The structure and organization of lanceolate mechanosensory complexes at mouse hair follicles. Elife *3*, e01901.

Li, L., Rutlin, M., Abraira, V.E., Cassidy, C., Kus, L., Gong, S., Jankowski, M.P., Luo, W., Heintz, N., Koerber, H.R., et al. (2011). The functional organization of cutaneous low-threshold mechanosensory neurons. Cell *147*, 1615–1627.

Liu, Q., Vrontou, S., Rice, F.L., Zylka, M.J., Dong, X., and Anderson, D.J. (2007). Molecular genetic visualization of a rare subset of unmyelinated sensory neurons that may detect gentle touch. Nat. Neurosci. *10*, 946–948.

Loewenstein, W.R. (1969). Rate sensitivity of a biological transducer. Ann. N. Y. Acad. Sci. *156*, 892–900.

Loewenstein, W.R., and Skalak, R. (1966). Mechanical transmission in a Pacinian corpuscle. An analysis and a theory. J. Physiol. *182*, 346–378.

Löken, L.S., Wessberg, J., Morrison, I., McGlone, F., and Olausson, H. (2009). Coding of pleasant touch by unmyelinated afferents in humans. Nat. Neurosci. *12*, 547–548.

Lumpkin, E. a, Marshall, K.L., and Nelson, A.M. (2010). The cell biology of touch. J. Cell Biol. *191*, 237–248.

Luo, W., Enomoto, H., Rice, F.L., Milbrandt, J., and Ginty, D.D. (2009). Molecular identification of rapidly adapting mechanoreceptors and their developmental dependence on ret signaling. Neuron *64*, 841–856.

Ma, C., and LaMotte, R.H. (2007). Multiple sites for generation of ectopic spontaneous activity in neurons of the chronically compressed dorsal root ganglion. J. Neurosci. *27*, 14059–14068.

Madsen, M. (1984). Postsynaptic Dorsal Column Pathway of the Rat . I . Anatomical Studies. *51*.

Maksimovic, S., Nakatani, M., Baba, Y., Nelson, A.M., Marshall, K.L., Wellnitz, S. a, Firozi, P., Woo, S.-H., Ranade, S., Patapoutian, A., et al. (2014). Epidermal Merkel cells are mechanosensory cells that tune mammalian touch receptors. Nature *509*, 617–621.

Mantyh, P.W. (1997). Inhibition of Hyperalgesia by Ablation of Lamina I Spinal Neurons Expressing the Substance P Receptor. Science (80-.). *278*, 275–279.

Maricich, S.M., Wellnitz, S. a, Nelson, A.M., Lesniak, D.R., Gerling, G.J., Lumpkin, E. a, and Zoghbi, H.Y. (2009a). Merkel cells are essential for light-touch responses. Science *324*, 1580–1582.

Maricich, S.M., Wellnitz, S.A., Nelson, A.M., Lesniak, D.R., Gerling, G.J., Lumpkin, E.A., and

Zoghbi, H.Y. (2009b). Merkel Cells Are Essential for Light-Touch Responses. Science (80-.). *324*, 1580–1582.

McIlwrath, S.L., Lawson, J.J., Anderson, C.E., Albers, K.M., and Koerber, H.R. (2007). Overexpression of neurotrophin-3 enhances the mechanical response properties of slowly adapting type 1 afferents and myelinated nociceptors. Eur. J. Neurosci. *26*, 1801–1812.

Mihara, M., Hashimoto, K., Ueda, K., and Kumakiri, M. (1979). The Specialized Junctions between Merkel Cell and Neurite: An Electron Microscopic Study. J. Invest. Dermatol. *73*, 325–334.

Millar, J., and Basbaum, A.I. (1975). Topography of the projection of the body surface of the cat to cuneate and gracile nuclei. Exp. Neurol. *49*, 281–290.

Millard, C.L., and Woolf, C.J. (1988). Sensory innervation of the hairs of the rat hindlimb: a light microscopic analysis. J. Comp. Neurol. *277*, 183–194.

Nichols, M.L. (1999). Transmission of Chronic Nociception by Spinal Neurons Expressing the Substance P Receptor. Science (80-.). *286*, 1558–1561.

Niu, J., Ding, L., Li, J.J., Kim, H., Liu, J., Li, H., Moberly, A., Badea, T.C., Duncan, I.D., Son, Y.-J., et al. (2013). Modality-based organization of ascending somatosensory axons in the direct dorsal column pathway. J. Neurosci. *33*, 17691–17709.

Orefice, L.L., Zimmerman, A.L., Chirila, A.M., Sleboda, S.J., Head, J.P., Ginty, D.D., Orefice, L.L., Zimmerman, A.L., Chirila, A.M., Sleboda, S.J., et al. (2016). Peripheral Mechanosensory Neuron Dysfunction Underlies Tactile and Behavioral Deficits in Mouse Models of ASDs Article Peripheral Mechanosensory Neuron Dysfunction Underlies Tactile and Behavioral Deficits in Mouse Models of ASDs. Cell *166*, 299–313.

Ossipov, M.H., Zhang, E., Carvajal, C., Gardell, L., Quirion, R., Dumont, Y., Lai, J., and Porreca, F. (2002). Selective Mediation of Nerve Injury-Induced Tactile Hypersensitivity by Neuropeptide Y. *22*, 9858–9867.

Paré, M., Smith, A.M., and Rice, F.L. (2002). Distribution and terminal arborizations of cutaneous mechanoreceptors in the glabrous finger pads of the monkey. J. Comp. Neurol. *445*, 347–359.

Pawson, L., Slepecky, N.B., and Bolanowski, S.J. (2000). Immunocytochemical identification of proteins within the Pacinian corpuscle. Somatosens. Mot. Res. *17*, 159–170.

Pease, D.C., and Quilliam, T.A. (1957). Electron Microscopy of the Pacinian Corpuscle. J. Biophys. Biochem. Cytol. *3*, 331–342.

Peirs, C., Williams, S.G., Zhao, X., Liu, Z., Paulina, S., Seal, R.P., Peirs, C., Williams, S.G., Zhao, X., Walsh, C.E., et al. (2015). Dorsal Horn Circuits for Persistent Mechanical Pain. Neuron *87*, 797–812.

Petitjean, H., Pawlowski, S.A., Fraine, S.L., Braz, J.M., Basbaum, A.I., Sharif-naeini, R., Petitjean, H., Pawlowski, S.A., Fraine, S.L., Sharif, B., et al. (2015). Dorsal Horn Parvalbumin Neurons Are Gate-Keepers of Touch-Evoked Pain after Nerve Injury Article Dorsal Horn Parvalbumin Neurons Are Gate-Keepers of Touch-Evoked Pain after Nerve Injury. CellReports 1–12.

Ray, R.S., Corcoran, A.E., Brust, R.D., Kim, J.C., Richerson, G.B., Nattie, E., and Dymecki, S.M. (2011). Impaired Respiratory and Body Temperature Control Upon Acute Serotonergic Neuron Inhibition. Science (80-.). *333*, 637–642.

Rice, F.L., and Munger, B.L. (1986). A Comparative Light Microscopic Analysis of the Sensory

Innervation of the Mystacial Pad . II . The Common Fur Between the Vibrissae. J. Comp. Neurol. *252*, 186–205.

Rotolo, T., Smallwood, P.M., Williams, J., and Nathans, J. (2008). Genetically-Directed, Cell Type-Specific Sparse Labeling for the Analysis of Neuronal Morphology. PLoS One *3*, e4099.

Rutlin, M., Ho, C.-Y., Abraira, V.E., Cassidy, C., Bai, L., Woodbury, C.J., and Ginty, D.D. (2014). The Cellular and Molecular Basis of Direction Selectivity of Aδ-LTMRs. Cell *159*, 1640–1651.

Sato, M. (1961). Response of Pacinian corpuscles to sinusoidal vibration. J. Physiol. *159*, 391–409.

Shergold, O.A., Fleck, N.A., and Radford, D. (2005). The uniaxial stress versus strain response of pig skin and silicone rubber at low and high strain rates. Int. J. Impact Eng. *32*, 1384–1402.

Spencer, P.S., and Schaumburg, H.H. (1973). An ultrastructural study of the inner core of the Pacinian corpuscle. J. Neurocytol. *2*, 217–235.

Sun, H., Ren, K., Zhong, C.M., Ossipov, M.H., Jr, T.P.M., Lai, J., and Porreca, F. (2001). Nerve injury-induced tactile allodynia is mediated via ascending spinal dorsal column projections. *90*, 105–111.

Takahashi, Y., Chiba, T., Sameda, H., Ohtori, S., Kurokawa, M., and Moriya, H. (2002). Organization of cutaneous ventrodorsal and rostrocaudal axial lines in the rat hindlimb and trunk in the dorsal horn of the spinal cord. J. Comp. Neurol. *445*, 133–144.

Takahashi-Iwanaga, H., and Shimoda, H. (2003). The three-dimensional microanatomy of Meissner corpuscles in monkey palmar skin. J. Neurocytol. *32*, 363–371.

Talbot, W.H., Darian-Smith, I., Kornhuber, H.H., and Mountcastle, V.B. (1968). The sense of flutter-vibration: comparison of the human capacity with response patterns of mechanoreceptive afferents from the monkey hand. J. Neurophysiol. *31*, 301–334.

Trupp, M., Arenas, E., Fainzilber, M., Nilsson, a S., Sieber, B. a, Grigoriou, M., Kilkenny, C., Salazar-Grueso, E., Pachnis, V., and Arumäe, U. (1996). Functional receptor for GDNF encoded by the c-ret proto-oncogene. Nature *381*, 785–789.

Uesaka, T., Nagashimada, M., Yonemura, S., and Enomoto, H. (2008). Diminished Ret expression compromises neuronal survival in the colon and causes intestinal aganglionosis in mice. J. Clin. Invest. *118*, 1890–1898.

Vallbo, A., Olausson, H., Wessberg, J., and Norrsell, U. (1993). A system of unmyelinated afferents for innocuous mechanoreception in the human skin. Brain Res. *628*, 301–304.

Wang, Y., Marshall, K.L., Baba, Y., Gerling, G.J., and Lumpkin, E. a. (2013). Hyperelastic Material Properties of Mouse Skin under Compression. PLoS One *8*, e67439.

Willis, W.D., Al-Chaer, E.D., Quast, M.J., and Westlund, K.N. (1999). A visceral pain pathway in the dorsal column of the spinal cord. PNAS *96*, 7675–7679.

Woo, S.-H., Ranade, S., Weyer, A.D., Dubin, A.E., Baba, Y., Qiu, Z., Petrus, M., Miyamoto, T., Reddy, K., Lumpkin, E.A., et al. (2014). Piezo2 is required for Merkel-cell mechanotransduction. Nature *509*, 622–626.

Woodbury, C.J., and Koerber, H.R. (2007). Central and Peripheral Anatomy of Slowly Adapting Type I Low-Threshold Mechanoreceptors Innervating Trunk. J. Comp. Neurobiol. *561*, 547–561.

Woodbury, C.J., Ritter, A.M., and Koerber, H.R. (2001). Central anatomy of individual rapidly adapting low-threshold mechanoreceptors innervating the hairy skin of newborn mice: Early

maturation of hair follicle afferents. J. Comp. Neurol. *436*, 304–323.

Wu, H., Williams, J., and Nathans, J. (2012). Morphologic diversity of cutaneous sensory afferents revealed by genetically directed sparse labeling. Elife *1*, e00181.

Xu, F., and Lu, T.J. (2011). Introduction to skin biothermomechanics and thermal pain (Science Press).

Xu, Z.-Z., Kim, Y.H., Bang, S., Zhang, Y., Berta, T., Wang, F., Oh, S.B., and Ji, R.-R. (2015). Inhibition of mechanical allodynia in neuropathic pain by TLR5-mediated A-fiber blockade. Nat. Med. *21*, 1–9.

Yamamoto, T. (1966). The Fine Structure of the Palisade-type Sensory Endings in Relation to Hair Follicles. J. Electron Microsc. (Tokyo). *15*, 158–166.

Yamamoto, W., Sugiura, A., Nakazato-Imasato, E., and Kita, Y. (2008). Characterization of primary sensory neurons mediating static and dynamic allodynia in rat chronic constriction injury model. J. Pharm. Pharmacol. *60*, 717–722.

Yang, Y., Ogawa, Y., Hedstrom, K.L., and Rasband, M. (2007). βIV spectrin is recruited to axon initial segments and nodes of Ranvier by ankyrinG. J. Cell Biol. *176*, 509–519.

Zimmerman, A., Bai, L., and Ginty, D.D. (2014). The gentle touch receptor of mammalian skin. Science *346*, 950–954.

Ling Bai

Phone: (443) 683-1317; Email: echo.bailing@gmail.com;

Address: Harvard Medical School, 200 Longwood Ave, Armenise 437, Boston, MA 02115

EDUCATION

2016 **Ph.D. Candidate**, Department of Neuroscience, Johns Hopkins University, School of Medicine

2009 **Bachelor of Science, Biology**, School of Life Sciences, Tsinghua University, Beijing, China

AWARDS and HONORS

2016 Nupur Dinesh Thekdi Award, Young Investigators' Day Program, Johns Hopkins University

RESEARCH EXPERIENCE

2010-16 Graduate Research Assistant, Department of Neuroscience, Johns Hopkins University, School of Medicine, Baltimore, USA
Thesis: A Genetic Approach to Study the Anatomical and Molecular Basis of the Sense of Touch
Advisor: Dr. David D. Ginty

2009-10 Rotations, Johns Hopkins University, School of Medicine, Baltimore, USA
Advisor: Dr. David D. Ginty, Dr. Elisabeth B. Glowatzki, Dr. Christopher J. Potter, Dr. Richard L. Huganir,

2008-09 Undergraduate Research Assistant, School of Life Sciences, Tsinghua University, Beijing, China
Research Project: Investigation of the molecular mechanism of cell cycle reentry in Alzheimer's Disease
Advisor: Dr. Yi Zhong

2007-08 Undergraduate Research Assistant, School of Life Sciences, Tsinghua University, Beijing, China
Research Project: High throughput screening for genes rescuing Alzheimer's disease in the drosophila
Advisor: Dr. Yi Zhong

PUBLICATIONS

Bai, L.*, Lehnert, B.P.*, Liu, J., Neubarth, N.L., Dickendesher, T.L., Nwe, P.H., Cassidy, C., Woodbury, C.J., Ginty, D.D. (2015). Genetic identification of an expansive mechanoreceptor sensitive to skin stroking, *Cell* 163, 1783-95. *Co-first author

Rutlin, M., Ho, C.-Y., Abraira, V.E., Cassidy, C., **Bai, L.**, Woodbury, C.J., and Ginty, D.D. (2014). The cellular and molecular basis of direction selectivity of Aδ-LTMRs. *Cell* 159, 1640–1651.

Zimmerman, A., **Bai, L.**, and Ginty, D.D. (2014). The gentle touch receptors of mammalian skin. *Science 346*, 950–954.

RESEARCH PRESENTATION

2015 Poster presentation at the Gordon Research Conference, Modulation of Neural Circuits and Behavior
Bai, L., Lehnert, B.P., Liu, J., Neubarth, N.L., Dickendesher, T.L., Woodbury, C.J., Ginty, D.D. "Genetic identification of cutaneous sensory neurons that selectively respond to gentle stroking of the skin".

2014 Poster at HHMI Investigators Meeting
Bai, L., Lehnert, B.P., Woodbury, C.J., Ginty, D.D. "Identification and characterization of a cutaneous touch receptor: the field receptor revisited".

2013 Oral presentation at the Janelia Farm Conference, Mammalian Circuits Underlying Touch Sensation
Bai, L., Woodbury, C.J., Ginty, D.D. "Molecular genetic identification of cutaneous Aβ-nociceptors".

ADVISING

2015-16 Casey Gilman, Neuroscience Program Student, Simmons College, Senior Thesis

2014-16 Pann H. Nwe, Public Health Program Student, Simmons College, Research Assistant

2013 Mikaela Freundlich, Biology B.S., Denison University, Summer Student

2012 Yang Zheng, Neuroscience Ph.D. Student, Rotation Student